Ferrocene Functionalized Achiral Amines:Synthesis, Characterization, *In-silico* study and Evaluation of as Cytotoxic Agents

Abstract

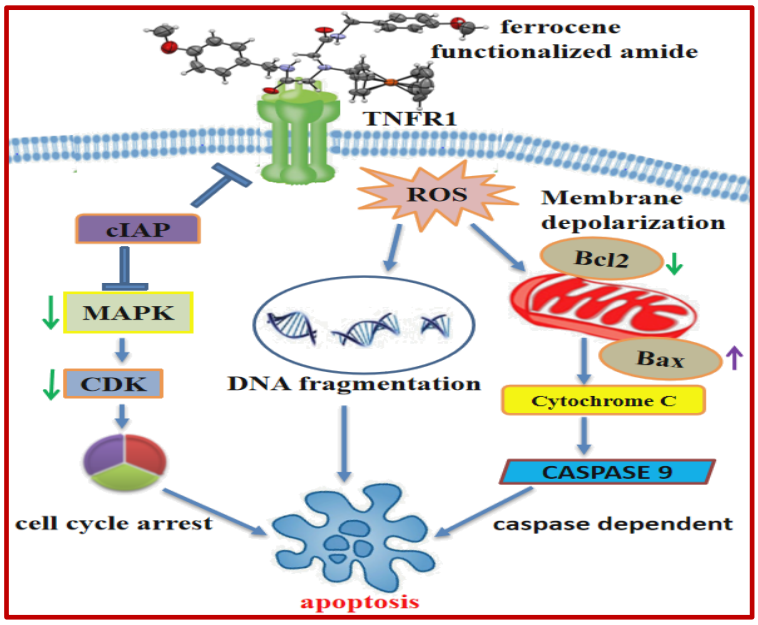

Ferrocenylmethylamine was chosen as a lead compound to synthesize a new series of amide functionalized 2º- and 3º-aminomethylferrocene. The new compounds were characterized by microanalysis, ^{1}H, ^{13}C NMR, UV-visible, fluorescence, FTIR, thermogravimetric and crystallographic techniques. *In vitro* anticancer activity of these derivatives was evaluated against MCF 7, IMR 32, HepG2 and immortal L132 cell lines by MTT assay and the results were compared with cisplatin. Interestingly, many compounds were extremely active against all the investigated cell lines and proved to be more potent as cytotoxic agents than cisplatin. In particular, diamide functionalized 3º-ferrocenylmethylamine 5b was shown to be active in low μM range against MCF7 (2.10 μM) and HepG2 (8.66 μM). The western blot, gene expression, mitochondrial membrane potential and flow cytometry study were used to explain the mode of action of these derivatives as antitumor agents. Density functional theory calculations and molecular docking have been performed to rationalize the experimental results. These ligands provide an opportunity to derive varied bioactive compounds by using free amino handle of 2º-ferrocenylmethylamines.

2.1 Introduction

The qualifications of new molecules that induce apoptosis and DNA fragmentation by different biological as well as cytological processes is crucial for the discovery and development of novel anticancer agents.[1, 2] In this regard, ferrocene containing compounds have been emerged as one of the robust anticancer agents.[3, 4] The involvement of ferrocene in the generation of reactive oxygen species (ROS) within cells, improvement of biological activity, overcome resistance barriers, lipophilic character, redox activity, enables easier passage through cell membranes has been already been recorded.[5, 6] Despite the nontoxic nature of ferrocene, its stability in aqueous and aerobic media, many ferrocenyl derivatives exhibit significant anticancer, antibacterial, antiparasitic, antifungal, and other biological activities.[7] In particular, Jaouen et al has developed more efficient ferrocifen type anticancer agents as analogues of the tamoxifen with innovative mechanisms of action.[8] Further reports suggest that the incorporation of amino groups into the molecular framework helps in an active transport process via the formation of organic cation transporters and it is responsible for the improved biological activity.[9, 10] For instance, covalently linkage of N,N-dimethyl tertiary amino group to celastrol (CTA) exhibited excellent cellular uptake efficiency in both rat pancreatic acinar cell line (AR42J) and human pulmonary alveolar epithelial cell line (A549).[11] Moreover, there are many drugs available in the market viz. Penicillin G, Mociobemide, Acetazolamide, Trimethobenzamide etc. which contains amide linkage in the nucleus and possesses various therapeutic activities.[12] Very recently, Professor Jianjun Chen and his group reported a number of diarylmethane amides displaying excellent neuroprotective and anticancer activities.[13]

In the light of the above considerations, we began with the optimization of the reaction conditions to obtain new ferrocenylmethylamine derivatives. Synthetically challenging derivatives ca 2-(ferrocenylmethylamino)-N-alkylacetamides 1a-5a and 2, 2'-(ferrocenylmethylazanediyl)bis(N- alkylacetamides) 1b-5b were derived selectively and characterized for their apoptotic potentials against human cancer cell lines. To prove the efficacy of these ligands as promising pro-drug, an inflammatory pathway study was carried out with a detail molecular mechanism. X-ray crystallography was used to elucidate the openings of secondary interactions provided by means of scaffold substitutions. We attempted to explore the apoptotic regulatory influence of various substitution patterns at the amidic nitrogen on the inhibition of TNFα protein by means of molecular docking. The synthesized inhibitors contained an optimal substitution of *p*-methybenzyl in 4b and *p*-

methoxybenzyl in 5b ligands, allowing us to probe the interplay of secondary interactions of the modified amidic nucleus with the TNFR1 protein.

2.2 Experimental Section

2.2.1 Materials and measurements

All amines were synthesized following literature procedure. Ferrocenylmethylamine, α-chloroamide precursors were synthesized by a modified literature procedure.[10,14] Reactions and handlings were performed in the atmosphere of nitrogen. All the chemicals and solvents used in this work were of laboratory grade available at various commercial sources and used without further purification. Thin Layer Chromatography was performed on Merck 60 F254 aluminium coated plates. FT-IR (KBr pellets) spectra were recorded in the 4000-400 cm^{-1} range using a Perkin-Elmer FT-IR spectrometer. The NMR experiments were carried out on a Bruker AV-III 400 MHz spectrometer in $CDCl_3$ solvents as per the solubility and chemical shifts are reported in parts per million (ppm). UV-visible absorption spectra were recorded on a JASCO V-730 UV-visible spectrophotometer Fluorescence was recorded on JASCO make spectrofluorometer model FP-8200. TGA/DTA plots were obtained using SII TG/DTA 6300 in flowing N_2 with a heating rate of 10 °C min^{-1}.

2.2.2 General procedure for the synthesis of amino methyl ferrocene from ferrocene

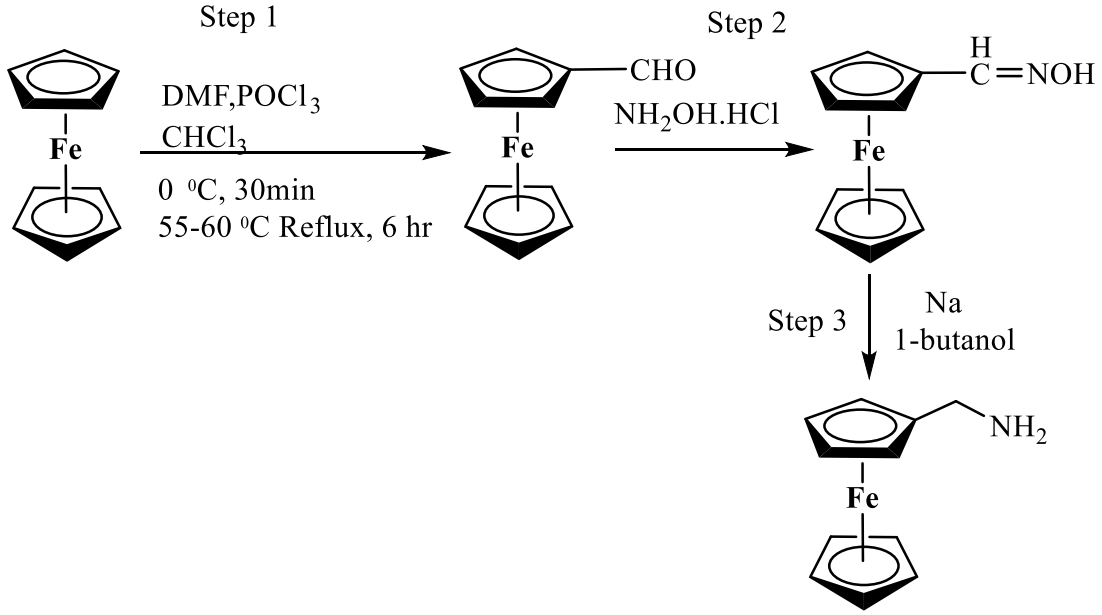

Scheme 1. Synthesis of amino methyl ferrocene from ferrocene.

Step 1: Ferrocene to formylferrocene

4.71g (0.066mol) of dimethylformamide was added to the solution of 2.0g (0.011mol) of ferrocene in 10ml of dry chloroform in three necked round bottle flask and the resulting mixture was stirred in an ice-bath under nitrogen atmosphere for 10 minutes. Then, 10.1g (0.066mol) of phosphoryl chloride was added dropwise to the mixture over about half an hour. After the addition had been completed, the reaction mixture was kept stirring for 6hr under heating at 55-60ºC on a water-bath taking care that the temperature did not exceed 60ºC. At the end of the reaction, chloroform was evaporated off under reduced pressure below 60 ºC and the residue was poured into the mixture of ice and water. Solid precipitates, most of which should be unreacted ferrocene, was filtered off. The filtrate, aqueous solution of the Vilsmeier complex, was neutralized carefully with saturated solution of sodium carbonate and then was extracted twice with ethyl acetate. All the extracts were combined together and dried over anhydrous sodium sulphate. The crude product obtained by evaporation of the solvent got reddish brown solid. MP 124.5 ºC. The yield was 1.6g (72%).

Step 2: Formylferrocene to ferrocenecarboxyaldehyde oxime

To a solution of ferrocenecarboxyaldehyde 2.5 (0.011mol) in EtOH (45 ml), the solution of hydroxylamine hydrochloride 085(0.012mol) in water (5 ml) was added under N_2, then followed by AcONa 1.80g (0.033mol). The mixture was heated under reflux for 3 h, cooled and concentrated in vacuum. The product was extracted with $CHCl_3$ or dichloromethane and collected the organic layer then dry over Na_2SO_4. Removing the solvent by rotator evaporator and got the brown red colour solid compound. The yield was 2.55g (95.0%).

Step 3: Ferrocenecarboxyaldehyde oxime to amino methyl ferrocene

The solution of ferrocenecarboxaldehyde oxime 2.0g (0.008mol) in 1-butanol (65 ml) was stirred under reflux, followed by the addition of Na 4.6g (0.20mol) in small portions in 1 h. Then, the refluxing was continued for an additional 2 h. The mixture was cooled to room temperature, acidified with 20% H_2SO_4 (65 ml) and extracted twice with dichloromethane. The water phase was alkalized with NaOH to pH 11-12 and then extracted with dichloromethane. The combined dichloromethane phase was dried up with anhydrous Na_2SO_4, filtered, concentrated under vacuum to give brown oil 0.92g in 50.2% yield. It was used for the following reactions directly without any further purification.

2.2.3 General procedure for the synthesis of 2-(ferrocenylmethylamino)-N-alkylacetamide (1a-5a)

N-cyclohexyl-2-iodoacetamide was prepared by reacting N-cyclohexyl-2-chloroacetamide with KI in acetone and it was subsequently utilized in the synthesis of corresponding 2-(ferrocenylmethylamino)-*N*-alkylacetamides, ca *N*-benzyl-2-iodoacetamide (0.289 g, 1.05 mmol), *N*-cyclohexyl-2-iodoacetamide (0.280 g, 1.05 mmol), *N*-furfuryl-2-iodoacetamide (0.278 g, 1.05 mmol), *N*-4-methylbenzyl-2-iodoacetamide (0.303 g, 1.05 mmol) or *N*-4-methoxybenzyl-2-iodoacetamide (0.320 g, 1.05 mmol) was added portion wise to the solution of amino methyl ferrocene (0.215 g, 1.0 mmol) in 25 ml of $CHCl_3$ containing 3-4 drops of Et_3N. The reaction mixture was reflux for 3 hours. The progress of the reaction was monitored by thin layer chromatography and ninhydrin. The reaction mixture was cooled at room temperature and solvent was removed under vacuum. Distilled water was added in the solid residue and the crude product was extracted by using dichloromethane. It was dried over Na_2SO_4 for 4 hours and the solvent was removed by rotator evaporator. The residue was column chromatographed to give pale yellow-coloured thick liquid products 1a-5a in 60-70 % yield. The reaction could not complete even after prolonged refluxing which leads to decomposition.

2.2.4 General procedure for the synthesis of 2, 2'-(ferrocenylmethylazanediyl)bis(N-alkylacetamide) (1b-5b)

N-benzyl-2-iodoacetamide (0.564 g, 2.05 mmol), *N*-cyclohexyl-2-iodoacetamide (0.547 g, 2.05 mmol), *N*-furfuryl-2-iodoacetamide (0.543 g, 2.05 mmol), *N*-4-methylbenzyl-2-iodoacetamide (0.592 g, 2.05 mmol) or *N*-4-methoxybenzyl-2-iodoacetamide (0.625 g, 2.05 mmol) was added portion wise to the solution of amino methyl ferrocene (0.215 g, 1 mmol) in 25 ml of CH_3CN containing Na_2CO_3 (0.265g, 2.5 mmol). The reaction mixture was refluxed for 6 hours. The similar workup procedure was adopted as described earlier to give yellow colored solid products 1b-5b in 80-90 % yield. These are outlined in scheme2.

Table 1. Micro-, mass- and IR analysis data for compounds **1a-5a** and **1b-5b.**

Entry	Molecular Formula	Molecular Weight	Yield (%)	MP (°C)	Elemental Analysis % Found (calculated)			IR data (KBr disc) υ_{max}/cm^{-1}
					C	H	N	
1a	$C_{20}H_{22}FeN_2O$	362	65	-	66.31 66.41	6.12 6.22	7.73 7.82	3209 (N-H), 3028(C-H), 2835 (C-H), 2603 (C-H), 1681(C=O), 1531, 1392, 1269, 1103, 1026, 894, 698, 659, 497, 482.
1b	$C_{29}H_{31}FeN_3O_2$	509	82	142	68.37 68.51	3.13 6.20	8.25 8.38	3448 (N-H), 3313(N-H), 2962 (C-H), 2920 (C-H), 1670 (C=O), 1639 (C=O), 1539, 1504, 1450, 1427, 1261, 1103, 1022, 802, 698, 482
2a	$C_{19}H_{26}FeN_2O$	354	60	-	64.42 64.50	7.40 7.46	7.91 7.98	471(N-H), 3163(C-H), 2800 (C-H), 1666(C=O), 1550, 1404, 1234, 1103, 1126, 910, 810, 648, 439
2b	$C_{27}H_{39}FeN_3O_2$	497	85	153	65.72 65.79	7.97 8.06	8.52 8.65	3321(N-H), 2931 (C-H), 2846 (C-H), 1681(C=O), 1643(C=O), 1535, 1450, 1315, 1253, 1103, 1026, 817,759, 493, 478
3a	$C_{18}H_{20}FeN_2O_2$	352	63	-	61.38 61.47	5.72 5.90	7.95 8.08	3201 (N-H), 2885 (C-H), 2816 (C-H), 1681(C=O), 1527, 1338,1265, 1018, 887, 810, 748, 655, 486
3b	$C_{25}H_{27}FeN_3O_4$	489	88	132	61.36 61.44	5.56 5.61	8.59 8.63	3340 (N-H), 2920 (C-H), 2850 (C-H), 1674 (C=O), 1651 (C=O), 1508, 1423, 1356, 1284, 1203, 1145, 1107, 1018, 756, 740, 474
4a	$C_{21}H_{24}FeN_2O$	376	61	-	67.03 67.12	6.43 6.49	7.44 7.53	3317 (N-H), 3086 (C-H), 3008 (C-H), 2835 (C-H), 2823 (C-H), 1658 (C=O), 1519, 1427, 1357, 1257, 1103, 1026, 810, 478
4b	$C_{31}H_{35}FeN_3O_2$	537	90	123	69.27 69.33	6.56 6.61	7.82 7.89	3360 (N-H), 3321(C-H), 2920 (C-H), 2854 (C-H), 1670 (C=O), 1639 (C=O), 1535, 1431, 1257, 1107, 1026, 840, 802, 752, 470
5a	$C_{21}H_{24}FeN_2O_2$	392	62	-	64.30 64.35	6.17 6.24	7.14 7.20	3308(N-H), 3081(C-H), 2931(C-H), 2834(C-H), 1655(C=O), 1513, 1460, 1301, 1247, 1176, 1105, 1133, 1001, 818, 484
5b	$C_{31}H_{35}FeN_3O_4$	569	92	170	65.38 65.47	6.20 6.29	7.38 7.42	3317(N-H), 3008(C-H), 2994(C-H), 2877(C-H), 1607(C=O), 1643(C=O), 1512, 1427, 1350, 1259, 1172, 1111, 1026, 840, 817, 594, 516, 478

Table 2. NMR spectral data for compounds **1a-5a** and **1b-5b.**

Entry	NMR Data (ppm)	
	^{1}H NMR ($CDCl_3$)	**^{13}C NMR ($CDCl_3$)**
1a	7.74 (s, 1H, -N*H*CO); 7.28-7.36 (m, 5H, *Ph*); 4.44 (d, *J* = 5.6 Hz, 2H, -C*H*$_2$CO); 4.14-4.43 (m, 9H, *Fc*); 3.64 (s, 2H, -C*H*$_2$Ph); 3.49 (s, 2H, -C*H*$_2$Fc)	176.5, 169.3, 137.9, 128.6, 127.7, 127.5, 82.1, 68.6, 50.2, 48.3, 43.2
1b	7.62(s, 2H, -N*H*CO); 6.94-7.37(m, 6H, Ph); 6.97 (d, 4H, Ph); 4.07-4.38 (m, 9H, *Fc*); 4.45 (s, 4H, -C*H*$_2$CO); 3.51(s, 4H, -C*H*$_2$Ph); 3.17 (2H, s, –C*H*$_2$ Fc)	170.1, 138.1, 128.7, 127.7, 127.5, 69.8, 68.6, 58.2, 55.1, 43.2, 30.9
2a	6.51 (s, 1H, -N*H*CO); 4.14-4.22(m, 9H, *Fc*); 3.62 (m, 1H, *Cy*); 3.40 (s, 2H,–C*H*$_2$Fc); 3.20(s, 2H,–C*H*$_2$CO); 2.08 (s, 1H, NH(-C*H*$_2$Fc) 1.19-1.90 (m, 10H, *Cy*).	168.1, 81.0, 68.6, 33.0, 32.8, 30.9, 25.4, 24.7, 21.6
2b	6.51 (s, 2H, N*H*CO); 4.12-4.17(m, 9H, *Fc*); 3.78 (m, 2H, *Cy*); 3.54 (s, 2H,–C*H*$_2$ Fc); 3.12 (s, 4H,–C*H*$_2$ CO); 1.12-1.91(m, 20H, *Cy*)	169.3, 81.8, 69.8, 68.6, 58.2, 55.1, 47.8, 33.08, 30.9, 25.4, 24.7
3a	7.64 (s, 1H, N*H*CO) ; 7.28 (d, *J* = 0.8 Hz, 1H, *furyl*); 6.34 (t, *J* = 2 Hz, 1H, *furyl*) ; 6.23 (d, *J* = 2.8 Hz, 1H, *furyl*); 4.14-4.19 (m, 9H, *Fc*); 4.44 (s, 2H, -C*H*$_2$furyl); 3.59 (2H, s, –C*H*$_2$Fc); 3.42(s, 2H, –C*H*$_2$CO)	170.0, 151.1, 142.2, 110.4, 107.4, 83.3, 68.5, 50.6, 48.4, 36.1
3b	7.37 (d, *J* = 0.8 Hz, 2H, *furyl*); 6.89 (s, 2H, N*H*CO) ; 6.34 (t, *J* = 1.2 Hz, 2H, *furyl*); 6.23(s, *J* = 2.8 Hz, 2H, *furyl*); 4.42 (s, 4H, -C*H*$_2$furyl); 4.05-4.12 (m, 9H, *Fc*); 3.50 (2H, s, –C*H*$_2$Fc); 3.17(s, 4H, –C*H*$_2$CO).	170.1, 151.1, 142.1, 110.5, 107.3, 81.4, 68.6, 58.0, 54.9, 36.1, 30.9
4a	7.50(s, 1H, -N*H*CO); 7.13-7.49 (m, 4H, *Ph*); 4.42 (d, *J* = 6 Hz, 2H, -C*H*$_2$CO); 4.08-4.16 (m, 9H, *Fc*); 3.47 (s, 2H, -C*H*$_2$Ph); 3.33(s, 2H, -C*H*$_2$Fc); 2.34(s, 3H, C*H*$_3$).	170.5, 137.1, 135.1, 129.3, 127.7, 68.5, 51.0, 48.9, 42.8, 21.1
4b	7.141(m, 5H, *Ph*); 6.9(s, 1H, -N*H*CO); 3.98-4.35 (m, 9H, *Fc*); 4.35 (s, 2H, -C*H*$_2$CO); 3.56 (s, 2H, -C*H*$_2$Ph); 3.19 (s, 2H, -C*H*$_2$Fc); 2.36 (s, 3H, C*H*$_3$)	166.7, 137.3, 134.3, 129.4, 127.8, 44.2, 21.1
5a	7.50(s, 1H, -NHCO); 7.2(d, *J* = 8.8 Hz, 2H, BZ); 6.8(d, *J* = 8.7 Hz, 2H, *Ph*); 6.84- 4.30 (d, *J* = 6.0 Hz, 2H, -C*H*$_2$CO); 4.01-4.32 (m, 9H, *Fc*); 3.96 (s, 3H, -OC*H*$_3$); 3.74 (s, 2H, -C*H*$_2$Ph); 3.23 (s, 2H,–C*H*$_2$Fc).	170.7, 158.8, 130.5, 129.1, 114.0, 84.5, 81.6, 68.5, 55.3, 51.2, 48.8, 42.4
5b	7.59 (s, 2H, -N*H*CO); 7.2(d, *J* = 8.8 Hz, 2H, *Ph*); 7.1 (d, *J* = 8.7 Hz, 2H, *Ph*); 6.84-7.27 (m, 4H, *Ph*); 4.35 (d, 4H, -C*H*$_2$CO); 4.05-4.30 (m, 9H, *Fc*); 3.97 (s, 6H, -OC*H*$_3$); 3.79 (s, 4H, -C*H*$_2$Ph); 3.15 (s, 2H,–C*H*$_2$ Fc)	170.0, 138.1, 128.7, 127.7, 127.5, 69.8, 68.6, 58.2, 55.1, 43.2, 30.9

2.3 Biological assay

2.3.1 In vitro Cytotoxicity Assay

To observe *in vitro* cytotoxicity of newly synthesized amide functionalized 2º- and 3º-aminomethylferrocene inhibitors 1A-5A and 1B-5B holding biologically relevant groups such as ferrocene, 2º-/ 3º-amino, and amidic moieties, MTT assay was performed. Breast cancer cell line (MCF 7), Neuroblastoma cell line (IMR 32), Hepatocellular carcinoma cell line (HepG2) and immortal lung cell line (L132) were procured from the NCCS, Pune. Cells were cultured in required culture medium with supplementation of 10% FBS and incubated at 37℃. For cytotoxicity study, cells were seeded in 96 well plate (8000 cells per well) and incubated overnight for adhesion then treated by synthesized ligands for 24 hours with five different concentrations. Cells were exposed to MTT solution (5mg/ml) for 5 hours at 37℃. The formazon crystals, formed by mitochondrial activity of live cell, were dissolved in 200µl of DMSO. Optical density was measured at 540nm using plate reader. Percent inhibition due to exposure of synthesized ligand at each concentration was calculated and IC_{50} values (Inhibition concentration 50) were derived. Cisplatin was used as a reference drug.

2.3.2 Apoptosis assay

Using dual staining method, the apoptotic effect of highly active ligands 1b, 4b and 5b was detected. Acridine orange (AO; live cell staining) and ethidium bromide (EtBr; stains dead cells) stained were used to observe apoptotic cell death induced by synthesized ligand. HepG2 cells were grown on Poly-L-Lysine coated coverslip in 6 well plates. After overnight incubation, adhered cells were exposed to 1b, 4b and 5b, then incubated for 24 hours. Cells were stained by AO: EtBr (4:1) for 10 minutes, then washed with PBS and observed under the fluorescent microscope.

2.3.3 Gene Expression study

Modulation of transcript expression, on the exposure of synthesized ligands to cells, was estimated using RT-PCR. For gene expression study, cells were exposed by synthesized ligand for 24 hours and RNA was isolated using Trizol reagent. RNA was quantified using NanoDrop spectrophotometer. RNA was reverse transcribed using cDNA synthesis kit. Using Power up SYBR Green mix (Invitrogen), Real Time PCR was performed to measure the variation in mRNA expression. To analyze transcript expression modulation variation in mRNA expression, mitochondrial dependent cell death genes (or apoptotic), anti-proliferative genes (or proliferation regulatory genes) were selected to illuminate the regression

mechanism of cancer. β-actin was used as the housekeeping gene. The mRNA level of p53, Bax, Bcl2, tubulin, TNFR1, cIAP1, p38MAPK and caspase-9 expression were estimated. The primer was designed using BLAST software of NCBI. p53-F: 5'CATAGTGTGGTGGTGCCCTA3', R: 5'CACCTCAAAGCTGTTCCGTC3'; Bcl-F: 5'GCC CGGAACCTAATGGCTT3', R: 5'CTCAGGGACTCACTCTGCTG3'; Bax-F: 5'GCCCTTTTG CTTCAGGGTTT3', R: 5'GGAAAAAGACCTCTCGGGGG3'; Caspase9-F: 5'ATGGACG A AGCGGATCGG3',R:5'CCCTGGCCTTATGATGTT3'; p38MAPK-F:5'ACCCTGGATGACTTCA CGGA3'; R:5'CGGCAGCGTGGATATACCT3'; Tubulinα-F:5'GAAGCGCAACCATGCGTG A3',R:5'GTGCCAGTGCGAACTTCATC3'; CDK-F:5'TTCAGTGGGCTTTTCTGGCA3', R:5' GAAGGACTGTGTTGTGCAGC3'; cIAP1-F:5'ATTGGATTCGGAAGCCCCAA3', R:5' TTAAAAGAACGCCGAGGGCT3'; TNFR1-F5' GGGGACAGGGAGAAGAGAGA3', R:5'TTGTGGCACTTGGTACAGCA3'; TNFα-F: 5'TGGGATCATTGCCCTGTGAG3', R:5'GGTGTCTGAAGGAGGGGGTA3' and β-actin-F:5'CCACCATGTACCCTGGCATT3', R:5'CG CTCAGGAGGAGCAATGAT3'. For each target gene expression, the ΔCt values (ΔΔCt) and the relative linear amount of target molecules, relative to the calibrator was calculated as 2ΔΔCt. Fold change of transcript expression was analysed.

2.3.4 Western blot analysis

HepG2 cells were exposed by ligands 4b and 5b for 24 hours with concentration of 3.5 μM and 1 μM respectively. Cell lysate of HepG2 cells were prepared using denaturing buffer and centrifuge for 30 minutes at 2000 rpm at 4°C. Supernatant was collected and protein concentration was measured using Barfoed reagent. Protein samples were separated using 10%SDS gel at 100V and transferred to PVDF membrane at 100V for 60-70 minutes. Membrane was blocked for unspecific binding for 1 hour at room temperature with PBS containing 0.1% Tween-20 and 5%BSA thereafter incubated over night with primary antibody rabbit anti TNFR1 (CST), rabbit anti phopho-p38MAPK (Invitrogen), rabbit anti cIAP1 and rabbit anti β-actin (Novus Biologicals) followed by incubation with horseradish peroxidase (HRP) conjugated anti-rabbit IgG secondary antibody (Invitrogen) for 1 hour at room temperature. The labelled proteins were developed using ECL prime system (GE Healthcare) for detection.

2.3.5 Mitochondrial Membrane potential (MMP)

Change in mitochondrial membrane potential was observed using JC-1 dye. Loss of membrane potential escorts the cell for mitochondrial dependent programmed cell death.

HepG2 cells were exposed to ligands 4b (3.5 μM) and 5b (1 μM) for 24 hours. Post incubation, cells were washed by PBS and incubated at 37°C for 10 minutes with JC-1 stain in the dark. Cells were washed twice with buffer and observed under fluorescent microscope.

Statistical Analysis

Each experiment was repeated at least 3 times. Statistical significance was assessed by comparing mean values (± SE) using one-way analysis of variance (ANOVA) followed by post hoc Bonferroni's test and was assumed for $p<0.05$ (*), $p<0.01$ (**). Pearson's correlation coefficient was used to determine the correlation between cIAP1 and TNFα/TNFR1 as well as caspase 9 and Bcl2/ Bax mRNA levels.

2.4 Molecular docking study

2.4.1 Ligand preparation

The 2D structures of ligands were drawn in ChemDraw 19.0 and the molecules were converted into 3D in ChemBio 3D. The energy minimization of all the lead molecules are done by MM2 based minimization, CDX format are converted into PDB format by using Open Babel (OBGUI) software. [15] All the ligands were assigned charges and torsions and converted to PDBQT in AutoDock 4.0 (The Scripps Research Institute) with CYGWIN-64. [16]

2.4.2 Protein preparation and Grid Parameters

The crystal structure of protein 1TNF is downloaded from RCSCB Protein Data Bank basing on the factors like RMSD, Resolution factor. The protein was prepared by Swiss PDB Viewer (SPDBv4.0). The crystal contacts and RMSD of prepared protein were elucidated by Ramchandran Plot and Hydrophobicity Plot. The binding site of the protein was predicted by Super Computing Facility at IIT-Delhi. The assigned Grid Co-ordinates of the active site X:22.534 Y: 53.169 Z: 40.421, the ligands were also blind docked with complete Chain-A of 1TNF as binding pocket.

2.4.3 Auto Dock 4.0

Docking was performed using rigid docking the auto dock 4.0. All the ligands were screened for their efficient fitting into the receptor (minimized) grid and all the docking parameters including binding energy were calculated with optimized RMSD. The ligands were screened with 10 possible minimum energy confirmations.

2.4.4 Visualization of residues Interaction

The lead ligands interact with active site either by Hydrogen bonding or by Hydrophobic Interactions. All the post processing was done using Discovery Studios & or with ICM-Pro software of Molsoft.com.

2.4.5 Pharmacokinetic study

Lead Identification

Traditionally Log P values are used to assign the drug absorption through the lipid bilayer. The ligands were screened for its Drug Likeness by studying the Molecular Properties of Ligands by ADMET analysis and screened by Lipinski and Veber filters however the usage of Log P values may attribute false negative results as Log P is the ratio. Here, we used 2 models to elucidate the permeability of lead molecules which uses hydrogen bonding functionality obtained calculating PSA & TPSA in addition to Log P. Pharmacokinetic profiling of designed leads was executed by ADMET plot provided by Discovery Studios 20 & Swiss-ADME plot. [17] Proposed Model with descriptors Atom-based Log P98 (ALogP98) and two-dimensional PSA (PSA2D) with a plot comprising 95% and 99% confidence interval were used to predict the lead molecules cell permeability. The compound with optimum cell permeability should follow the criteria PSA < 140 $Å^2$ and AlogP98 < 5. All of the compounds showed best fit to the proposed model.

Quantitative Structure Toxicity Relationship-QSTR

Optimization of designed molecules is given at most preference to minimize the toxicity and maximize the potency of designed leads. Quantitative Structure Toxicity Relationship was predicted for the designed lead molecules from its chemical structure using toxicity profiling module (TOPKAT) of Biovia's Discovery Studios.[17a] Structurally similar hits were screened using TOPKAT; where Bayesian Score; Mahalanobis Distance parameters of descriptors used to validate QSTR model and all lead molecules are non-toxic and non-carcinogenic.

2.5 RESULTS AND DISCUSSION

2.5.1 Synthesis and Characterization

It is worth noting that ferrocenylmethyamine did not react with α-chloroamide precursors CA1-CA5, unlike others[18] to give desired products. The α-chloroamide precursors CA1-CA5 were then converted to α-iodoamide precursors IA1-IA5, which were indeed reacted with ferrocenylmethyamine to give a new series of amide functionalized

ferrocenylmethylamine derivatives 1a-5a, 1b-5b in moderate to high yield (Scheme 2). Using the optimized reaction conditions, we tested the scope of this procedure and established the best reaction conditions for the selective formation of mono-amide functionalized 2º-aminomethylferrocene 1a-5a and diamide functionalized 3º-aminomethylferrocene 1b-5b which contain promising ferrocenyl, amino and amido groups in the molecular framework.

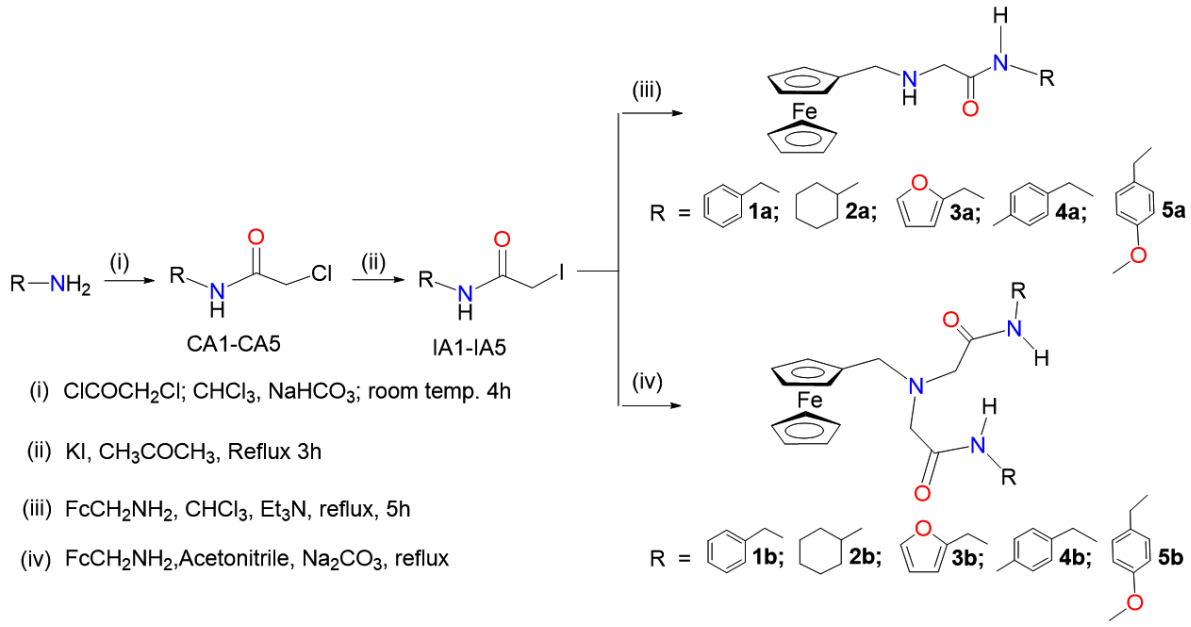

Scheme 2. General synthetic strategies adopted for 2-(ferrocenylmethylamino)-N-alkylacetamide (1a-5a) and 2, 2'-(ferrocenylmethylazanediyl)-bis-(*N*-alkylacetamide) (1b-5b).

Newly synthesized amide functionalized 2º-ferrocenemethylamine 1a-5a were isolated in a thick liquid form while 3º- aminomethylferrocene 1b-5b were isolated as solid. All the ligands are fairly soluble in common organic solvents and found to be stable in the pure state and in the solution over a period of days. The compositions and phase purity of the samples were confirmed by microanalysis and by ^{1}H and ^{13}C spectroscopy. The NMR (Annexures 1-20) and IR spectra (Annexures 21-30) gives confirmation of various groups viz. ferrocenyl, amino- amido-, alkyl- and aryl present in 1a-5a, 1b-5b. The assigned IR and NMR data are summarized in the experimental section. Ferrocene appears in the range of 3.98-4.43 ppm in the ^{1}H NMR spectrum of 1a-5a, 1b-5b. Notably, di-amide functionalized 3º-aminomethyl ferrocene 1b-5b show two different CO stretching frequencies in 1681-1640 cm^{-1} region (Annexures 22, 24, 26, 28 30) due to the involvement of one of the amidic CO in intermolecular hydrogen bonding as revealed by X-ray diffraction study (vide infra).

The UV-visible spectral spectrum of all ligand gives a high intensity absorption bands in the region of 300-324 nm **(**Figure 1**)** which is mainly attributed to the locally excited n→π* transitions. A broad, low intensity band observed in the 430-439 nm region attributable to

metal (LMCT) charge transfer transitions, a characteristic feature of attached ferrocene moiety.[11]

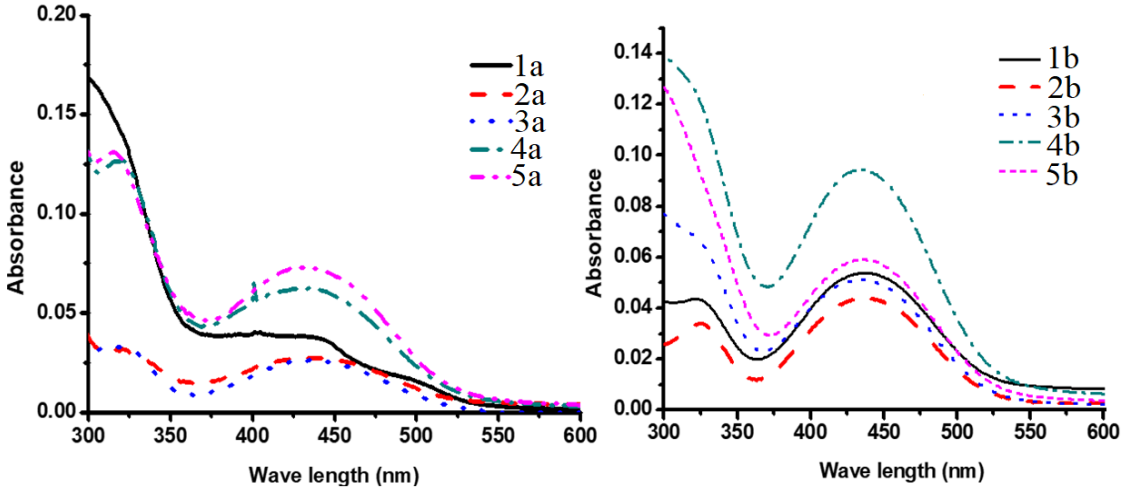

Figure 1. UV-visible absorption spectrum of the compounds under investigation at room temperature in 10^{-5} M CH_3CN.

The majority of the ligands fluoresces in the visible region of upon excitation in the ultraviolet region with a concomitant Stokes shift of 60-100 nm **(**Figure 2, Table 3**)**.

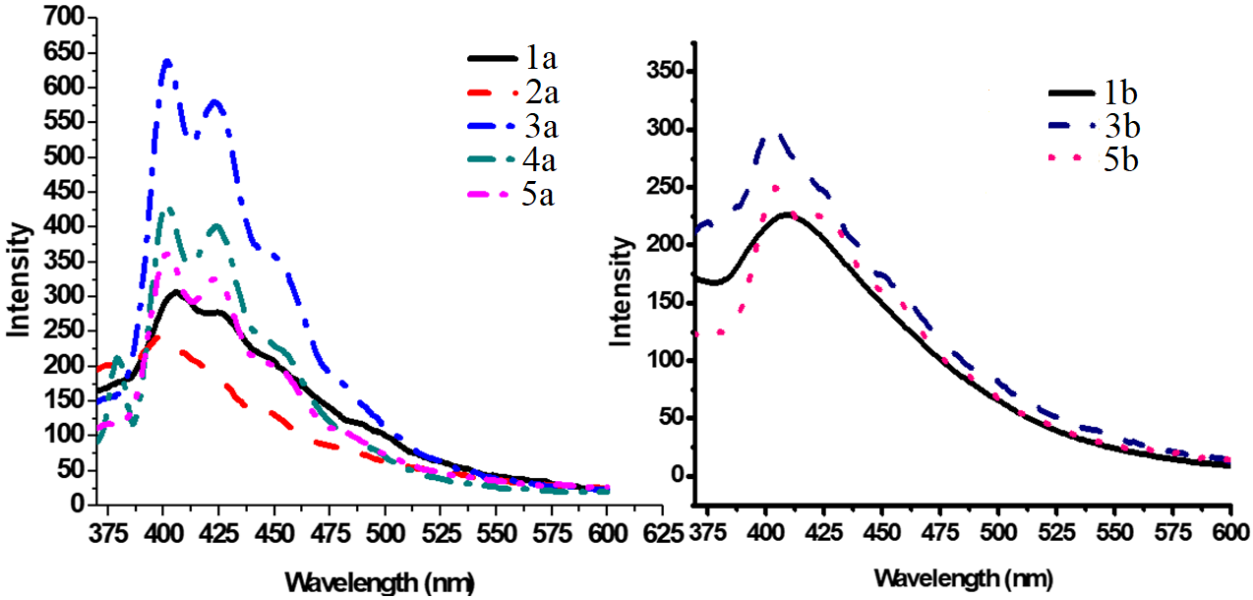

Figure 2. Fluorescence spectrum of compounds under investigation at room temperature in 10^{-5} M CH_3CN solution.

Table 3. UV-visible and fluorescence bands for compounds under investigation.

Entry	UV-Visible data (10^{-5} CH_3CN) λ_{max} nm (ε L Mol^{-1} cm^{-1})	Wave number cm^{-1}	Fluorescence spectruml data (10^{-5} M CH_3CN)	
			λ_{ex} (nm)	λ_{em} nm (Intensity)
1a	322 (4360) n→ π*, 437(5380) CT	31055, 22883	320	406 (306), 425(276) CT
1b	324 (4344) n→ π*, 439(5394) CT	30864, 22779	325	409 (225) CT

2a	321(3100) n→ π*, 437(2749) CT	31152, 22883	320	400 (246) CT
2b	323(3391) n→ π*, 435(4386) CT	30959, 22988	-	-
3a	318(3276) n→ π*, 435(5134) CT	31446, 22988	325	402 (638), 422 (579) CT
3b	321(6770) n→ π*, 434(5107) CT	31152, 23041	325	401 (302) CT
4a	319(1265) n→ π*, 430(6216) CT	31347, 23255	342	401 (432), 424 (400) CT
4b	305(1357) n→ π*, 434(9408) CT	23041	-	-
5a	315 (1310) n→ π*, 433(7330) CT	31746, 23094	325	401 (362), 424 (325) CT
5b	300 (1260) n→ π*, 436(5933) CT	22935	325	403 (249), 426 (246) CT

2.5.2 Thermogravimetric Analysis of 1a-5a and 1b-5b

The DTA curves (Figure 3) show an endothermic peak at 142.8 °C (for 1b), 153. 7°C (for 2b), 131.7 °C (for 3b), 123.3 °C (for 4b) and 170.0 °C (for 5b), respectively, without any mass loss on DTG curves and these peaks attributes to the melting point of the ligands. Notably, TGA curves of 1b-5b essentially show one-step decomposition in the 200−550 °C temperature range with weight loss of 76.4, 75.4, 60, 64.4 and 67.0% respectively, leaving the residue of Fe_2O_3 in each case (Table 4). The ability of these ligands to form Fe_2O_3 may be a factor for their enhanced anti-proliferative activity at low micro molar concentration (vide infra). Evidently, the possible toxicity study of Fe_2O_3 in human cells, including blood lymphocytes indicated that Fe_2O_3 significantly reduced the cell viability and at different concentrations Fe_2O_3 NPs affect cellular glutathione (GSH) level and cause oxidative stress in human lymphocytes.[19]

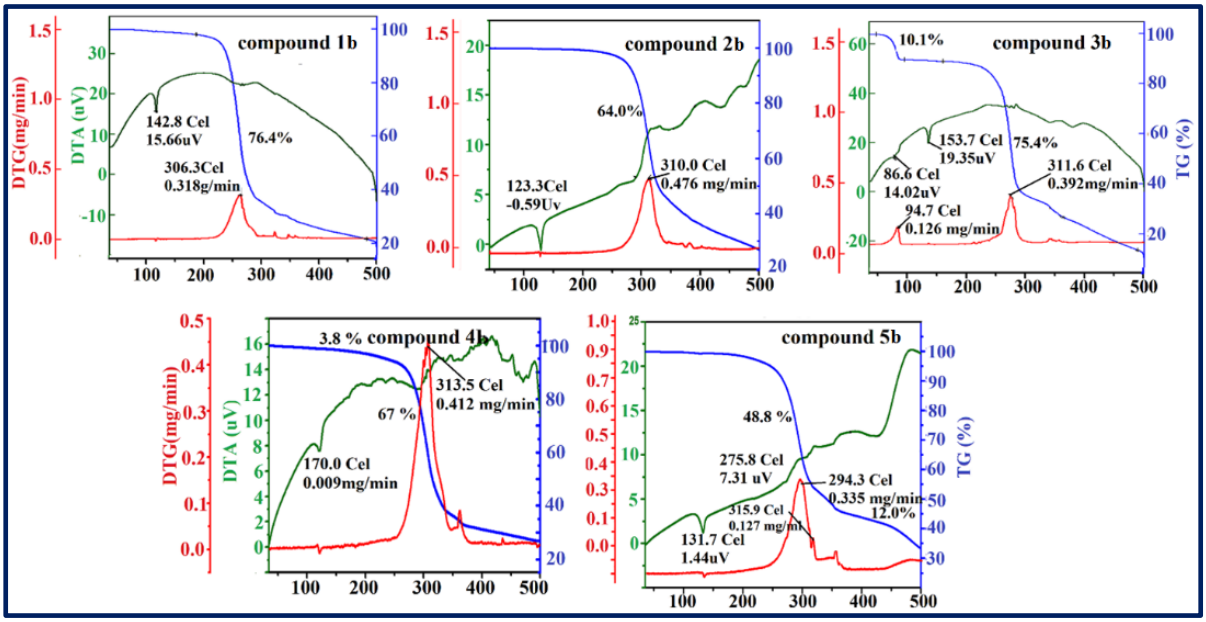

Figure 3. TG/DTA curves for the ligands 1b-5b.

Table 4. TGA results for the ligands 1b-5b.

ligand	T (°C) in DTA	T (°C) in TGA	residue wt. observed (Calcd.) (%)	expected product of decomposition
1b	142.8	220	0.0 (phase transition)	-
	-	220-550	23.6 (31.4)	Fe_2O_3
2b	153.7	200	0.0 (phase transition)	--
	-	200-550	24.6 (32.5)	Fe_2O_3
3b	131.7	200	0.0 (phase transition)	--
	-	200-550	39.2 (32.8)	Fe_2O_3
4b	123.3	210	0.0 (phase transition)	--
	-	210-550	36 (29.8)	Fe_2O_3
5b	170.0	180	0.0 (phase transition)	--
	-	200-550	33 (28.2)	Fe_2O_3

2.5.3 X-ray crystallographic study

The liquid samples of 1a and 3a, which contain 2º amine moieties were crystallized in the salt form in triclinic P-1 (1a.*2HI.H₂O*) and monoclinic Cc (3a.*CH₃COOH*) space groups, respectively. Solid samples crystallize in monoclinic $P2_1/c$ (3b, 4b) and triclinic P-1 (5b) centrosymmetric space groups. X-ray crystal structure shows one complete molecule in their asymmetric units, except 1a.*2HI.H₂O* and 5b which contains two complete molecules in their asymmetric units. The *ORTEP* view at 50 % probability for these compounds is shown in Figure 4. Details about data collection, refinement, and structure solution are recorded in (Table 5) and selected geometrical parameters are in the beneath of Figure 4.

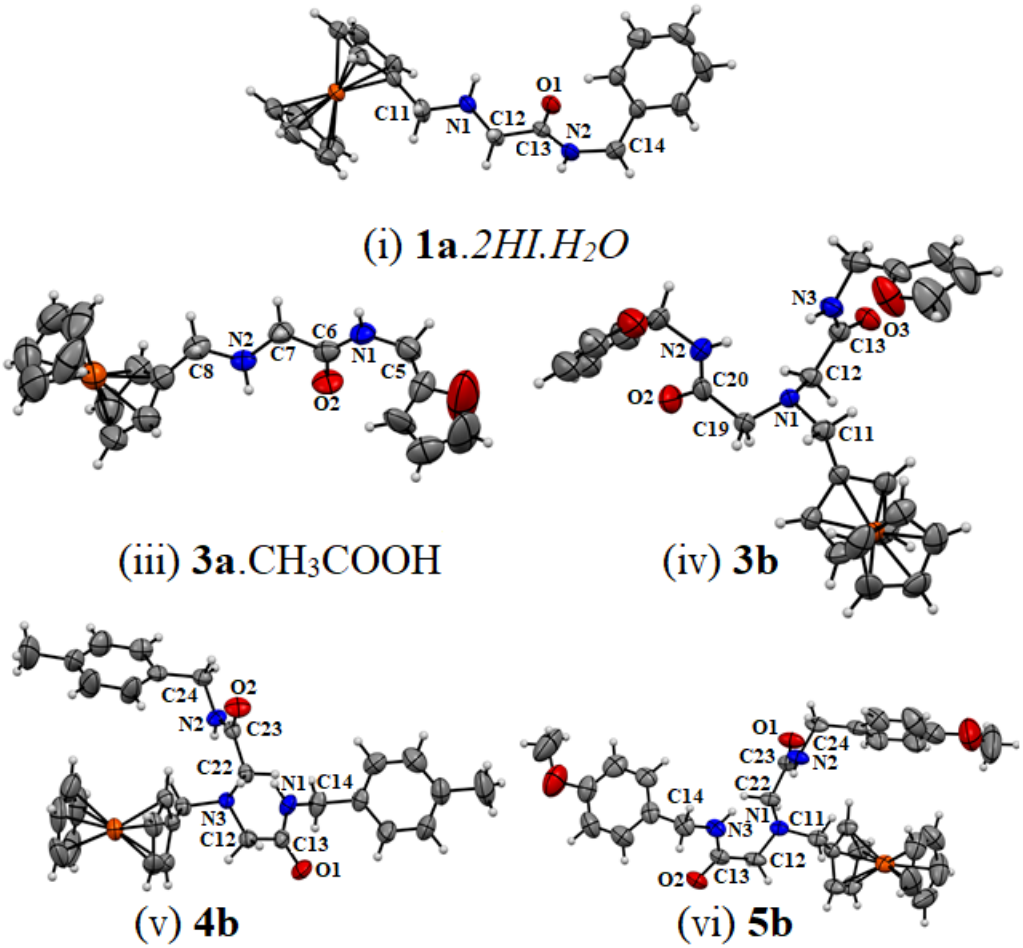

Figure 4. The ORTEP diagram with partial atom numbering showing 50 % probability ellipsoid; (hydrogen atoms and solvent molecules from 1a and 3a are removed for clarity) for (i) **1a**.*2HI.H₂O*, selected bond lengths (Å): N1–C11, 1.468(6); N1–C12, 1.482(5); C13–C12, 1.509(6); C13–O1, 1.230(5); C13–N2, 1.321(6); (ii) **3a**.*CH₃COOH*, selected bond lengths (Å): N2–C8, 1.506(11); N2–C7, 1.507(10); C6–C7, 1.520(12); O2–C6, 1.235(10); N1–C6, 1.326(11); (iii) **3b**, selected bond lengths (Å): N2–C21, 1.451(7); N2–C20, 1.338(8); O2–C20, 1.215(7); C19–C20, 1.511(8); N1–C19, 1.452(7); (iv) **4b**, selected bond lengths (Å): N2–C24, 1.447(4); N2–C23, 1.318(4); O2–C23, 1.234(3); C23–C22, 1.510(4); N3–C22, 1.461(3); (v) **5b**, selected bond lengths (Å): C14–N3, 1.460(7); N3–C13, 1.345(7); O2–C13, 1.221(6); C12–C13, 1.510(8); N1–C12, 1.462(6).

Table 5. Crystal data and structure refinement for compounds 1a, 3a, 3b, 4b and 5b.

Identification code	**1a. *2HI. H_2O***	**3a. *CH_3COOH***	**3b**	**4b**	**5b**
CCDC Number	1915120	1915118	1915119	1915121	1915123
Formula	$C_{40}H_{48}Fe_2I_2N_4O_3$	$C_{20}H_{24}FeN_2O_4$	$C_{25}H_{27}FeN_3O_4$	$C_{31}H_{35}FeN_3O_2$	$C_{31}H_{35}FeN_3O_4$
Formula weight	998.32	412.26	490.35	537.49	569.47
Temperature/K	293	293(2)	293	293.00(10)	293
Crystal system	Triclinic	Monoclinic	Monoclinic	Monoclinic	Triclinic
Space group	P-1	Cc	$P2_1/c$	$P2_1/c$	P-1
a/Å	7.4660(3)	6.1657(13)	11.296(2)	16.6561(12)	9.5112(12)
b/Å	9.8940(3)	31.742(6)	23.105(3)	17.7316(18)	17.1975(13)
c/Å	28.6567(9)	10.347(2)	9.474(2)	9.3941(8)	18.6246(19)
α/°	87.795(2)	90	90	90	104.797(8)
β/°	86.532(3)	91.726(19)	112.32(3)	92.819(7)	101.581(10)
γ/°	72.015(3)	90	90	90	90.062(8)
Cell volume/$Å^3$	2009.27(12)	2024.1(7)	2287.5(8)	2771.1(4)	2881.0(5)
Z	2	4	4	4	4
$\rho_{calc}g/cm^3$	1.65	1.353	1.424	1.2882	1.315
μ/mm^{-1}	2.3	0.772	0.697	0.576	0.563
F(000)	996.0	864	1028	1137.8	1200
Crystal size/mm^3	0.4 × 0.3 × 0.2	0.6 × 0.2 × 0.1	0.3 × 0.2 × 0.15	0.9 × 0.6 × 0.4	0.5 × 0.3 × 0.2
Completeness to theta (%)	(θ = 72.16) 100	(θ = 27.36) 96.27	(θ = 25.00) 99.8	(θ = 26.08) 99.7	
Radiation	MoKα (λ = 0.71073)	MoKα (λ = 0.71073)	MoKα (λ = 0.71073)	Mo Kα (λ = 0.71073)	MoKα (λ = 0.71073)
2Θ range for data collection/°	6.04 to 57.98	6.48 to 57.56	5.96 to 58.4	6.32 to 58.14	6.4 to 58.02
Index ranges	$-10 \le h \le 9$, $-12 \le k \le 12$, $-38 \le l \le 37$	$-8 \le h \le 8$, $-41 \le k \le 42$, $-9 \le l \le 13$	$-12 \le h \le 15$, $-26 \le k \le 29$, $-12 \le l \le 5$	$-22 \le h \le 20$, $-24 \le k \le 12$, $-12 \le l \le 9$	$-12 \le h \le 12$, $-22 \le k \le 23$, $-25 \le l \le 23$
Reflections collected	16892	4702	6433	12751	23241
Independent reflections	9071 [R_{int} = 0.0239, R_{sigma} = 0.0426]	3011 [R_{int} = 0.0454, R_{sigma} = 0.0792]	4857 [R_{int} = 0.0422, R_{sigma} = 0.1129]	6366 [R_{int} = 0.0461, R_{sigma} = 0.0907]	13012 [R_{int} = 0.0673, R_{sigma} = 0.1182]
Data/restraints/parameters	9071/0/463	3011/38/245	4857/4/274	6366/0/336	13012/0/707
Goodness-of-fit on F^2	1.042	1.009	1.028	1.037	1.046
Final R indexes [I>=2σ (I)]	R_1 = 0.0483, wR_2 = 0.1216	R_1 = 0.0628 (0.0792), wR_2 = 0.1356	R_1 = 0.0854, wR_2 = 0.1919	R_1 = 0.0669, wR_2 = 0.1216	R_1 = 0.0992, wR_2 = 0.2511
R indexes [all data]	R_1 = 0.0698, wR_2 = 0.1337	R_1 = 0.1203, wR_2 = 0.1701	R_1 = 0.1563, wR_2 = 0.2509	R_1 = 0.1300, wR_2 = 0.1474	R_1 = 0.1702, wR_2 = 0.3019
Larg. diff. peak/hole /$eÅ^{-3}$	0.92/-0.83	0.46/-0.22	1.17/-0.71	0.76/-0.74	1.19/-0.67

The structural parameters such as bond lengths and bond angles are found to be consistent with the literature.[10, 20] Notably, X-ray crystallography revealed the propensity of amidic and amine groups of newly synthesized amines to form intermolecular hydrogen bonding (Figure 5).

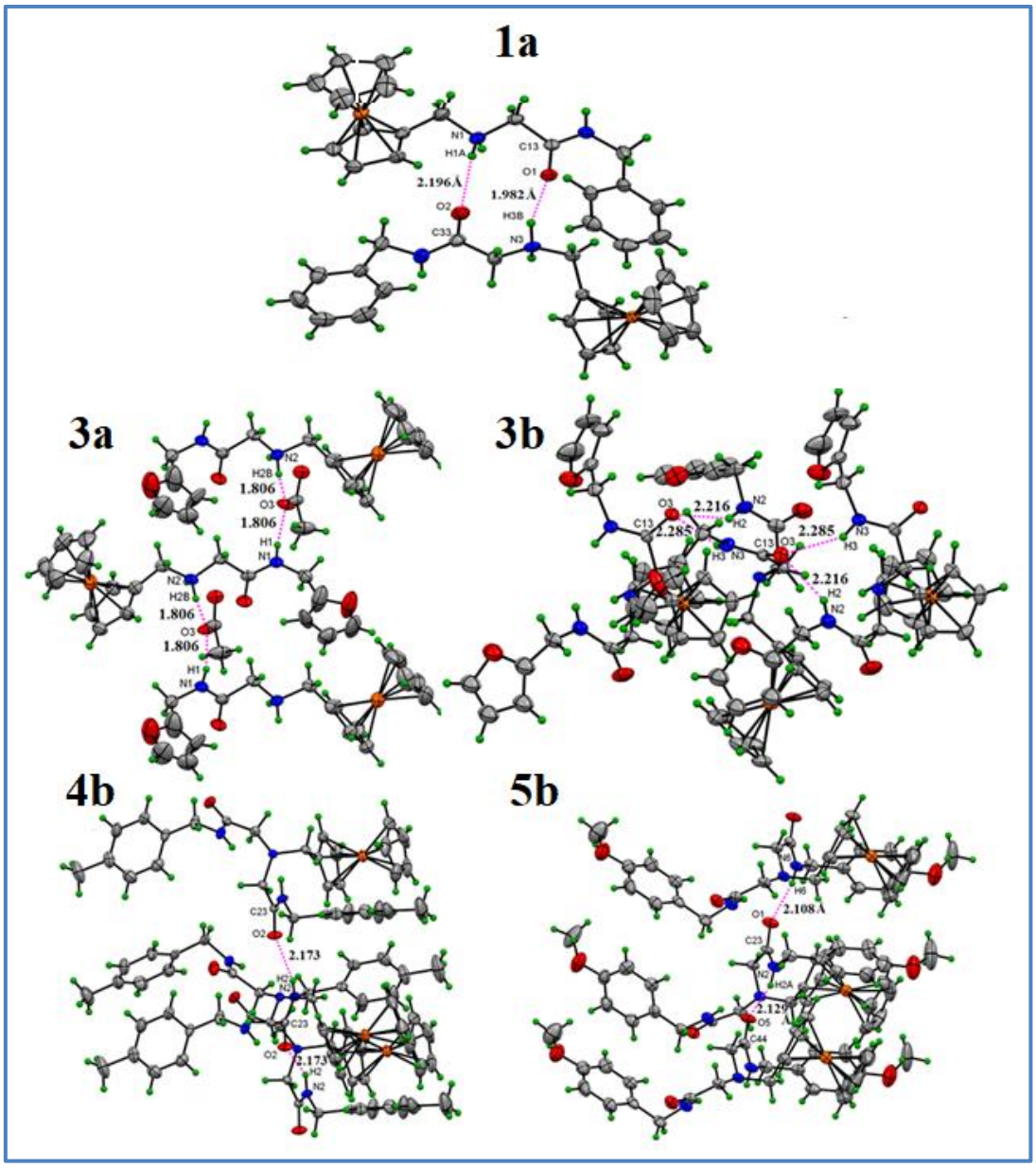

Figure 5. Crystallographic study reveals the propensity of synthesized ligand to form inter molecular H-bonding.

2.5.4 Hirshfeld surface analysis

Hirshfeld surface analysis was employed to understand and quantify the noncovalent interactions e.g. hydrogen bonding, π-forces and the details are summarized. The fingerprint plots of close contacts (Figure 6) confirms both strong and weak intermolecular interactions. The relative contributions of the intermolecular contacts in 1a, 3a, 3b, 4b and 5b are given in Table 6. The bar graph pf relative contribution of the intermolecular contacts shows in Figure 7. This indicates the ability of these molecules to offer secondary interaction in the biological system required for cell growth inhibition. To reveal the inhibitory influence of various substituents at the amidic scaffold of 1a-5a and 1b-5b, interactions of these with 1tnf protein was carried out using molecular docking for further study on lead molecules.

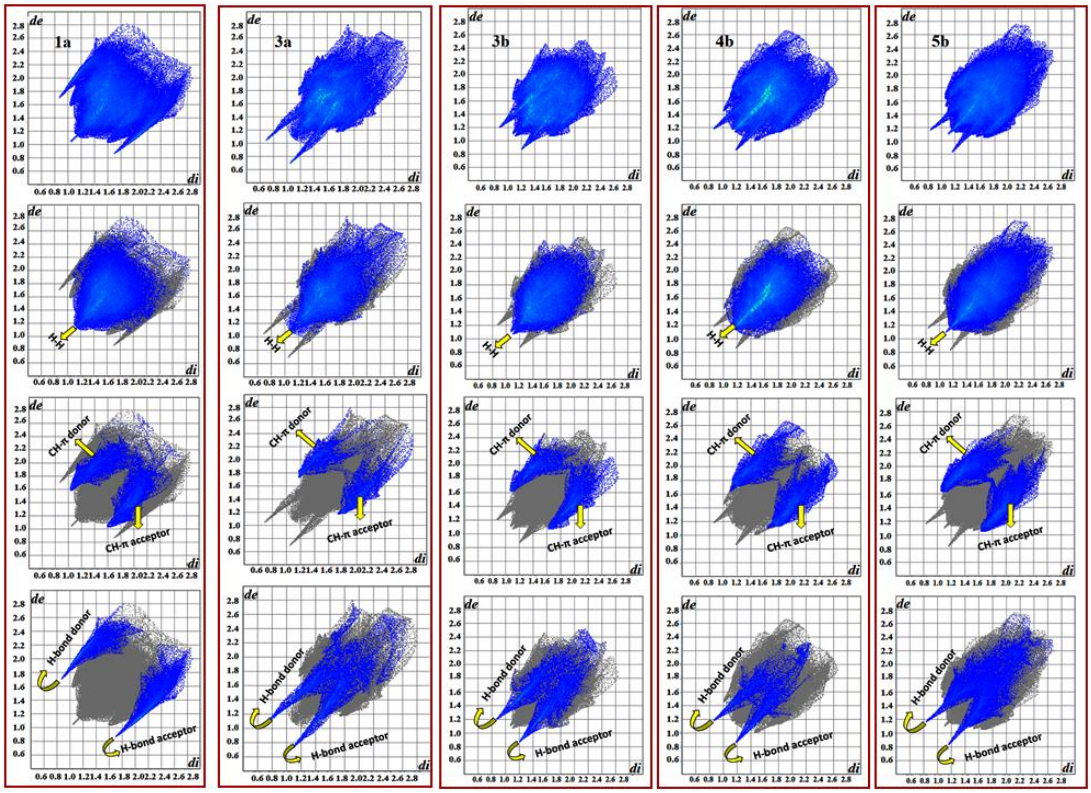

Figure 6. Decomposed Hirshfeld fingerprint plots for 1a, 3a, 3b, 4b and 5b. Specific contacts are highlighted, while the entire 2D fingerprint is shown in gray. Close contacts are labelled H…H, CH…π and O…H contacts and their reciprocal.

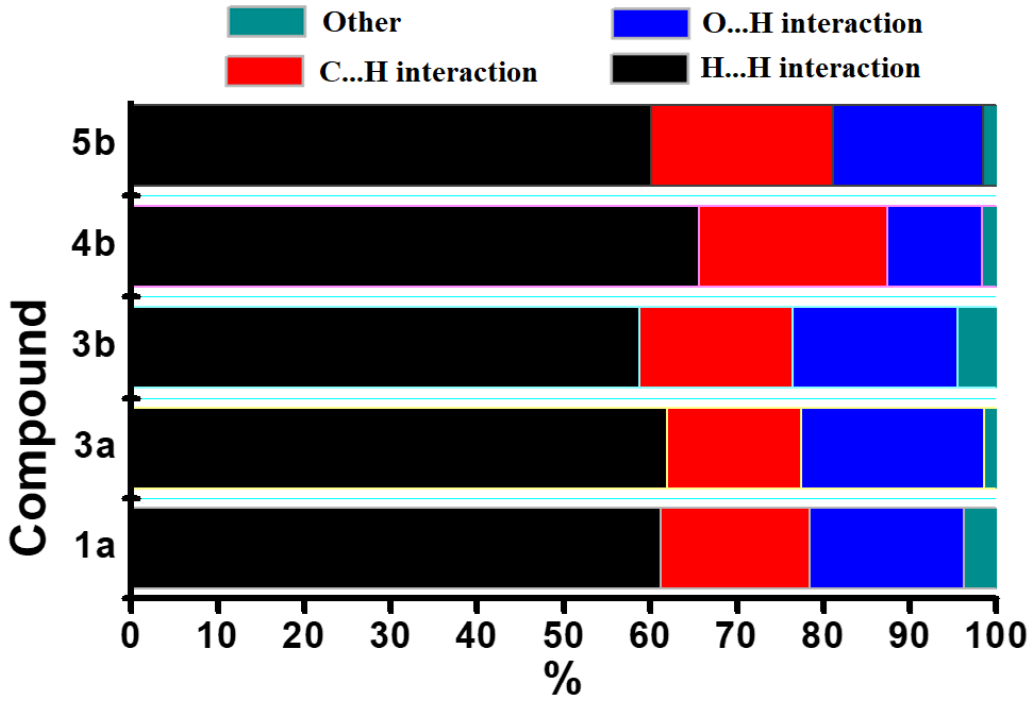

Figure 7. Demonstration of relative contributions of the intermolecular interactions to the Hirshfeld surface for the compounds 1a, 1b, 3a, 3b, 4b and 5b [%].

Table 6. Relative contributions of the intermolecular interactions to the Hirshfeld surface for
the compounds 1a, 3a, 3b, 4b and 5b [%].

Nature of contacts	1a	3a	3b	4b	5b
H-H interaction (%)	61.2	62	58.8	65.6	60.1
C-H interaction (%)	17.3	15.5	17.6	21.8	21
O-H intraction (%)	17.8	21.1	19.2	11	17.4
Other (%)	3.7	1.4	4.4	1.6	1.5

2.5.5 Theoretical Investigations

2.5.5.1 Density functional theory calculations

DFT level calculations and full geometry optimization of some representative compounds 1a-5a and 1b-5b have been executed using B3LYP/LanL2DZ basis sets. DFT calculations have been widely used in recent years due to its ability to provide reasonably good results for large molecular structures. All the calculations are performed using the Gaussian16 program suite and molecular orbitals were generated by GaussView 6.0 program. The density functional calculations have appeared in good support to the experimentally determined similar parameters. The structural parameters such as bond lengths and bond angles assumed for 1a-5a and 1b-5b obtained theoretically were found to be consistent with the similar parameters

obtained experimentally by X-ray study. An optimized geometry for the minimum energy conformation of 1a-5a and 1b-5b are given in Figure 8. Energy of optimized geometry and HOMO-LUMO gaps for compounds 1a-5a and 1b-5b have summarized in Table 7.

1a

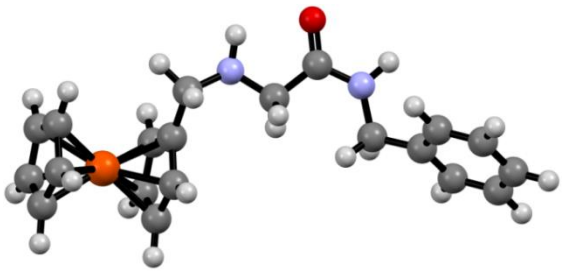

1b

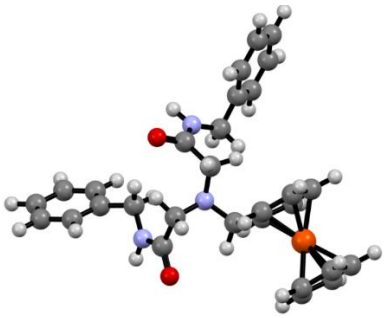

2a

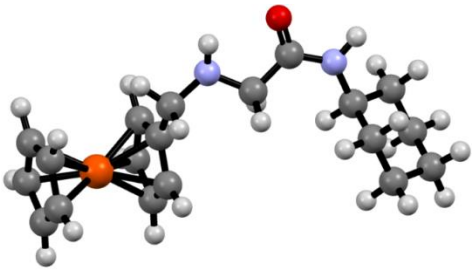

2b

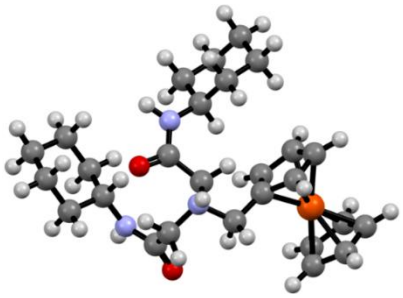

3a

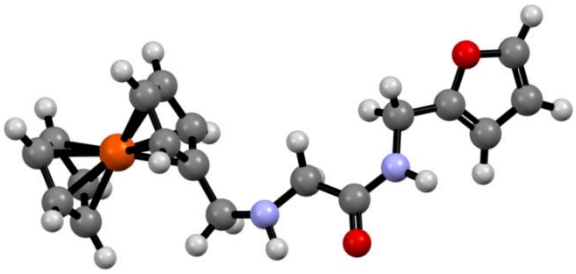

3b

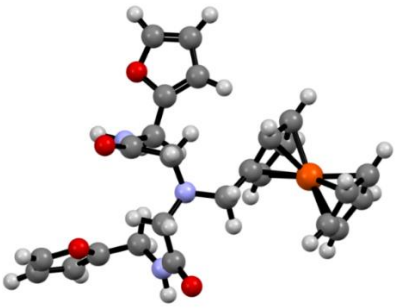

4a

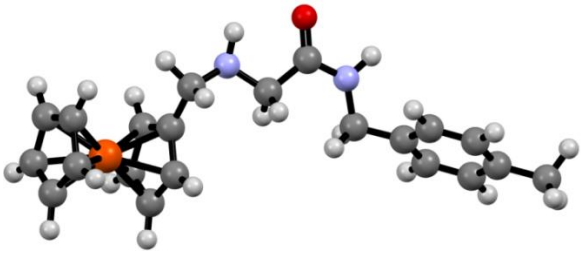

4b

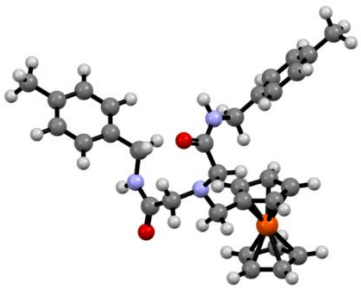

5a

5b

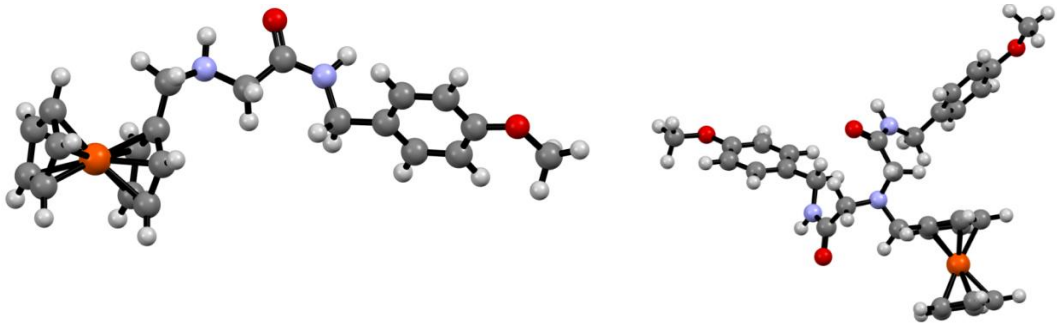

Figure 8. An optimized geometry for the minimum energy conformation of compounds 1a-5a and 1b-5b at B3LYP/LanL2DZ level.

Table 7. Summary of Computational study performed on compounds 1a-5a and 1b-5b.

Entry	Energy of Optimized Geometry (Hartree)	E_{HOMO}, E_{LUMO} (eV)	$E_{HOMO-LUMO}$ (eV)
1a	-1047.6973	-5.40990, -0.48191	4.92798
1b	-1490.3072	-5.57589, -0.64518	4.93070
2a	-1083.3777	-5.44854, -0.69389	4.75464
2b	-1561.6661	-5.66977, -0.73988	4.92988
3a	-1081.1516	-5.46650, -0.52246	4.94403
3b	-1557.2188	-5.78269, -0.85117	4.93152
4a	-1122.6896	-5.42922, -0.57743	4.85179
4b	-1640.2896	-5.63439, -0.69797	4.93642
5a	-1197.8854	-5.42432, -0.65226	4.77206
5b	-1790.6812	-5.63684, -0.70233	4.93451

[a]: Geometry optimization was performed at the DFT B3LYP/LanL2DZ level for 1a-5a and 1b-5b

2.5.5.2 Molecular electrostatic potential

The molecular electrostatic potential (MESP) of chemical species plays a decisive factor for determining the properties and potential sites associated to the reactivity in biological systems and processes. In the mapping of electrostatic potential surface of the ligands, the occurrence of negative potential is found to be concentrated over the amide oxygen whereas the positive potential is around the amide proton. The MESP surfaces of compound 1a-5a and 1b-5b are shown below in Figure 9.

1A

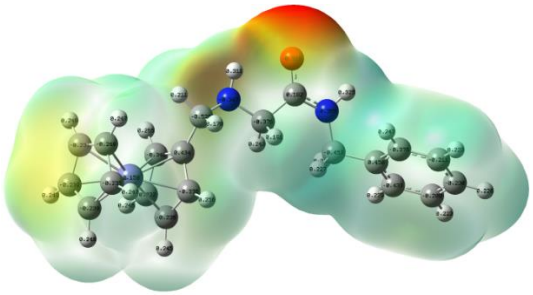

1B

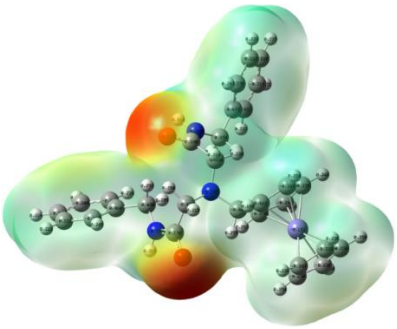

2A

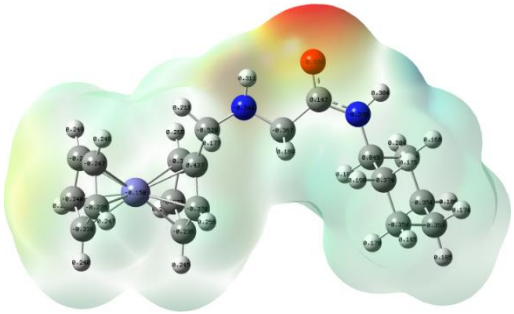

2B

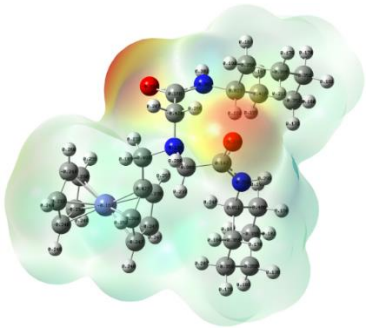

3A

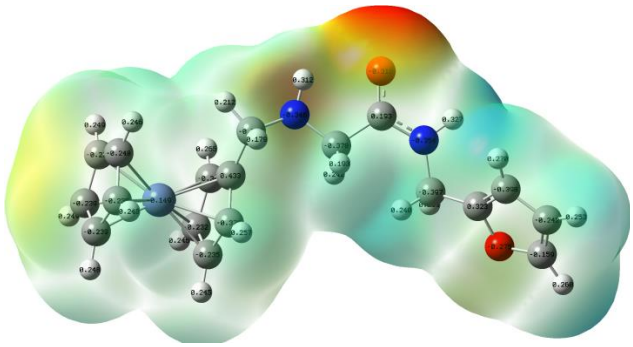

3B

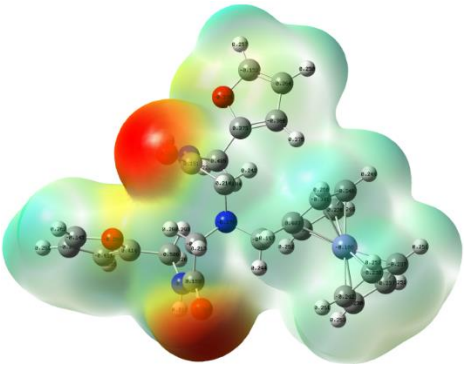

4A

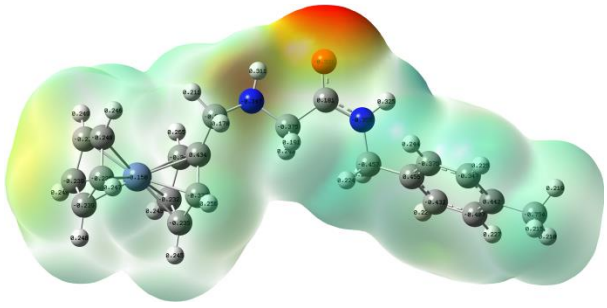

4B

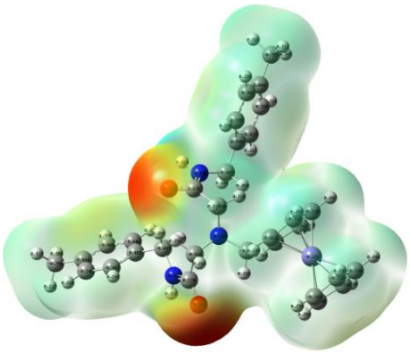

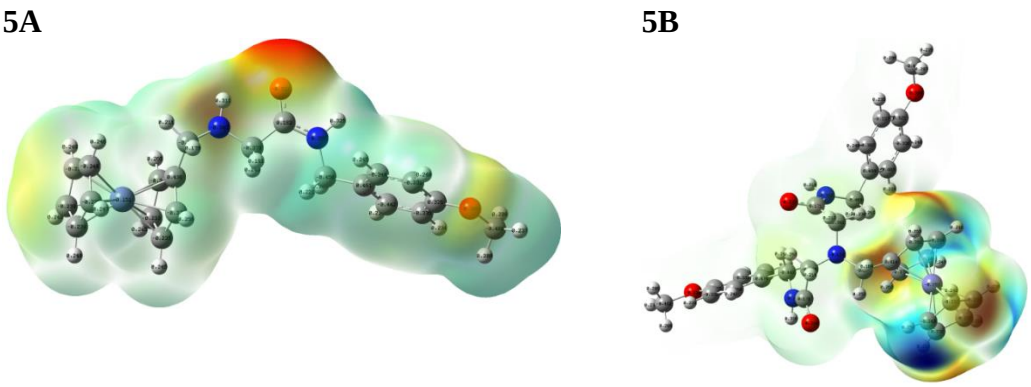

Figure 9. Representations of electron density from total SCF density (Isovalue= 0.0004; mapped with ESP)

2.5.5.3 Frontier molecular orbital analysis

The frontier molecular orbitals diagram of compound 1a-5a and 1b-5b illustrated in Figure 10. The HOMO–LUMO energy gap values for the entire investigated compound are in the range of ~ 4.7-5.0 eV which reveals the possible insulating properties of the compounds. The character of the frontier orbitals and the HOMO–LUMO energy gap greatly contribute to the photo-physical properties of the complexes and thus analysis of frontier molecular orbitals needs prime consideration for prediction of the possible reactivity of the molecule.

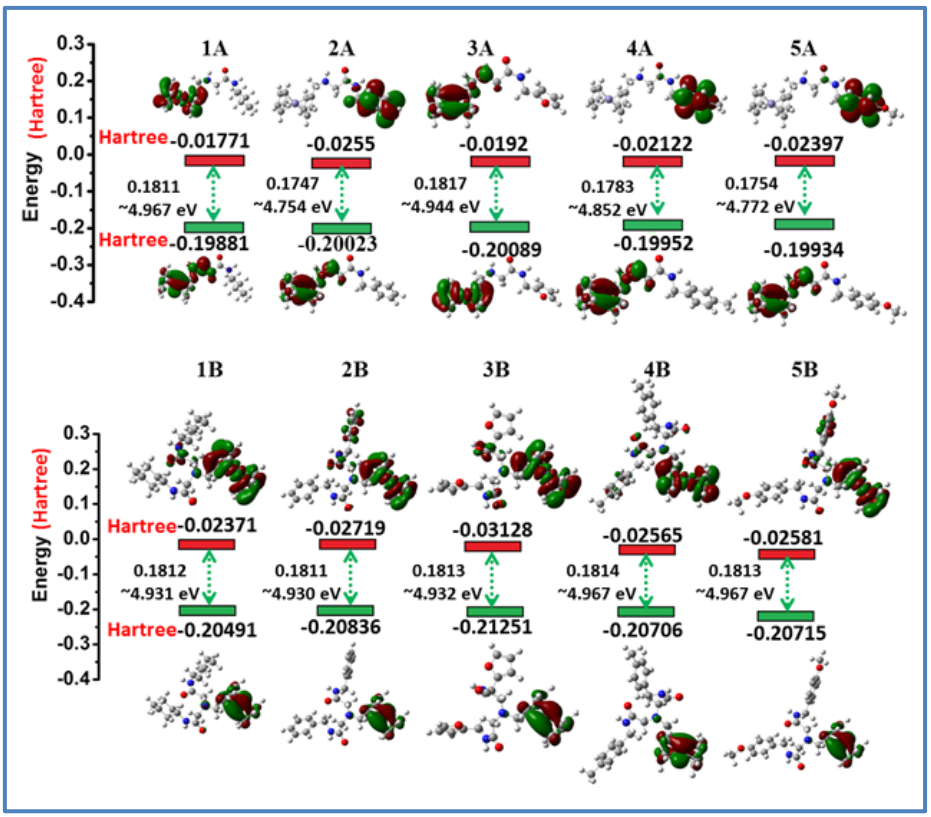

Figure 10. Comparison of the frontier molecular orbitals derived from DFT calculation at the B3LYP/LANL2DZ level for 1a-5a and 1b-1b.

2.5.6 Biological study

2.5.6.1 Inhibitory activity and structure activity relationships (SAR)

We first set out to systematically examine the influence of diverse set of simple substituents at amidic nucleus on cytotoxic activity of 1a-5a and 1b-5b. The cytotoxic potential of these amide functionalized ferrocenenylmethylamine derivatives against selected cell lines is presented in Table 8, (Figure 11). Table 8 revealed that bis-amide inhibitors 1b-5b show improved cytotoxicity profile as compared to mono-amide inhibitors 1a-5a against various cell lines due to availability of more binding sites (amidic group).

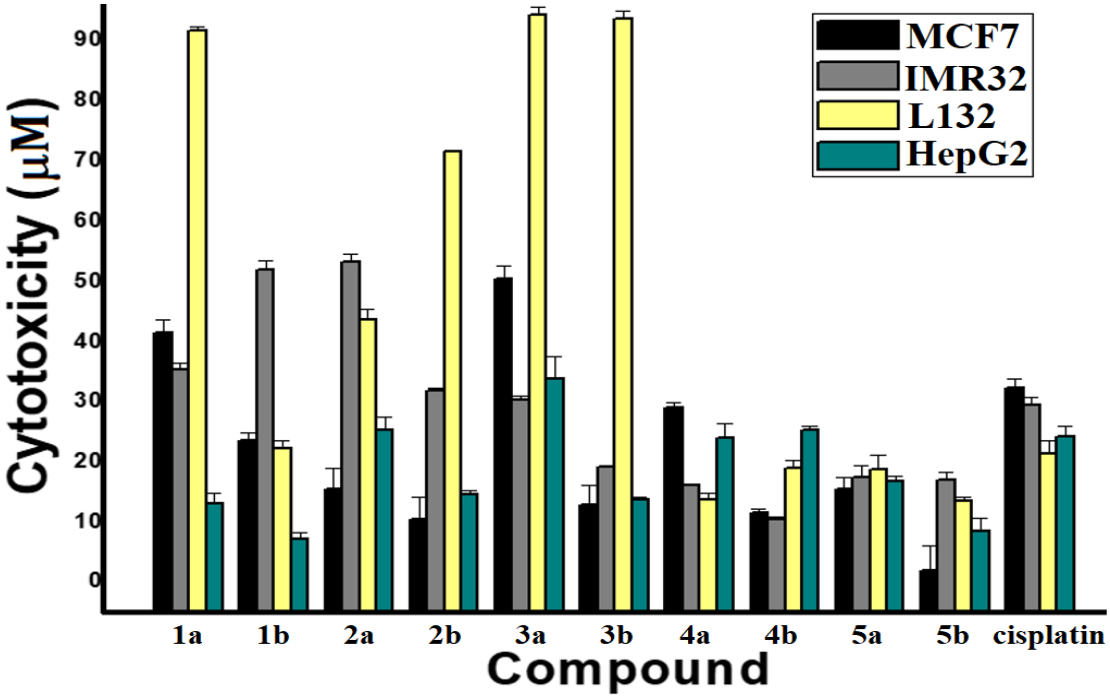

Figure 11. Cytotoxicity (μM) of amide functionalized ferrocenylmethylamine ligands on neoplasmic cell lines.

Evidently, the introduction of an optimal substituents *p*-methylbenzyl and *p*-methoxybenzyl at the amidic nitrogen of bis-amide inhibitors 4b and 5b, respectively gave a remarkable increase in cytotoxicity against several cell lines. For instance, in comparison to the reference drug cisplatin, inhibitors 5b and 4b showed ~15 fold and ~3 fold better inhibition against MCF 7, respectively. Notably, the introduction of benzyl substituent at the amidic nitrogen of bis-amide inhibitor 2b gave similar result to that of 4b against MCF 7. Inhibitors 4b and 5b showed ~3-2 fold better activity against IMR 32 than the reference. Against the hepatocellular carcinoma HepG2 cell line, inhibitor 5b showed comparable activity to that of 1b.

Table 8. *In vitro* cytotoxicity on cell line after 24 hours of exposure of 2-(ferrocenylmethylamino)-N-alkylacetamide (1a-5a), 2, 2'-(ferrocenylmethylazanediyl)bis(*N*-alkylacetamide) (1b-5b).

	Ligand	IC_{50} values (μM)			
		MCF 7	**IMR 32**	**L132**	**HepG2**
1	1a	41.45±0.22	35.45±0.11	91.80±0.07	13.19±0.17
2	1b	23.63±0.12	52.11±0.11	22.37±0.13	7.25±0.11
3	2a	15.54±0.54	53.20±0.15	43.74±0.08	25.38±0.21
4	2b	10.49±0.37	31.96±0.20	71.68±0.01	14.60±0.08
5	3a	50.42±0.43	30.35±0.07	94.30±0.14	33.84±0.37
6	3b	12.89±0.33	19.14±0.20	93.79±0.12	13.74±0.05
7	4a	29.07±0.09	16.17±0.19	13.77±0.01	24.14±0.22
8	4b	11.49±0.07	10.39±0.30	19.10±0.12	25.25±0.08
9	5a	15.60±0.19	17.55±0.19	18.74±0.24	16.83±0.09
10	5b	2.10±0.41	16.95±0.15	13.56±0.07	±0.21
11	Cisplatin	32.41±1.5	29.6±1.26	21.4±2.2	24.3±1.7

Values are represented as Mean ± SEM.

Although, inhibitors 1b, 2b and 3b have shown better potency than the reference drug, however the highest activity against HepG2 was observed for 5b and 1b which contain *p*-methoxybenzyl and benzyl substituent at amidic nitrogen. The IC_{50} values of synthesized inhibitors were found to be most effective on HepG2 amongst all the investigated cell line cells. Notably, Tyr119 was identified as a common binding site for all the inhibitors, but on substitution of amidic scaffold with *p*-methoxybenzyl switches the inhibitor binding mode of 5b to Gly121 with TNFR1, which authenticate 5b as potent anti-proliferative agent. The molecular electrostatic potential (Figure 9) of all the ligands clearly demonstrates that the presence of polar amide subunits which are indeed projected towards the outside. This provides H-bond donor-acceptor sites to facilitate the interactions with biomolecules, leading to the effective cellular membrane transportation causing increased concentration of complexes at the site of action. Moreover, the presence of bulkier *p-methoxybenzyl* substituents probably enhances the lipophilicity resulting in greater cellular accumulation, responsible for better activity.

The obtained IC_{50} values for herein studied ferrocene ligands (except some) are more effective than cisplatin on different human cancer cell line. For analysis of cytotoxicity, uptake of the molecule by the cell is an important process. Hereby, with aim to identify the lead ligands for their drug likeness, we studied the molecular properties of ligands by ADMET analysis and screened by Lipinski and Veber filters.[21] Ligands with optimum cell permeability should follow the criteria PSA <

140 Å2 and AlogP98 < 5. All of the ligands showed the best fit of the proposed model (Table 9, Figure 12-13).

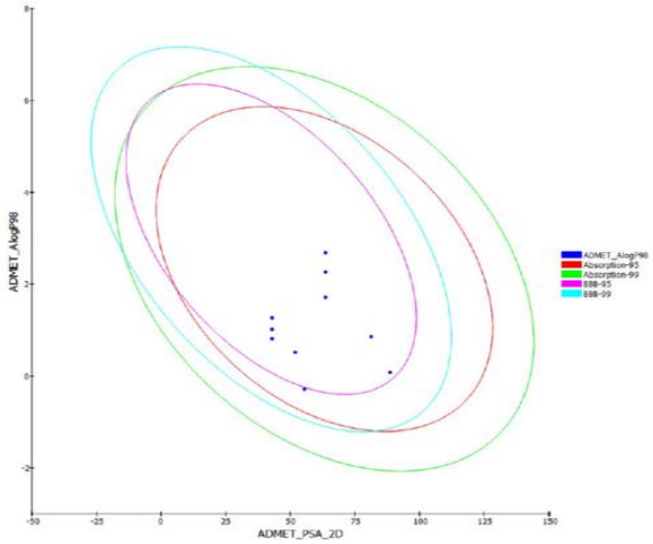

Figure 12. Discovery Studio ADMET Model.

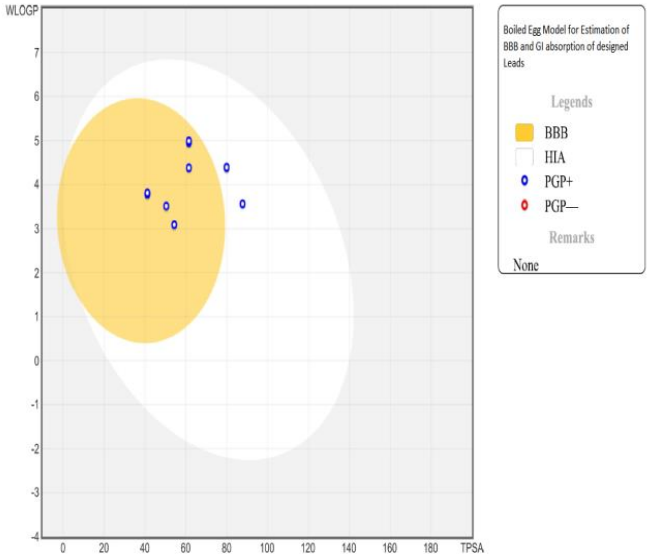

Figure13. Swiss ADME Model.

Table 9. ADMET/Pharmacokinetic Prediction of Representative Lead molecules.

$C_{20}H_{22}FeN_20$		$C_{29}H_{31}FeN_30_2$		$C_{21}H24FeN_20_2$		$C_{21}H24FeN_20_2$	
Property	Value	Property	Value	Property	Value	Property	Value
MW	362.25	MW	509.43	MW	392.28	MW	584.2

							1
HBD	2	HBD	2	HBD	2	HBD	4
HBA	2	HBA	3	HBA	3	HBA	5
Log P	-2.21	Log P	-1.3325	Log P	-1.524	Log P	-1.112
MolLogP	3.64	MolLogP	5.73	MolLogP	3.59	MolLogP	5.63
MolLogs	-3.63	MolLogs	-5.78	MolLogs	- 3.71	MolLogs	-5.33
MolLog PSA	37.32	MolLog PSA	5.47	MolLog PSA	44.86	MolLog PSA	68.55
MolVol	371.71	MolVol	523.45	MolVol	403.55	MolVol	587.14
Violations	0	Violations	0	Violations	1	Violations	1
BBB	4.88	BBB	3.97	BBB	4.57	BBB	2.21
TPSA	41.13	TPSA	61.44	TPSA	50.36	TPSA	79.90
Drug Likeness Model Score	0.05	Drug Likeness Model Score	-0.25	Drug Likeness Model Score	-0.13	Drug Likeness Model Score	-0.30

Furthermore, the quantitative structure, toxicity relationship (QSTR) was performed to validate the toxic potentials of the lead ligands. Many of the compounds in the present series, showed anticancer activity in low micro-molar concentrations which is indeed comparable with the activity of several high molecular weight organometallic compounds, recently reported in the literature elsewhere. Notably, some of the compounds showed better activity than the activity of several ferrocence-glycine/ L-alanine hybrid compounds, recently reported in the literature.[22] QSTR model clearly suggested that all the lead molecules are non-toxic and non-carcinogenic (Table 10).

Table 10. QSTR-Model of Ames Mutagen Test of Representative Lead Molecule.

Lead-Descriptors	**Similar Hit -1**		**Similar-Hit-2**		**Similar-Hit-3**	
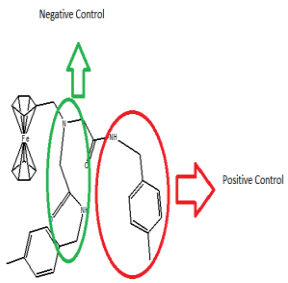 Non-Carcinogen Non-Mutagen	Oxethazine 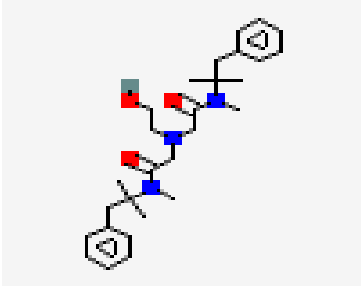		PubChem: ID 85723-20-2 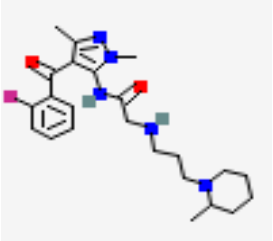		Flecainide Acetate 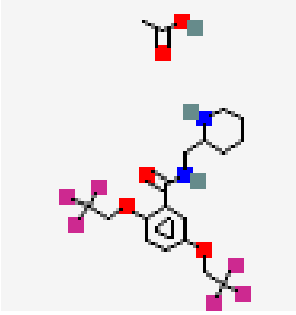	
Bayesian Score: -3.34	Type	Non-Mutagen	Type	Mutagen	Type	Non-Mutagen
Mahalanobis Distance:	Predicted	Non-Mutagen	Predicted	Mutagen	Predicted	Non-

11.4						Mutagen
Mahalanobis Distance P-Value: 0.0105	Actual	Non-Mutagen	Actual	Mutagen	Actual	Non-Mutagen
	Distance	0.627	Distance	0.666	Distance	0.668

2.5.6.2 AO/ErBr staining

The dual staining of acridine orange (AO) and ethidium bromide (EtBr) phenomenon speculates that AO penetrated normal and early apoptotic cells with intact membranes, fluorescing green. Ethidium bromide entered in damaged cells, such as late apoptotic and dead cells, emitting orange-red fluorescence via binding to DNA. The efficacy of ferrocenenylmethylamino functionalized amide inhibitor 5b to induce programmed cell death was observed prominent as a promising anti-proliferative agent in comparison to 4b and 1b (Figure 14). The apoptotic pattern observed after exposure of 4b was pre-eminent as compare to 1b. HepG2 cells were featured with apoptotic cell death after the exposure of 5b and 4b whereas the morphological pattern of 1b inhibitor suggested secondary necrosis.

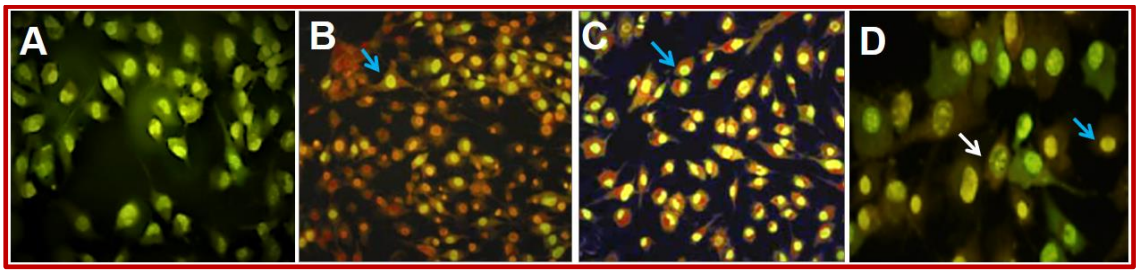

Figure 14. AO/ErBr staining on HepG2 cells. A, Untreated cell stained by AO with more viable cell density; B, 1b); C, 4b); D, 5b) Treated cell staining pattern by AO/EtBr. On treatment of 1b, 4b and 5b ligands to HepG2 cells apoptotic pattern of dual staining was observed. Cells stained green represent viable cells, whereas yellow staining represents early apoptotic cells (white arrow) and reddish or orange staining (Blue arrow) represents late apoptotic cells.

2.5.6.3 Transcript analysis

Transcript analysis revealed that the expression level of cellular inhibitors of apoptosis 1 (cIAP1) was positively associated with TNFR1 in cancer survival. Activation of TNFR1, surface receptor, and cIAP1 amplification is commonly observed outline of cancer to promote cell proliferation. As expected, data of the present study (Figure 15-17) suggested that inactivation of TNFR1 and depletion of cIAP1 expression inhibits the expression of p38MAPK and escort the cell for

apoptosis. On the treatment of amide functionalized 2º- and 3º- aminomethylferrocene ligands to selected cell lines, cIAP1 expression decreased as compared to control. Expression of p38MAPK expression was also measured fold decrease after treatment that was in support of cIAP1 expression. On downregulation of p38MAPK, rate of proliferation decreased that would be in support of the cyclin dependent kinase (CDK) expression. Lower the expression of p38MAPK alters the cancerous cell physiology and triggers an antiproliferative cascade in cells. This phenomenon was supported by the expression of CDK, p53 and tubulin. Lower the expression of cyclin dependent kinase and tubulin, augment cell cycle arrest that induces programmed cell death in cells. The tumor suppressor p53 and its expression after the exposure of amide functionalized 2º- and 3º-aminomethylferrocene ligands were observed fold elevated that was supportive phenomenon for apoptosis induction in cancerous cell. Bcl2 family protein is a key regulator of programmed cell death. The expression of Bax, pro-apoptotic inducing member of Bcl2 family, showed fold increased, whereas the expression of anti-apoptotic member, Bcl2 expression decreased after 24 hours of treatment. The activity of caspase 9 is enhanced during apoptosis, which was observed fold upregulated after treatment. The change in the expression pattern of apoptosis transcript was prominent in comparison to cisplatin treatment. Cisplatin is considered to be drug resistant on exposure. There was no clear relation between cisplatin induced apoptosis through intrinsic Bcl2 and Bax expression and modulation of the Bcl-2/Bax ratio.[23] This was in correlation n with the present result of positive control cisplatin. In comparison to all the synthesized inhibitors, 4b has shown a most promising modulatory effect on transcript expression of cancerous cell lines. The transcript expression of TNFR1 was observed fold decreased after 4b treatment. The fold decreased expression of TNFαR1 was 2 fold in HepG2, 3.7 fold in MCF 7 and 2.93 in IMR 32 cells after 24 hours treatment of 4b whereas fold upregulated transcript expression of tumor suppressor gene p53, was 2.99 fold in HepG2, 2.23 fold in IMR32 and 2.5 fold in MCF 7 cells. The pattern of low expression of anti-apoptotic cell proliferation regulatory gene and upregulation of tumor suppressor gene was followed by 5b inhibitor as second most effective apoptosis inducer.

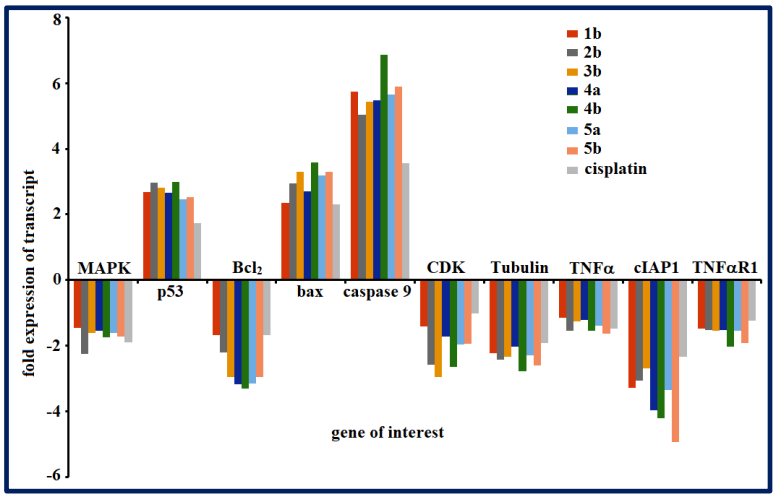

Figure 15. Modulation of transcript expression after treatment of ferrocenylmethylamine ligand derivatives to HepG2 cell line.

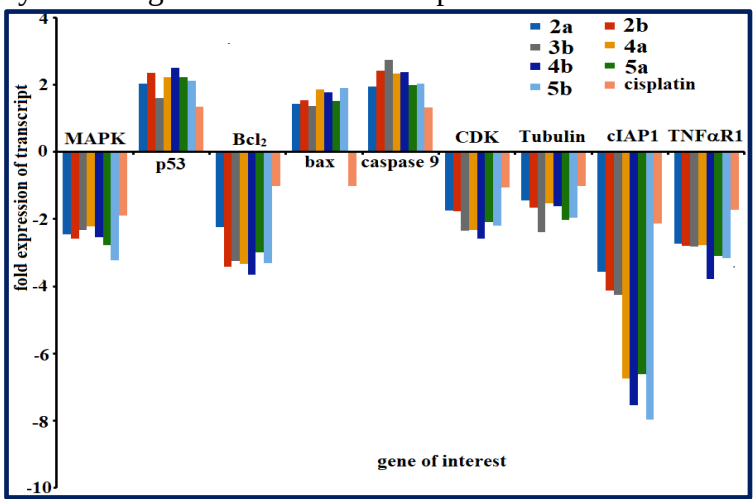

Figure 16. Modulation of transcript expression after treatment of ferrocenylmethylamine ligand derivatives to MCF 7 cells.

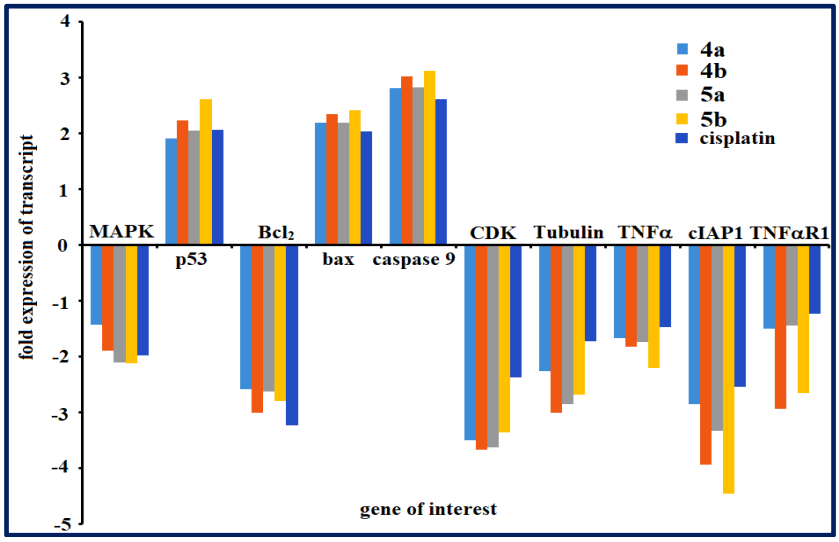

Figure 17. Modulation of transcript expression after treatment of ferrocenylmethylamine ligand derivatives to IMR 32 cells.

According to Pearsons's correlation analysis for HepG2 cells, the TNFR1 expression level was positively correlated with cIAP expression (r=0.695, P=0.01, 4b; r=0.703, P=0.002, 5b) whereas expression of Bcl2 and caspase 9 was negatively correlated (r=-0.859, P=0.001, 4b; r=-6.09, P=0.009, 5b). There was a positive correlation observed between caspase 9 and Bax expression (r= 0.804, P=0.005, 4b; r=0. 681, P=0.002).

2.5.6.4 Annexin V/ Propidium iodide assay

Annexin V/PI staining and flow cytometry were performed to investigate the cell death analysis after 24 hours of 4b and 5b ligand treatment to HepG2 cells. According to our results displayed in Table 11, there was significant apoptotic cell death after the treatment of target ligand. Apoptotic (pro and late) death was accounted for 77.3% and 70.3% after 24 hours of treatment of 4b and 5b, respectively. As shown, the cell population decreased in the live cell quadrangle (Q3) and increased in pro-apoptotic and apoptotic quadrangle (Q4 & Q2) (Figure 18). The PI positive cell was less in untreated control HepG2 cells. Results are in support of AO/EtBr staining where apoptotic cell were observed significantly. Evidently, with an increase in the expression of apoptosis initiator caspase 9, enhance the DNA fragmentation and loss the membrane integrity. Therefore, the binding efficiency of PI was increased and scored under apoptotic cell death.[24]

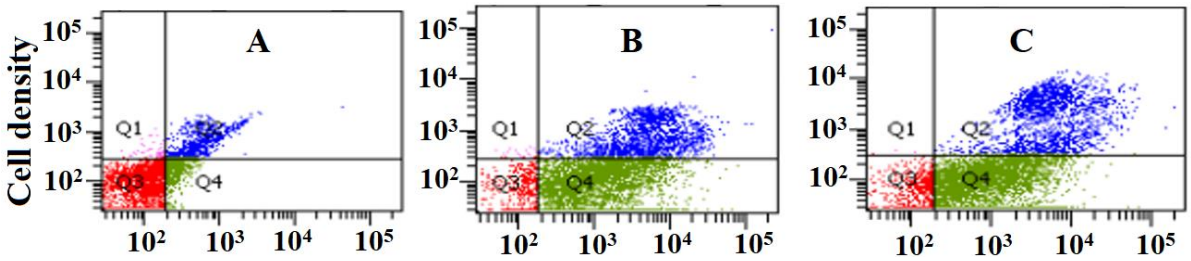

Figure 18. Fluorescent assorted cell sorting (FACS) for analysis of cell death using Annexin/PI staining after 24 hours of treatment to HepG2 cells. A) Untreated Cells, B) 4b ligand, C) 5b ligand treated HepG2 cells.

Table 11. Percent pattern of cell death of HepG2 cells after 24 hours of targeted ligand treatment

Cell Pattern	Untreated(A) %	4b(B) %	5b(C) %
Live	78.4	19.2	28.2
Pro-apoptotic	8.1	58.2	53.2
Late Apoptotic	11.3	19.1	17.1

2.5.6.5 Protein expression analysis

Protein expression was measured to verify post-transcription/translation modification on exposure of 4b and 5b inhibitors. As shown in Figure 19 (A), inhibition of the TNFR1 protein expression in HepG2 cells was observed upon treatment with 4b and 5b inhibitors. Figure 19 (B) revealed that level of TNFR1 protein decreased with increasing time of exposure of 4b and 5b. Western blot analysis shows down regulation of cIAP and phosphorylated p38MAPK on redundant of TNFR1 expression. cIAP1 deficiency sensitizes certain cell types to TNF induced programmed cell death. The phenomenon of the anticancer drug is to activate mitochondrial dependent pathway via releasing caspase 9 in apoptosis prone cancer cell.[25] TNFR1 dependent apoptosis, indicating that caspase-9 activation contributed to the activation of the caspase cascade and escort cancerous cell on death pathway via inhibiting proliferative marker like p38MAPK.[25] Moreover, on activation of caspase 9, mitochondria release IAP inhibitor and activate caspase-3. This, in turn, sensitizes neoplastic cells to apoptosis. The phenomenon of apoptosis is supported by the loss of protein expression of current study shown in Figure 19(C) and Figure 19(D), where cAIP and phosphorylated p38MAPK protein expression was downregulated.

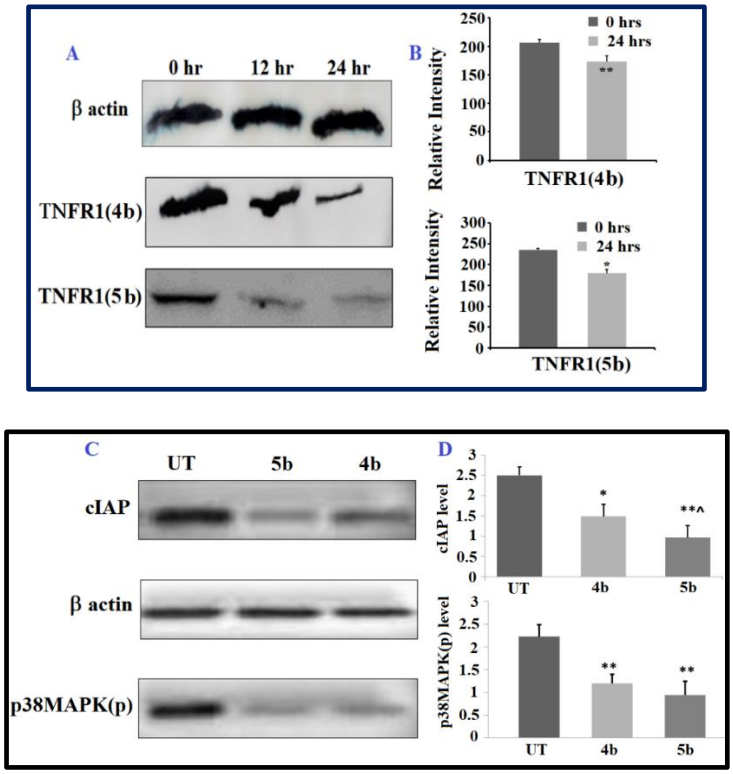

Figure 19. Western blot analysis of protein expression: A) Blot of TNFR1 protein at different time interval on exposure of 4b and 5b inhibitors; B) Relative loss of protein

level at 24 hours; C) Western blot of cIAP and phopho- p38MAPK; D) Relative depletion of protein level at 24 hours. UT- untreated cell at 0 hours. *=p $p \leq 0.005$ **=$p \leq 0.001$ in comparison with UT and ^= $p \leq 0.005$ in comparison with 4b.

2.5.6.6 Mitochondrial Membrane Potential

Several apoptotic events occur in mitochondria, of which, the most significant event is the loss of mitochondrial membrane potential ($\Delta\Psi_M$).[26] JC-1 staining emits red fluorescence on J-aggregates with a normal $\Delta\Psi_M$ of mitochondria, whereas, on a decrease in red/green fluorescence intensity ratio marks mitochondrial depolarization.[26, 27] On staining, significant shift in the fluorescence intensity ratio (towards green) in 4b and 5b treated HepG2 cells was observed (Figure 20). A fluorescence shift towards green was accounted higher on 5b treatment in comparison to 4b exposure to the cells. Evidently, amide functionalized 2º- and 3º-aminomethylferrocene inhibitors 4b and 5b hampered mitochondrial membrane potential via depolarization of the membrane. Loss of mitochondrial depolarization in HepG2 cells, suggesting that 4b and 5b alters mitochondrial respiration and insult the cells through ROS production. Our study corroborates previous notions that strengthening the relation of loss of mitochondrial membrane potential and apoptotic metabolic profile of cell can be exploited as prodrug chemotherapeutic property of ligand.[28] Loss of membrane potential was in support of gene expression pattern of caspase 9, Bcl2 and Bax. Over expression of Bax and down regulation of Bcl2 were measured after 4b and 5b treatment which is an applicable molecular event to hamper cell survival through membrane potential shift of mitochondria.

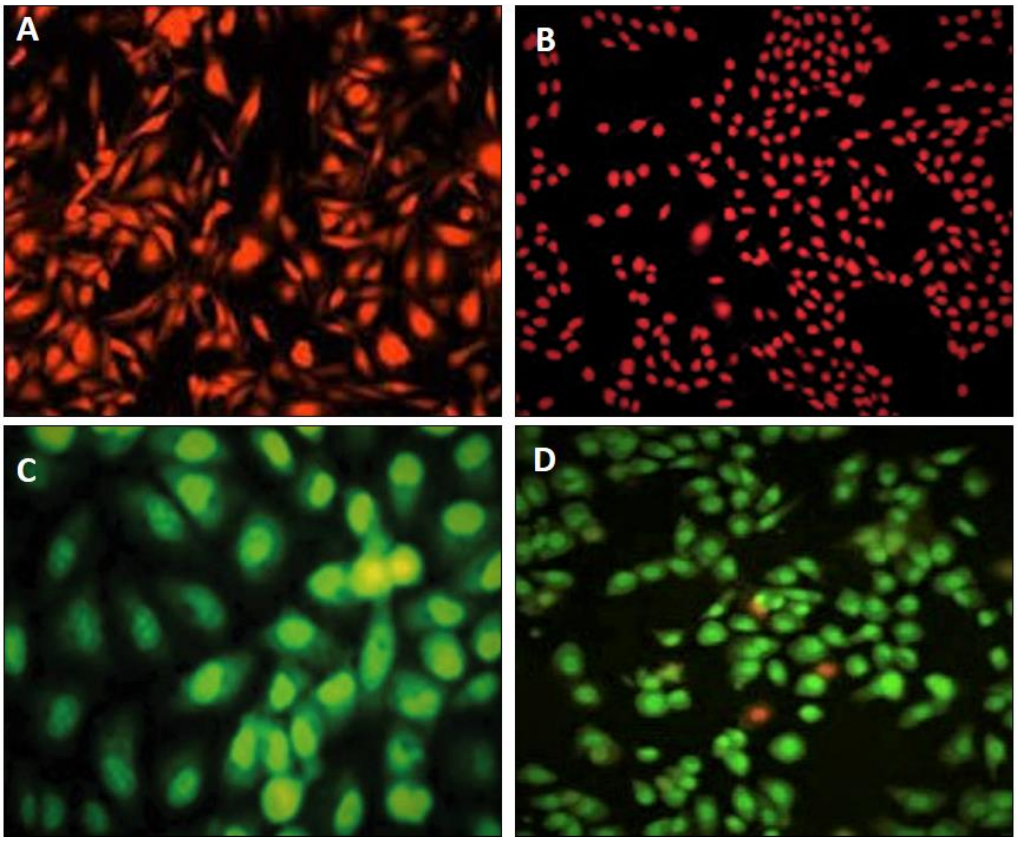

Figure 20. JC 1 staining of HepG2 cells to observe mitochondrial membrane potential ($\Delta\Psi_M$) A. J aggregate at 0 hours B. J aggregate at 24 hours C. J monomers at 24 hours after 5b exposure D. J monomers at 24 hours after 4b exposure.

2.5.7 Protein- ligand molecular docking

The manuscript characterizes the antineoplastic properties of amide functionalized 2º- and 3º- aminomethylferrocene ligands 1a-5a, 1b-5b to propose them as prodrug with potential to alter the inflammatory pathway. Molecular docking for protein-ligand studies have been performed to determine the binding mode of synthesized inhibitors 1a-5a, 1b-5b with the most probable sites of TNFα receptor. Dock scores for each ligand with different poses have been represented in Table 4. Based on dock score, it is clear that complexes 4b selectively bind to TNFR1 at the Tyr149 site and to 5b at the Gly121 sites more effectively than the other ligands. Binding interaction of 4b and 5b ligands with the TNFR1 protein is shown in Figure 21 while the interaction of other ligands is illustrated. (Figure 22-29).

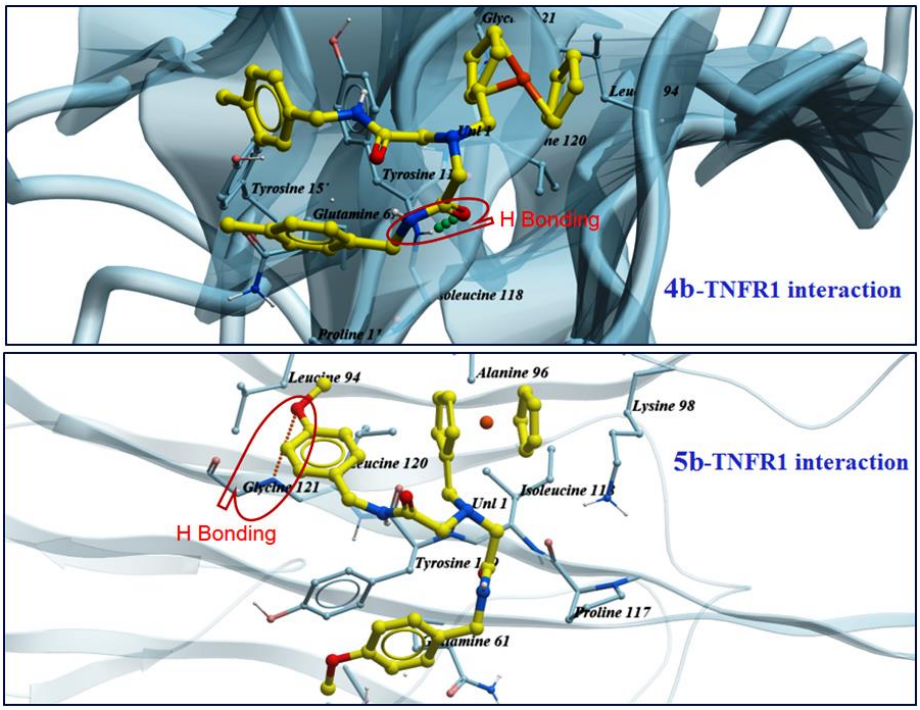

Figure 21. Binding of inhibitors 4b and 5b with TNFα receptor.

The analysis of molecular docking suggests that 4b and 5b might work as antagonist of TNFα, and bind to TNFR1 which change the configuration and inhibits binding of cIAP1 that alters the survival signalling of TNFR1 and induce cell death. Sacchi *et al.* have shown that derivatives of TNFα target effect on angiogenesis as well as shown reduced toxicity, as an antitumor agent in comparison to cisplatin, doxorubicin, paclitaxel and melphalan on some cancer like lymphoma, breast cancer.[29] Our dock results demonstrate that ligands 4b and 5b might be standardized as an effective prodrug for cancer therapeutics.

Table 12. TNF tyrosine residue and interaction of ligands with TNFα receptor.

PDB Code	Ligand	Ligand Interaction		Binding Energy (Kcal/mol)
		Hydrogen Bonding	Hydrophobic Interaction	
1tnf	1a	Tyrosine 119	Pro-117, Leu-120 & Leu-94	-5.33
1tnf	1b	Tyrosine 119	Pro-117	-5.97
1tnf	2a	Tyrosine 119	ILE-118, Ala-96, Leu-120 & Leu-94	-5.61
1tnf	2b	Tyrosine 119	Pro-117, & Leu-94	-6.33
1tnf	3a	Tyrosine 119	ILE-118, Ala-96, Leu-120 & Leu-94	-4.95
1tnf	3b	Tyrosine 119	ILE-118, Ala-96, Leu-	-5.89

			120, Leu-94 & GLy-121	
1tnf	4a	Tyrosine 119	ILE-118, Ala-96, Leu-120, Leu-94	-5.40
1tnf	4b	Tyrosine 119	Leu-120 & Leu-94 & Pro-117	-6.55
1tnf	5a	Tyrosine 119	Leu-120 & ILeu-118 & Pro-117	-5.06
1tnf	5b	Glycine 121	Tyrosine-119, LYS-98 ILE-118, Ala-96, Leu-120	-6.34

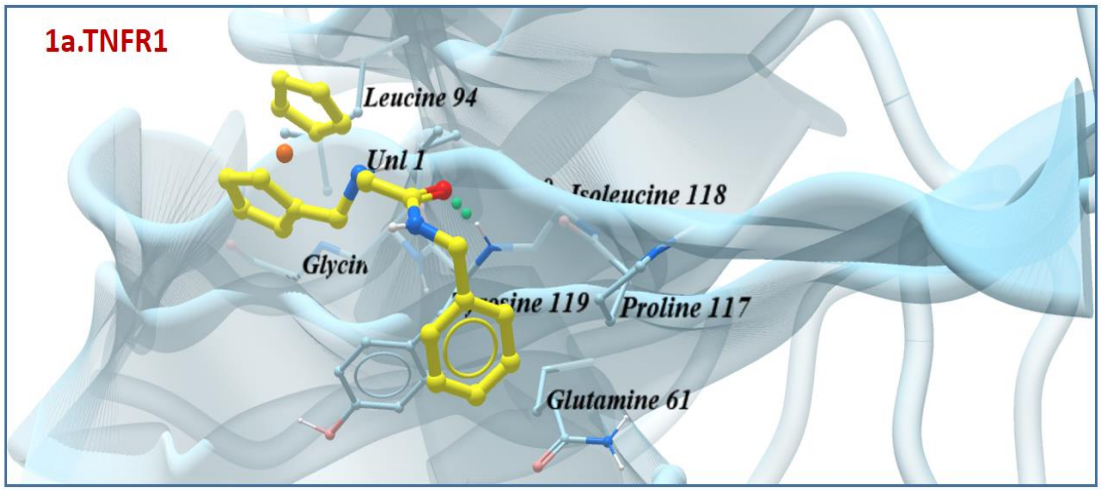

Figure 22. Binding of inhibitors 1a with TNFα receptor.

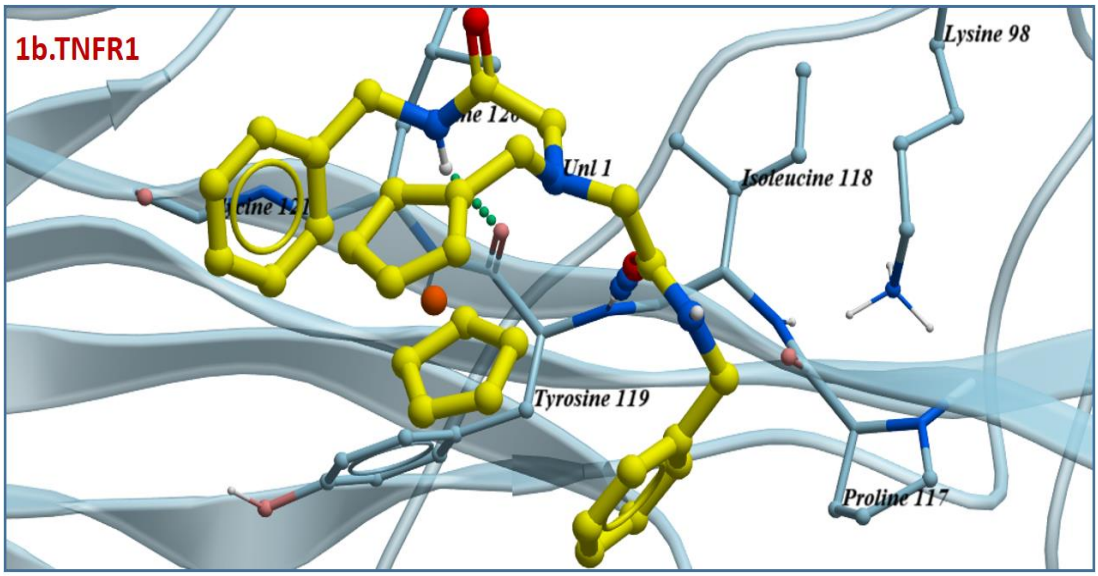

Figure 23. Binding of inhibitors 1b with TNFα receptor.

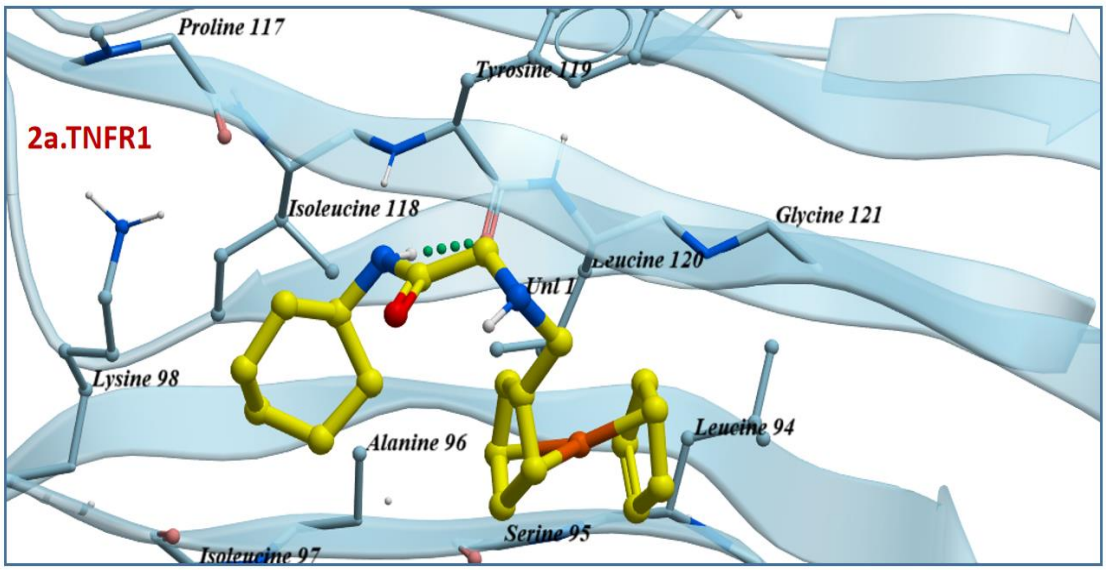

Figure 24. Binding of inhibitors 2a with TNFα receptor.

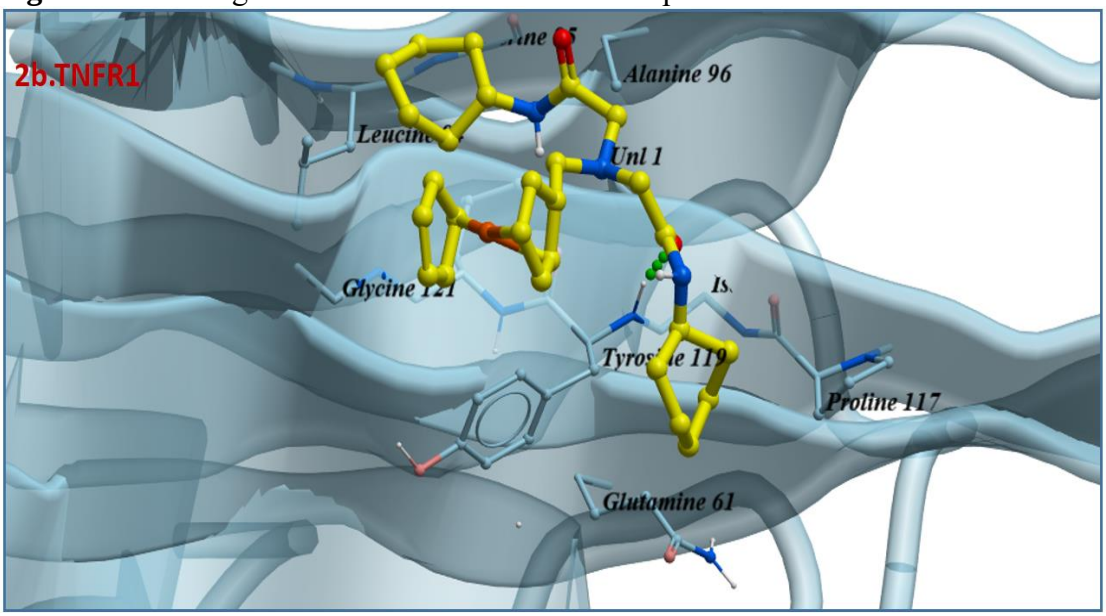

Figure 25. Binding of inhibitors 2b with TNFα receptor.

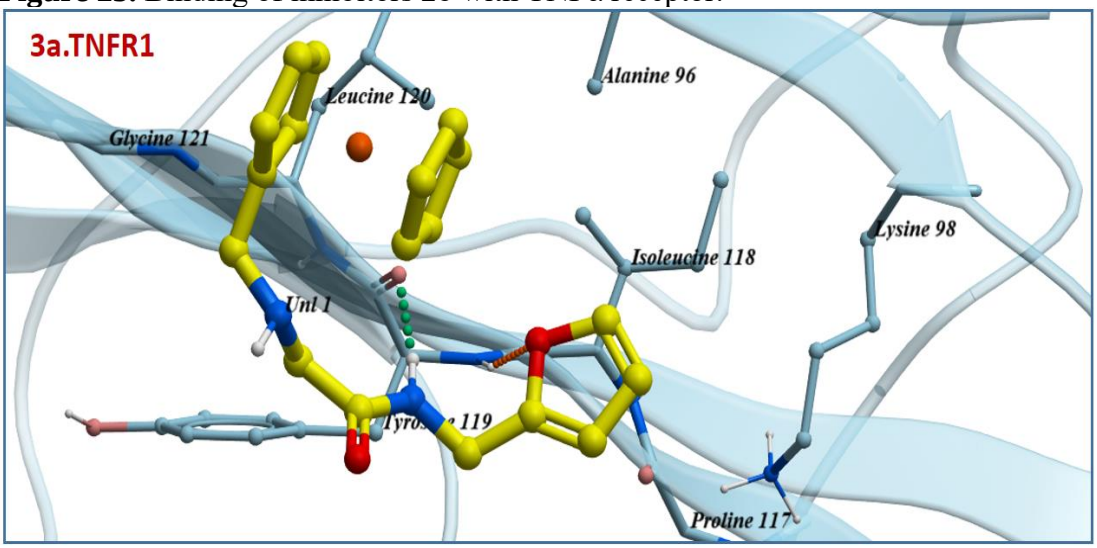

Figure 26. Binding of inhibitors 3a with TNFα receptor.

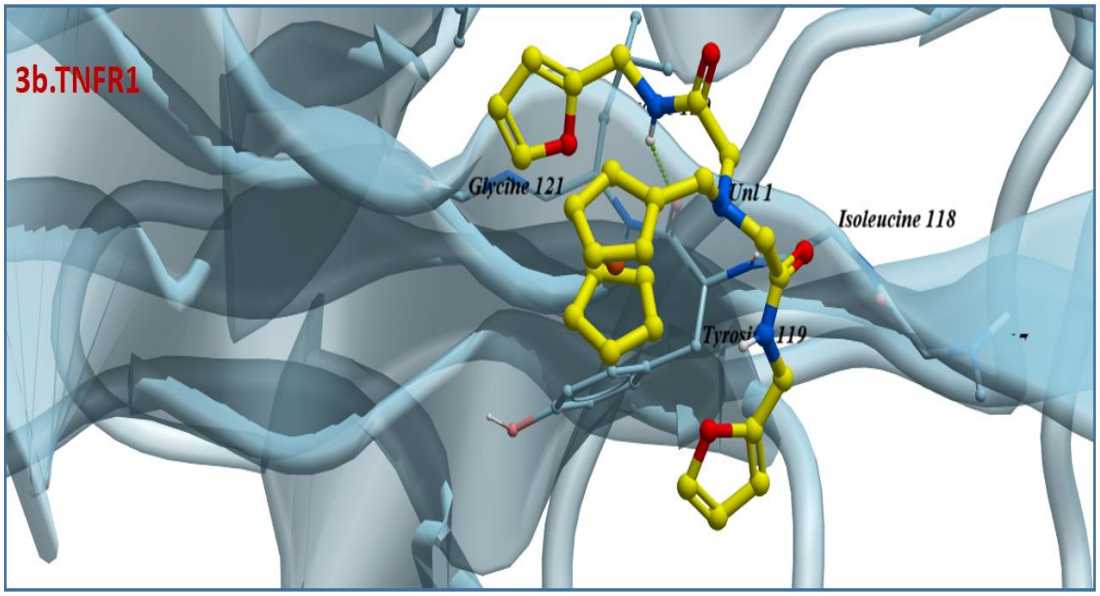

Figure 27. Binding of inhibitors 3b with TNFα receptor.

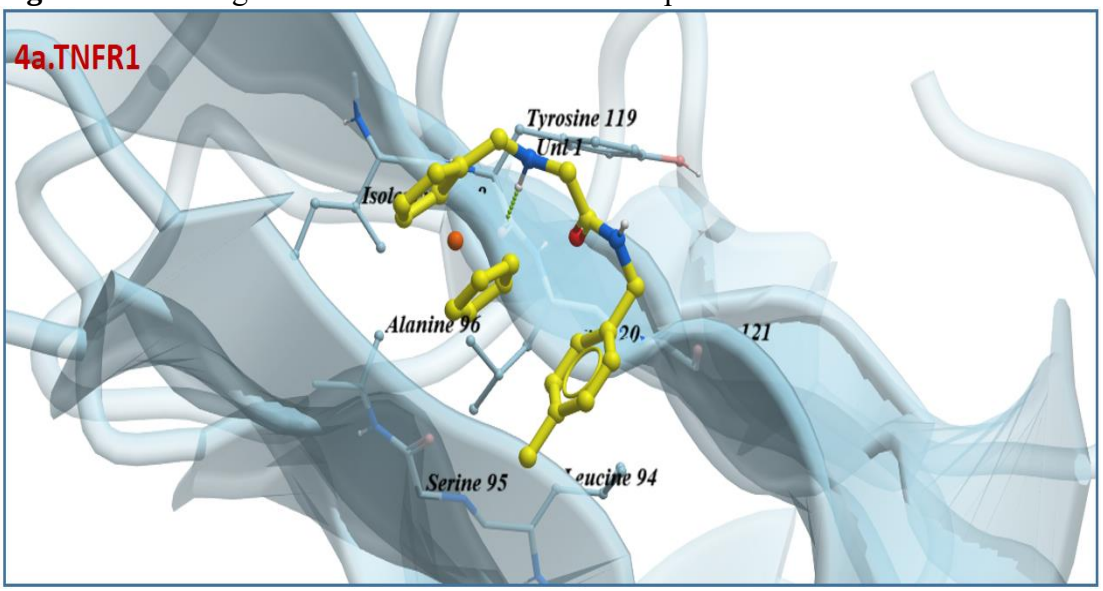

Figure 28. Binding of inhibitors 4a with TNFα receptor.

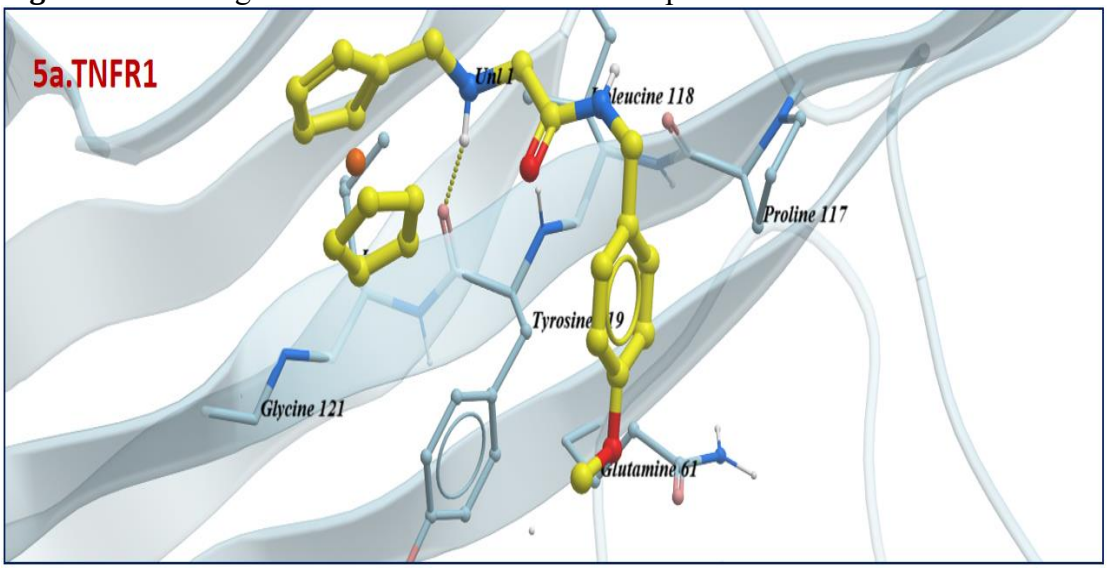

Figure 29. Binding of inhibitors 5a with TNFα receptor.

2.6 Conclusions

This study allows us to conclude that may of the newly synthesized ferrocenylmethyamine derivatives showed potent inhibition of cell growth in low μM concentrations against various carcinoma cell lines of human origin. The IC_{50} values of some of these low molecular weight compounds are found to be comparable with a number of recently reported high molecular weight organometallic compounds, however, they showed better activity than the ferrocence-glycine/ L-alanine hybrids against MCF-7 cells.[18] Highest dock score of 5b-TNFR1 suggested that the ligand 5b has a modulatory effect on TNFα receptor mediated signaling pathway which is indeed one of the known pathways involved in cancer progression and metastasis. Evidently, the loss in the expression from cancer cells induces TNFα dependent apoptosis. The reduced phosphorylation of p38MAPK hampers cell proliferation via downregulating CDK and up regulating p53. This phenomenon enhances the apoptosis in selected cancer cells of human origin. Moreover, loss of cIAP, activates caspase cascade and also alters mitochondrial membrane potential. The synergistic effect of amido, amino and ferrocenyl groups present in the molecular framework evidently enhanced the potentials of synthesized ligands as TNFR1 inhibitors and projects them as a persuasive antitumor agent. The future aspect is to functionalize amino handles of amide functionalized 2º- ferrocenylmethylamine (1a-5a) into diverse bioactive ligands.

2.7 Reference

[1] H. Z. Zhang, S. Kasibhatla, J. Kuemmerle, W. Kemnitzer, K. Ollis-Mason, L. Qiu, C. Crogan-Grundy, B. Tseng, J. Drewe, S.X. Cai, *J. Med. Chem*., **2005**, 48, 5215.

[2] A. Hunold, H. G. Schmalz, L. Kater, B. Bonitzki, P. Jesse, A. Prokop, *J. Cancer Res. Clin. Oncol*., **2010**, 137, 639.

[3] M. Patra, G. Gasser, The medicinal chemistry of ferrocene and its derivatives, *Nat. Rev. Chem*., **2017**, 1, 66.

[4] R. Wang, H. Chen, W. Yan, M. Zheng, T. Zhang, Y. Zhang, Eur. *J. Med. Chem*., **2020**, 190, 112109.

[5] H. Helen, M. Paul, J. Elmar,; Veldwijk, Marlon, European Patent, No. EP 2 497 775 A1, **2012**.

[6] C. G. Hartinger, P. J. Dyson, *Chem. Soc. Rev*., **2009**, 38, 391.

[7] S. K. Verma, V. K. Singh, *J. Organomet. Chem*., **2015**, 791, 214.

[8] G. Jaouen, A. Vessieres, S. Top, *Chem. Soc. Rev*., **2015**, 44, 8802.

[9] Y. Zhang, K. T. Zhao, S. G. Fox, J. Kim, D. R. Kirsch, R. J. Ferrante, R. I. Morimoto, R. B. Silverman, *J. Med. Chem*., **2015**, 58, 5942.

[10] V. K. Singh, R. Kadu, H. Roy, Eur. *J. Med. Chem*. **2014**, 74, 552e561.

[11] S. Luo, P. Li, S. Li, Z. Du, X. Hu, Y. Fu, Z. Zhang, *Pharmaceutics*, **2017**, 14, 1771.

[12] S. N. Rao, D. C. Mohan, S. Adimurthy, *RSC Adv*., **2015**, 5, 95313.

[13] X. Peng, Z. Sun, P. Kuang, L. Li, *J. Chen, J. Chen, Org. Lett*., **2020**, 22, 5789.

[14] R. Kadu, H. Roy, V. K. Singh, *Appl Organometal. Chem*., **2015**, 29, 746.

[15] O'Boyle, N. M.; Banck, M.; James, C. A.; Morley, C.; Vandermeersch, T.; Hutchison. G. R. "Open Babel: An open chemical toolbox. *J. Cheminf*., **2011**, 3, 33.

[16] Huey, R.; Morris, G. M.; Olson, A. J. Goodsell, D. S. *J. Computational Chem.*, **2007**, 28, 1145.

[17] (a) Dassault Systèmes BIOVIA, Discovery Studio, San Diego: Dassault Systèmes, **2020**; (b) W. J. Egan, K. M. Merz, B. J. Jr, *J. Med Chem*., **2000**, 43, 3867; (c) M. Gupta, H. J. Lee, C. J. Barden, D. F. Weaver, *J. Med. Chem*., **2019**, 62, 9824; (d) A. Daina, O. Michielin, V. Zoete, *J. Chem. Inf. Model.*, **2014**, 54, 3284; (e) A. Daina, V. Zoete, *ChemMedChem*, **2016**, 11, 1117.

[18] R. Kadu, H. Roy, V. K. Singh, *Appl Organometal. Chem.*, **2015**, 29, 746.

[19] E. Assadian, H. Dezhampanah, E. Seydi, J. Pourahmad, *J. Biochem. Mol. Toxicol*. **2019**, 33, e22303.

[20] S. Bittner, C. Meenakshi, G. Temtsin, *Tetrahedron*, **2001**, 57, 7423-7429. A. Daina, V. Zoete, *ChemMedChem*, **2016**, 11, 1117.

[21] a) R. Wang, H. Chen, W. Yan, M. Zheng, T. Zhang, Y. Zhang, *Eur. J. Med. Chem.*, **2020**, 190, 112109; b) M. Odachowski, C. Marschner, B. Blom, *Eur. J. Med. Chem*. **2020**, 204, 112613.

[22] a) A. Mandic, v. Viktorsson, M. Varsanyi, J. Hansson, S. Linder, M. C. Shoshan, *Nature Genetics*. **2001**, 27, 86; b) H. Burger, K. Nooter, A. Boersma, C. Kortland, G. Stoter, *Br. J. Cancer*., **1998**, 77, 1562.

[23] S. Pietkiewicz, J. H. Schmidt, N. I**.** Lavrik, *J. Immunol. Methods*, **2015**, 42, 399.

[24] M. V. Blagosklonny, *Oncogene*, **2004**, 23, 2967.

[25] M. A. McDonnell, D. Wang, S. M. Khan, H. M. G. Vander, A. Kelekar, *Cell Death Differ.*, **2003**, 10, 1005.

[26] F. Sivandzade, A. Bhalerao, L. Cucullo, *Bio Protoc.*, **2019**, 9, e3128.

[27] L. D. Zorova, V. A. Popkov, E. Y. Plotnikov, D. N. Silachev, I. B. Pevzner, S. S. Jankauskas, V. A. Babenko, S. D. Zorov, A. V. Balakireva, M. Juhaszova, S. J. Sollott, D. B. Zorov, *Anal. Biochem.*, **2018**, 552, 50.

[28] R. Jitschin, A. D. Hofmann, H. Bruns, A. Giebl, J. Bricks, J. Berger, *Blood.*, **2014**, 123, 2663.

[29] A. Sacchi, A. Gasparri, C. Gallo-Stampino, S. Toma, F. Curnis, A. Corti, *Clin Cancer Res.*, **2006**, 12, 175.

2.8 Annexures

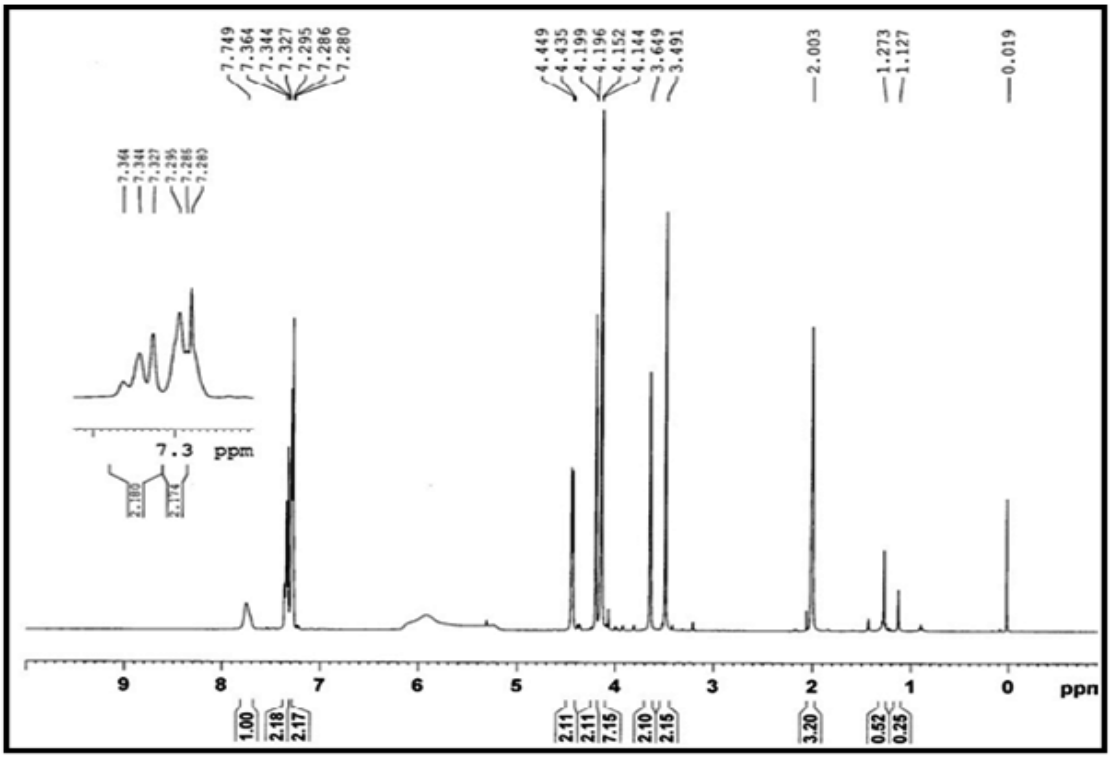

Annxure 1. ^{1}H NMR spectrum of 1a.

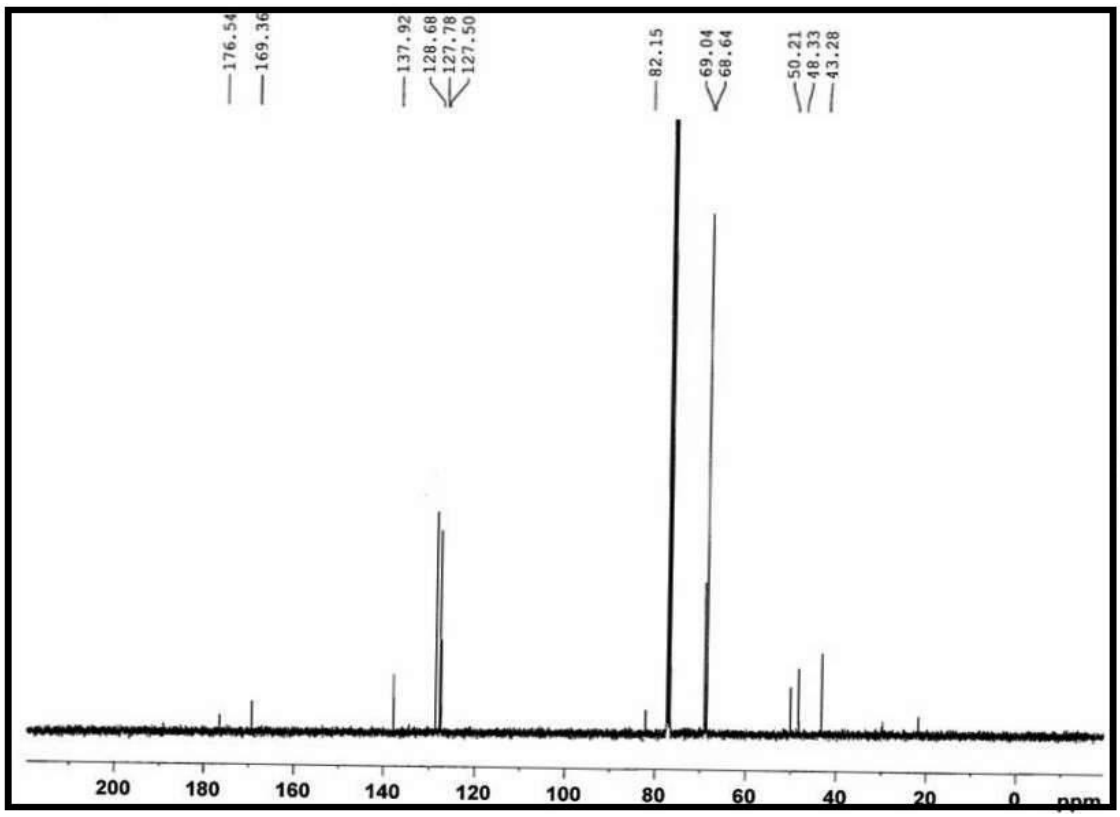

Annxure 2. ^{13}C NMR spectrum of 1a.

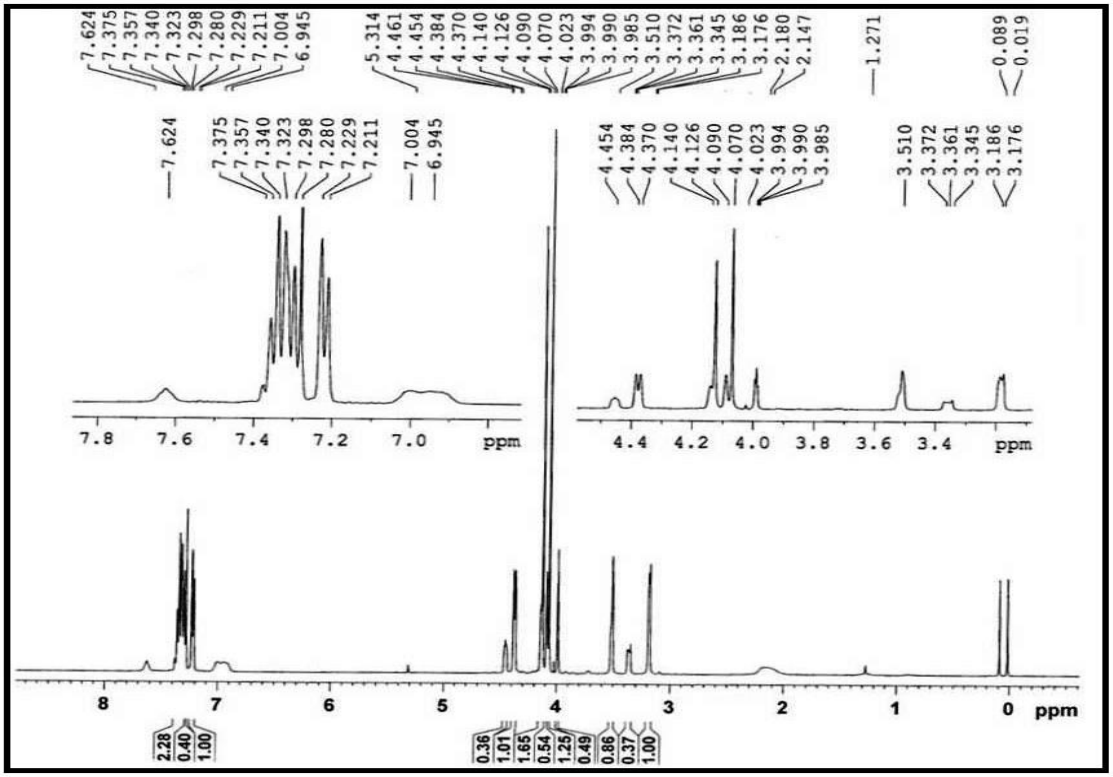

Annxure 3. ^{1}H NMR spectrum of 1b.

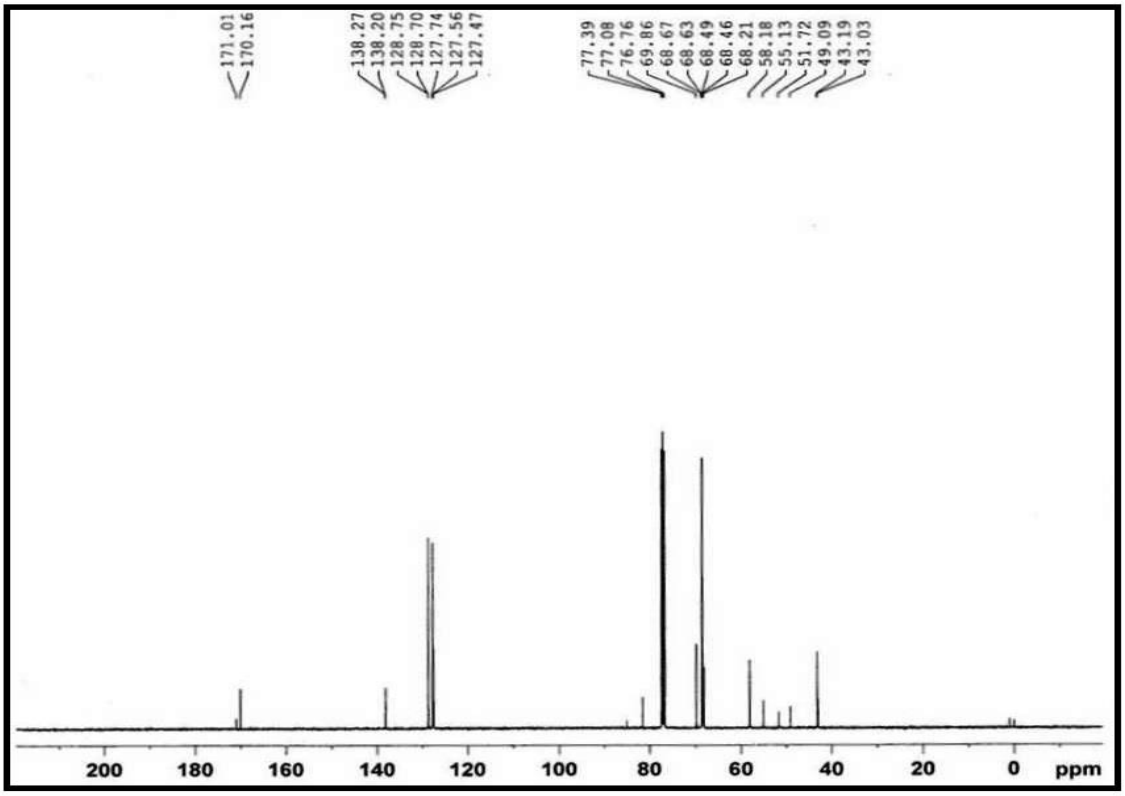

Annxure 4. ^{13}C NMR spectrum of 1b.

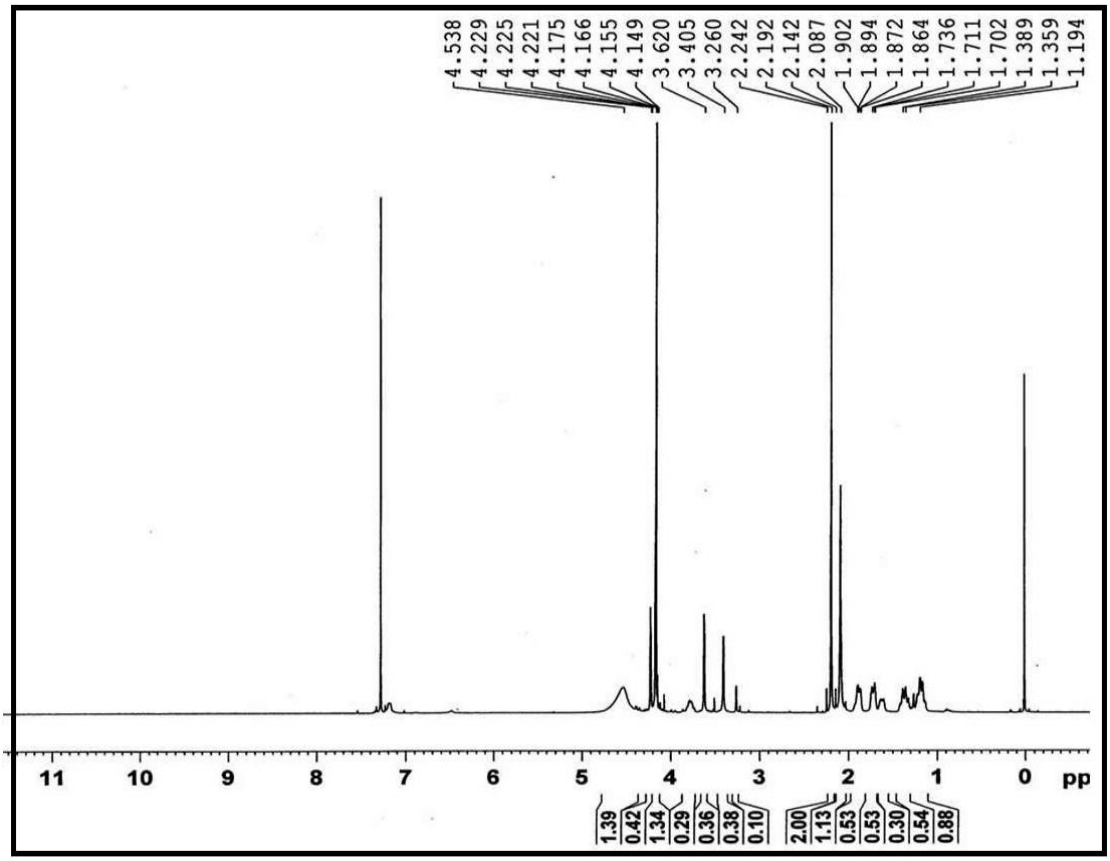

Annexure 5. ^{1}H NMR spectrum of 2a.

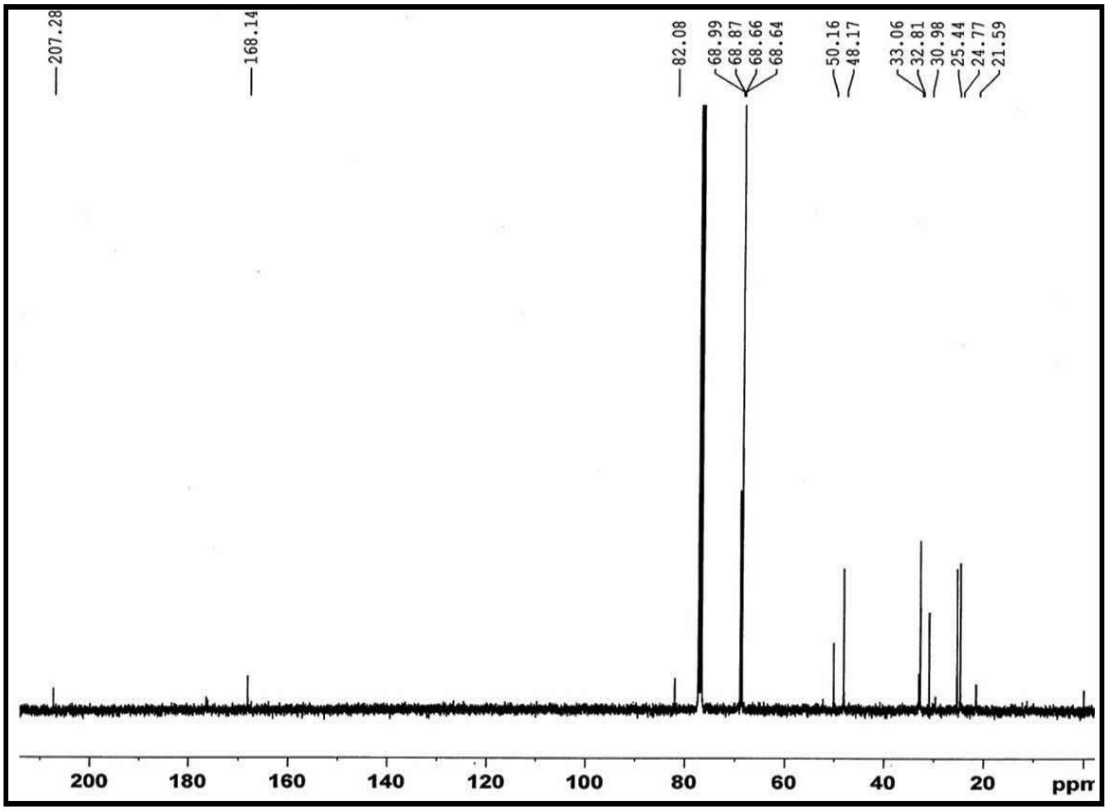

Annexure 6. ^{13}C NMR spectrum of 2a.

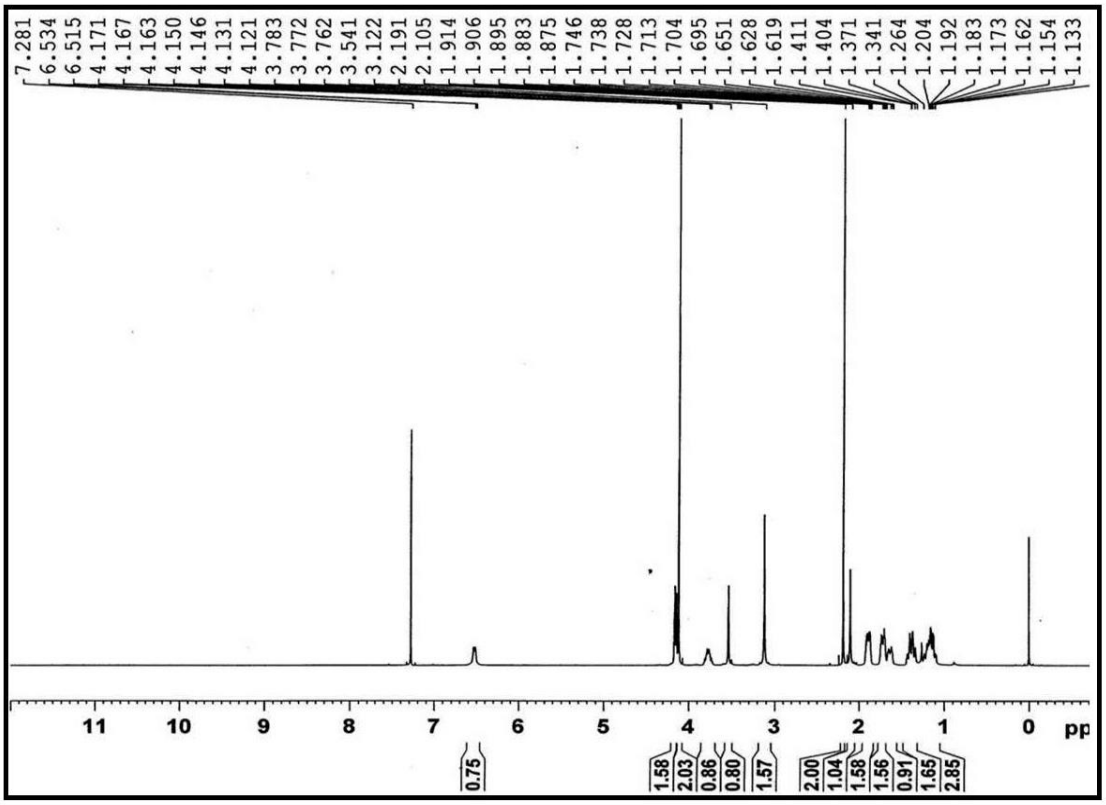

Annexure 7. ^{1}H NMR spectrum of 2b.

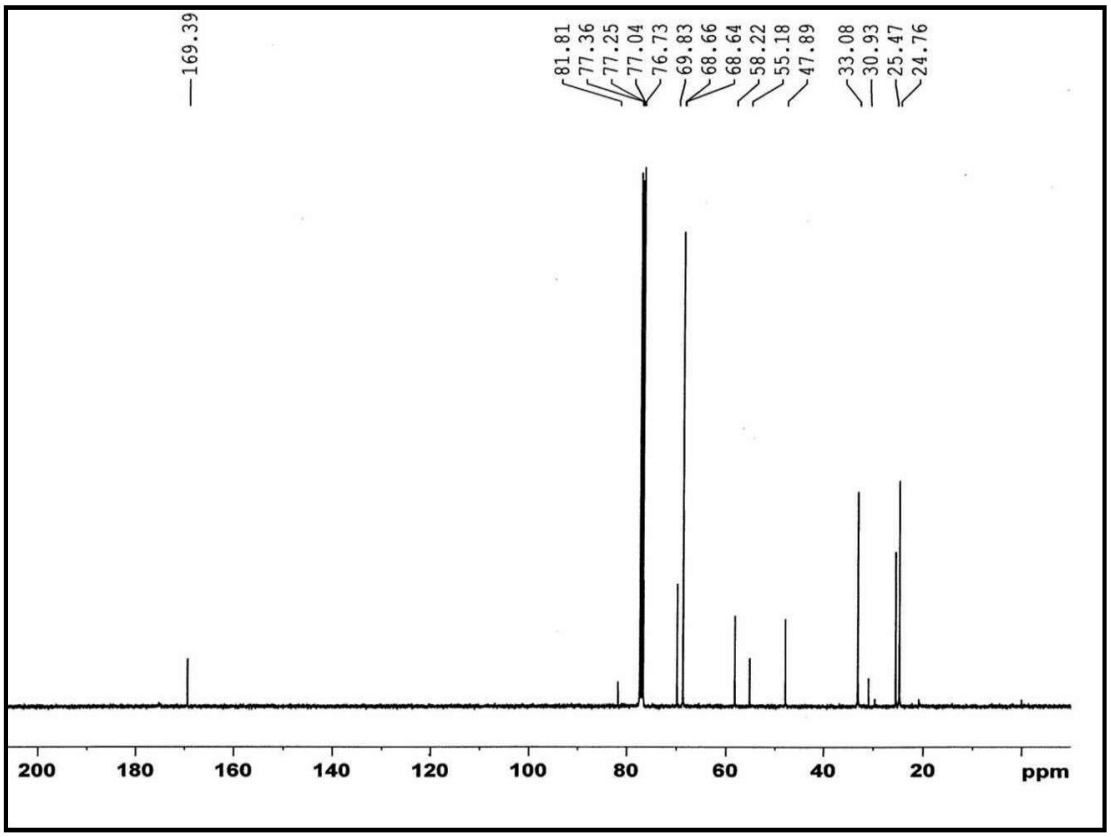

Annexure 8. ^{13}C NMR spectrum of 2b.

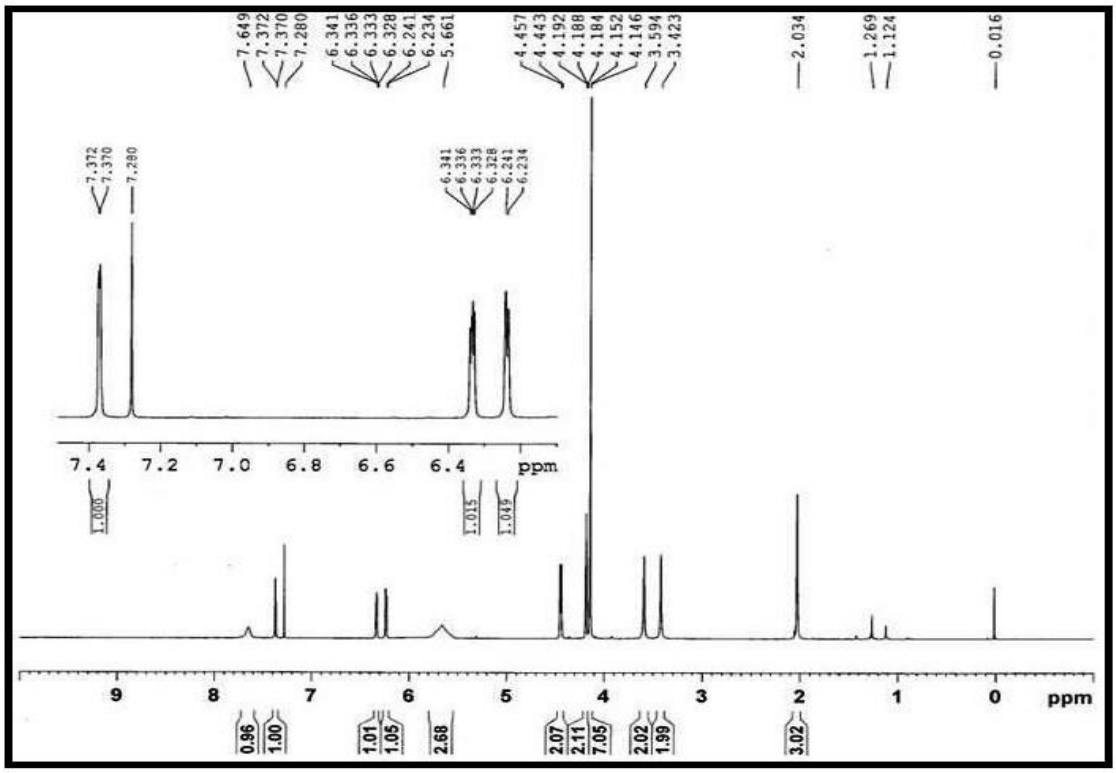

Annexure 9. ^{1}H NMR Spectrum of 3a.

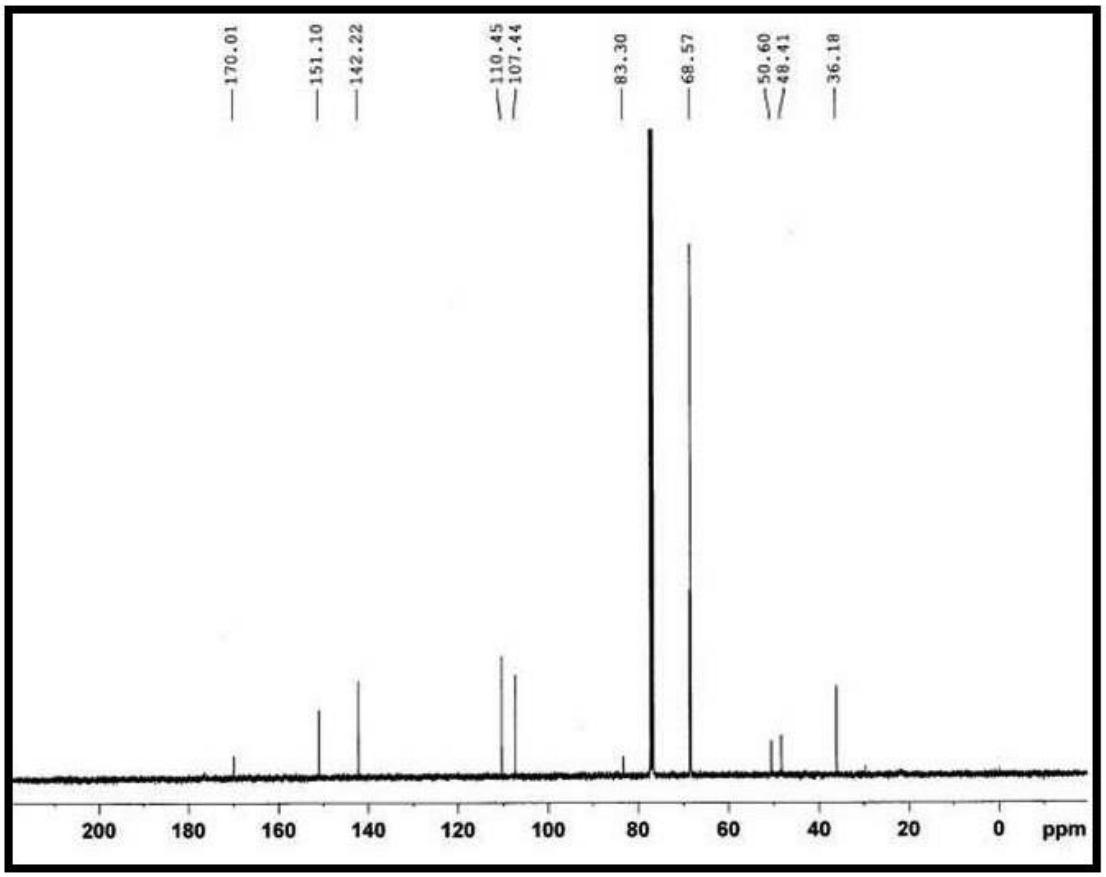

Annexure 10. ^{13}C NMR spectrum of 3a.

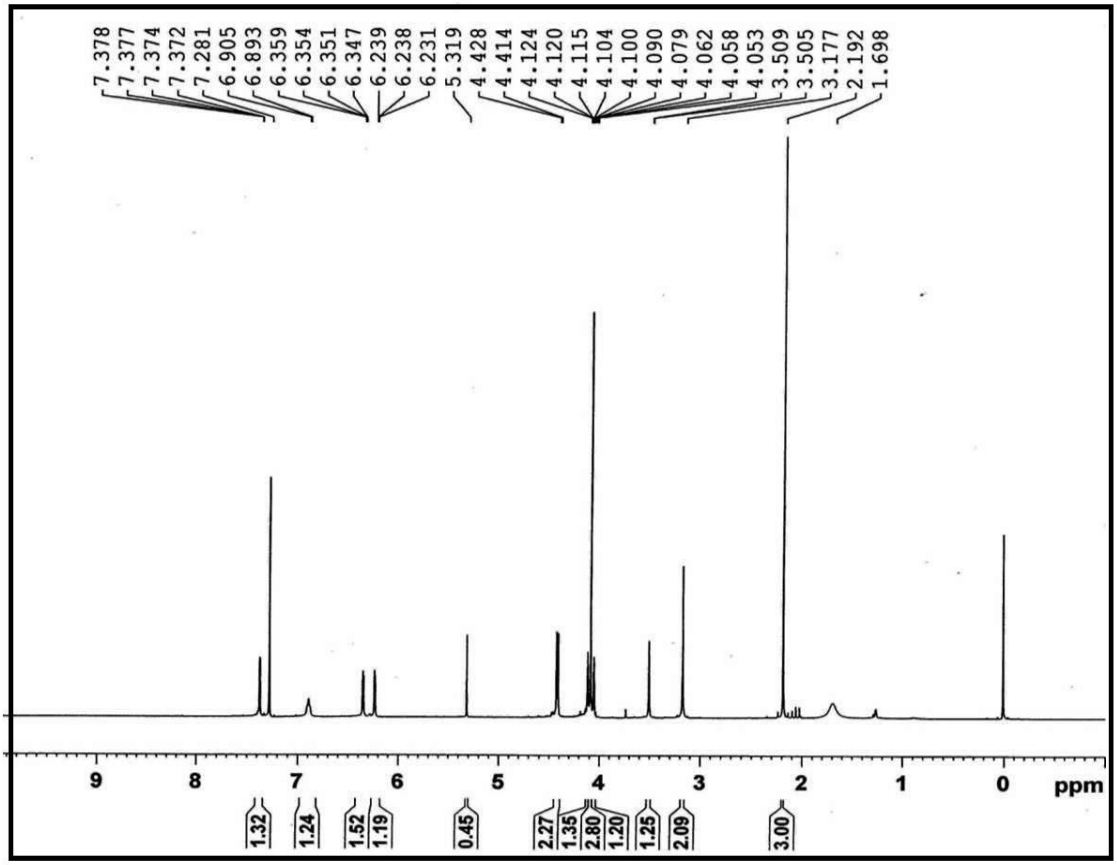

Annexure 11. ^{1}H NMR spectrum of 3b.

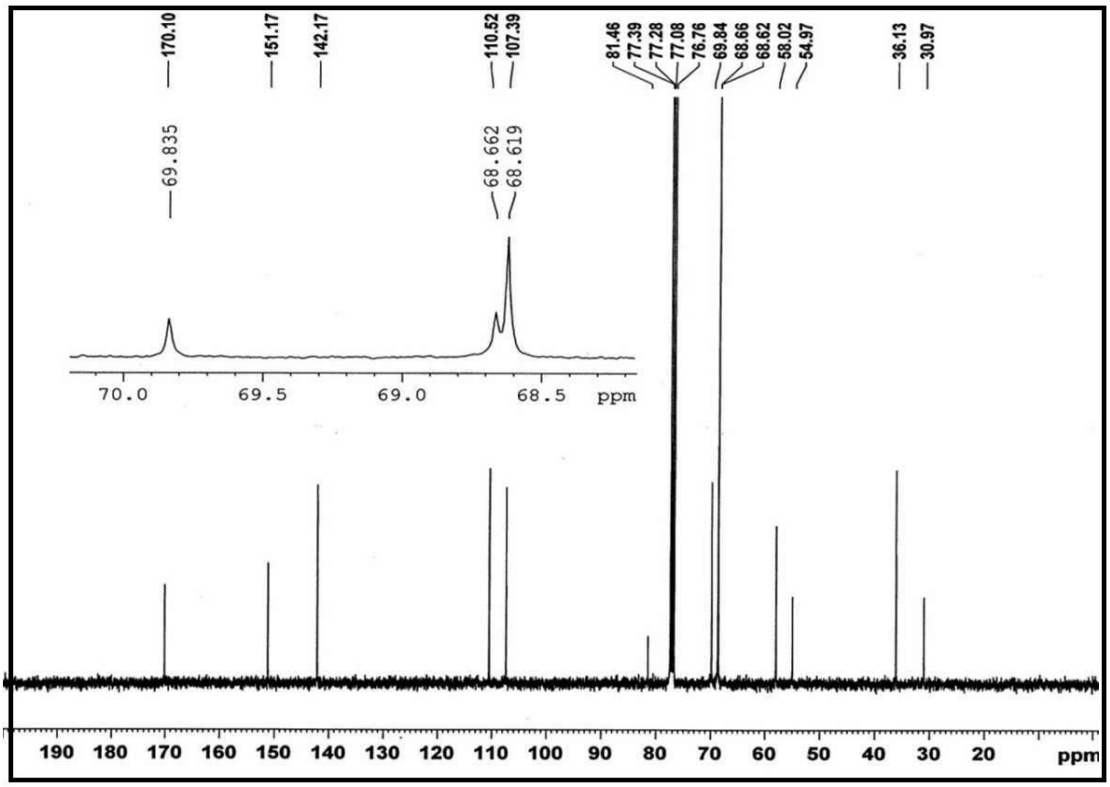

Annexure 12. ^{13}C NMR spectrum of 3b.

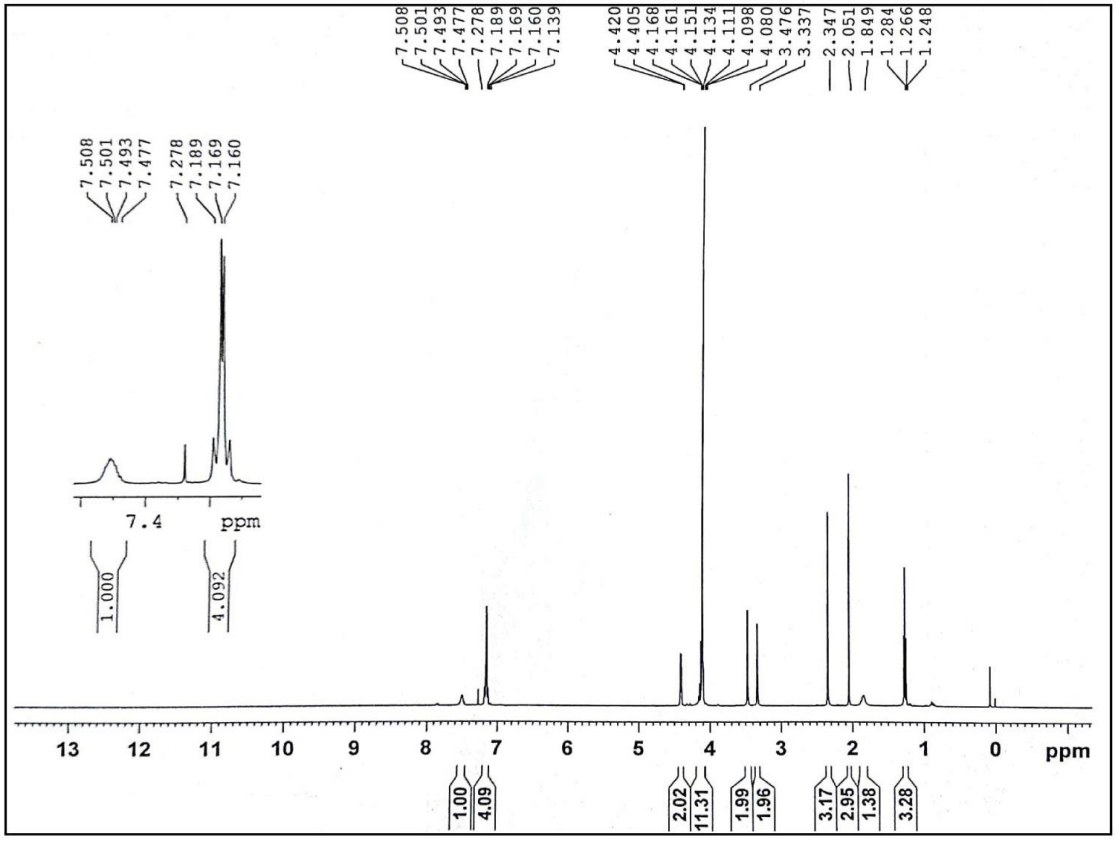

Annexure 13. ^{1}H NMR spectrum of 4a.

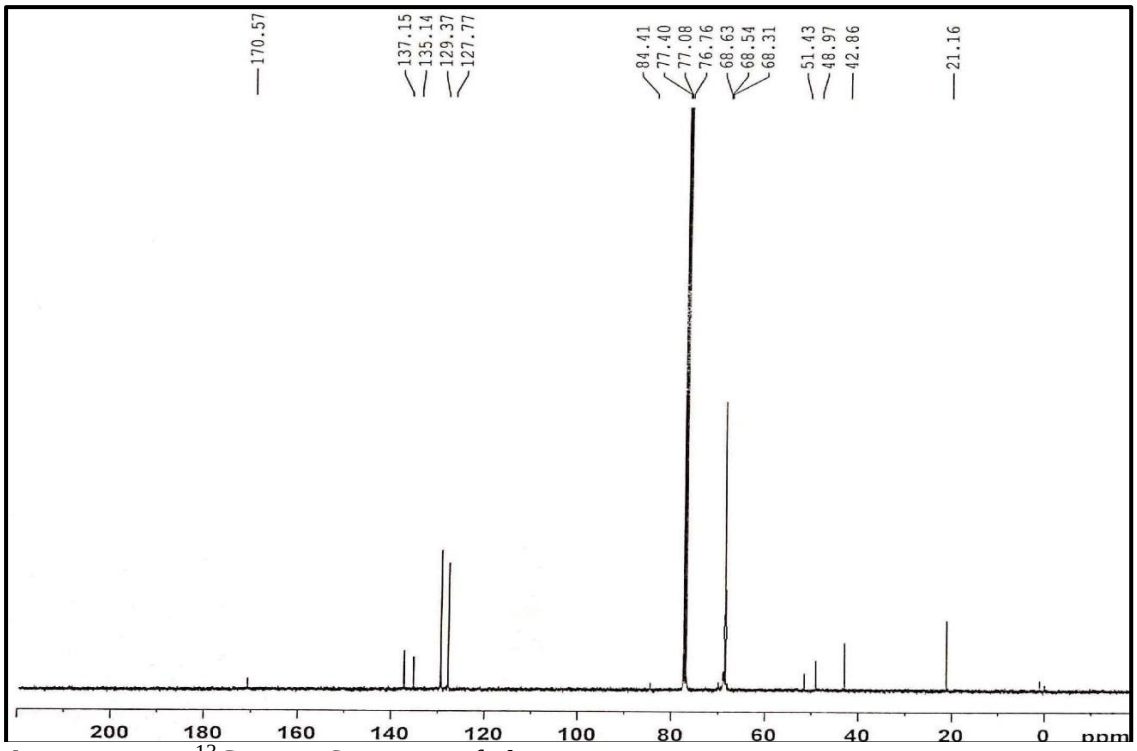

Annexure 14. ^{13}C NMR Spectrum of 4b.

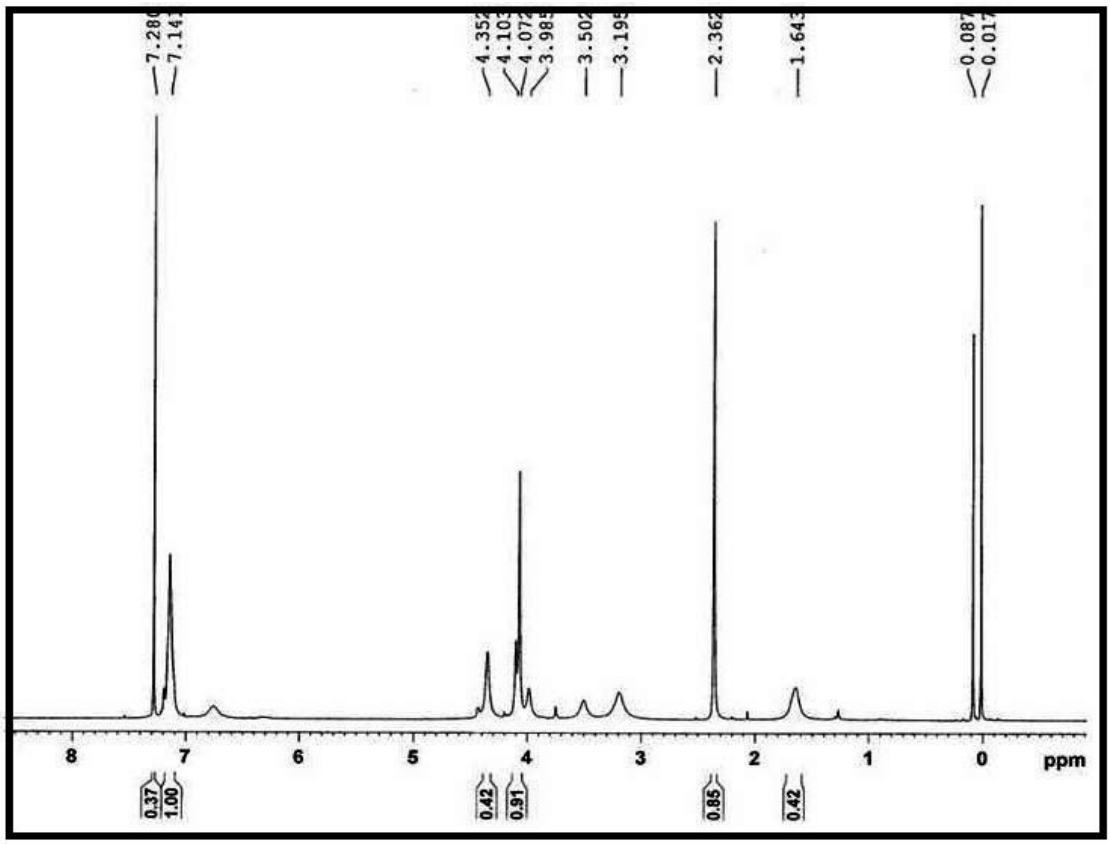

Annexure 15. ^{1}H NMR Spectrum of 4b.

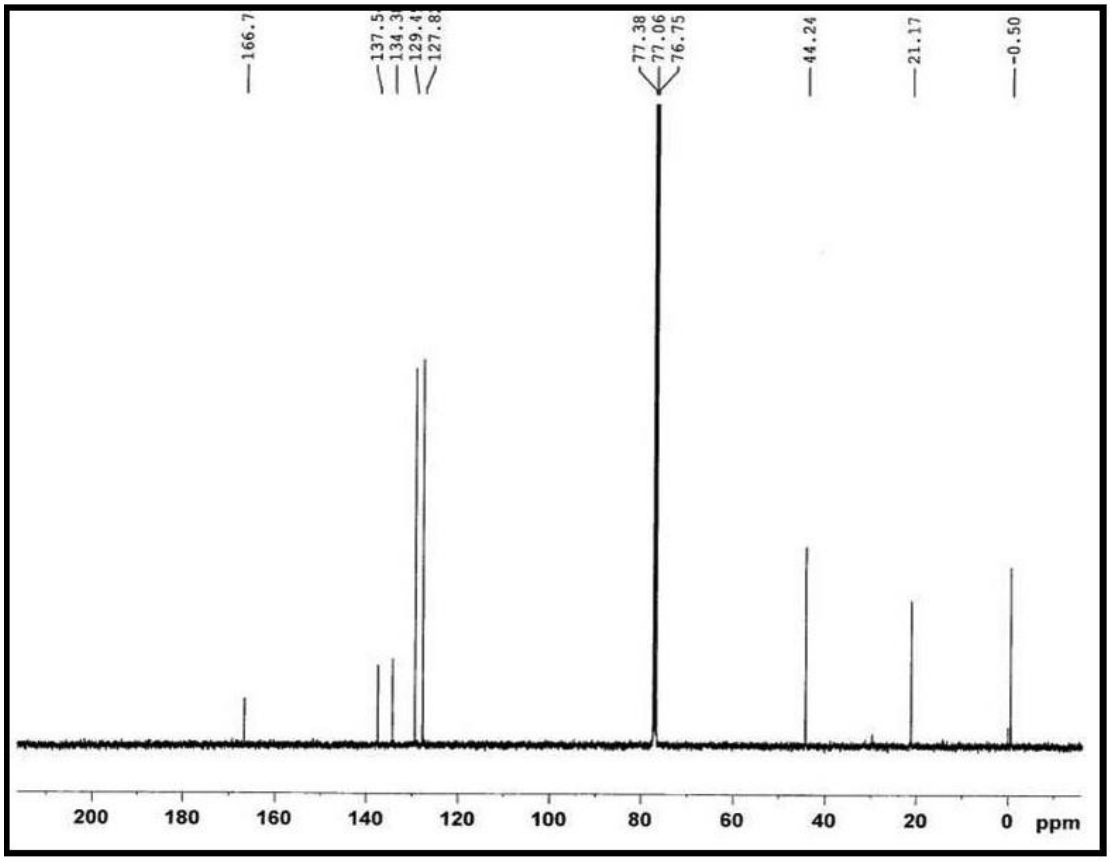

Annexure 16. ^{13}C NMR Spectrum of 4b.

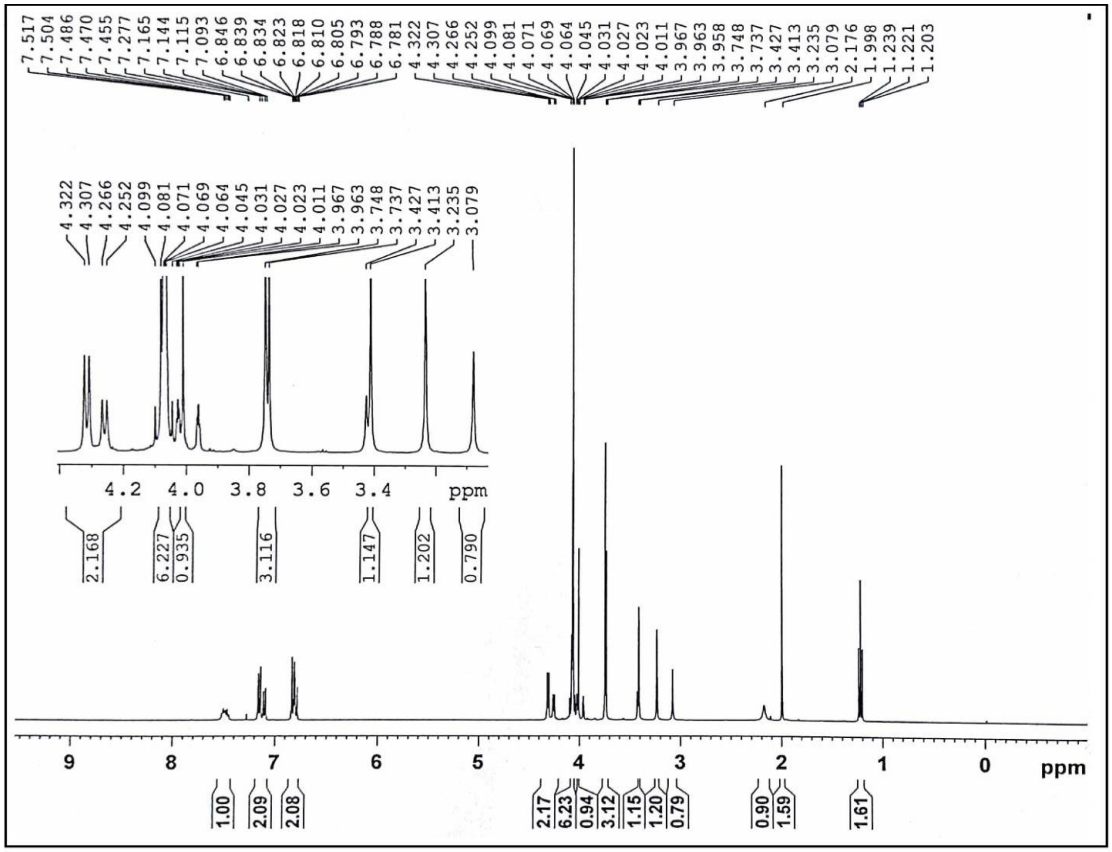

Annexure 17. ^{1}H NMR Spectrum of 5a.

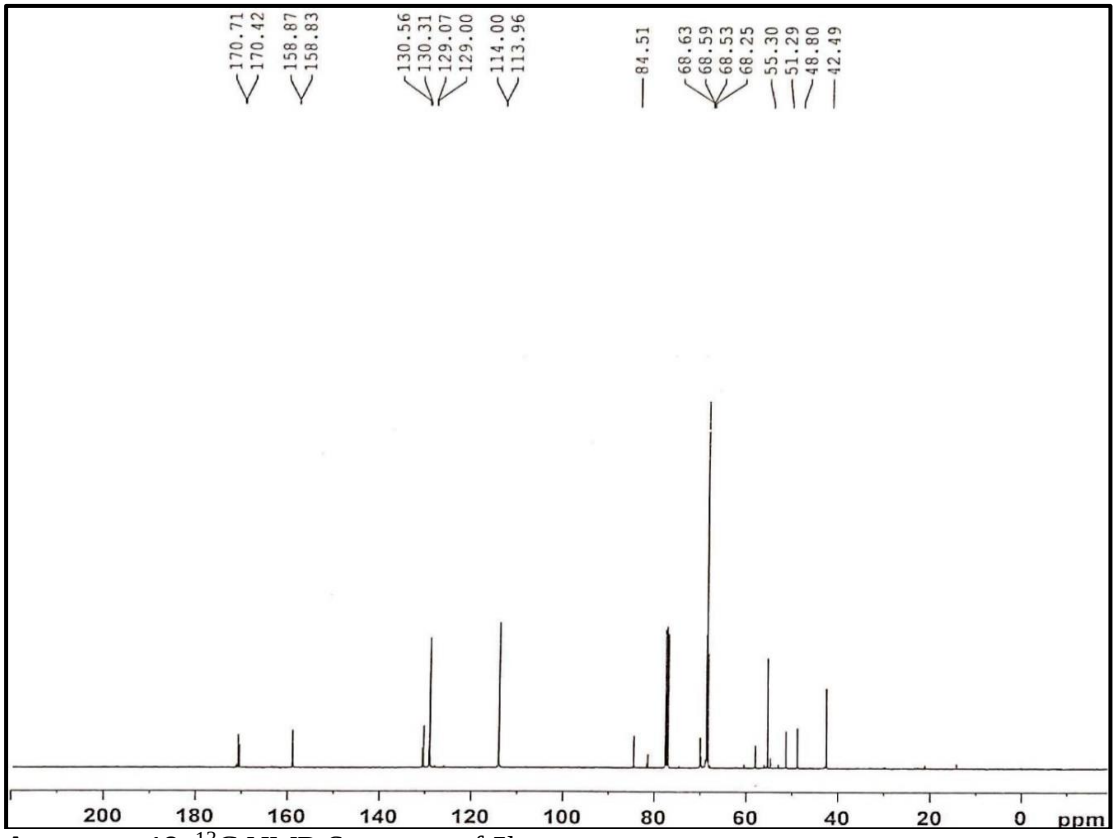

Annexure 18. ^{13}C NMR Spectrum of 5b.

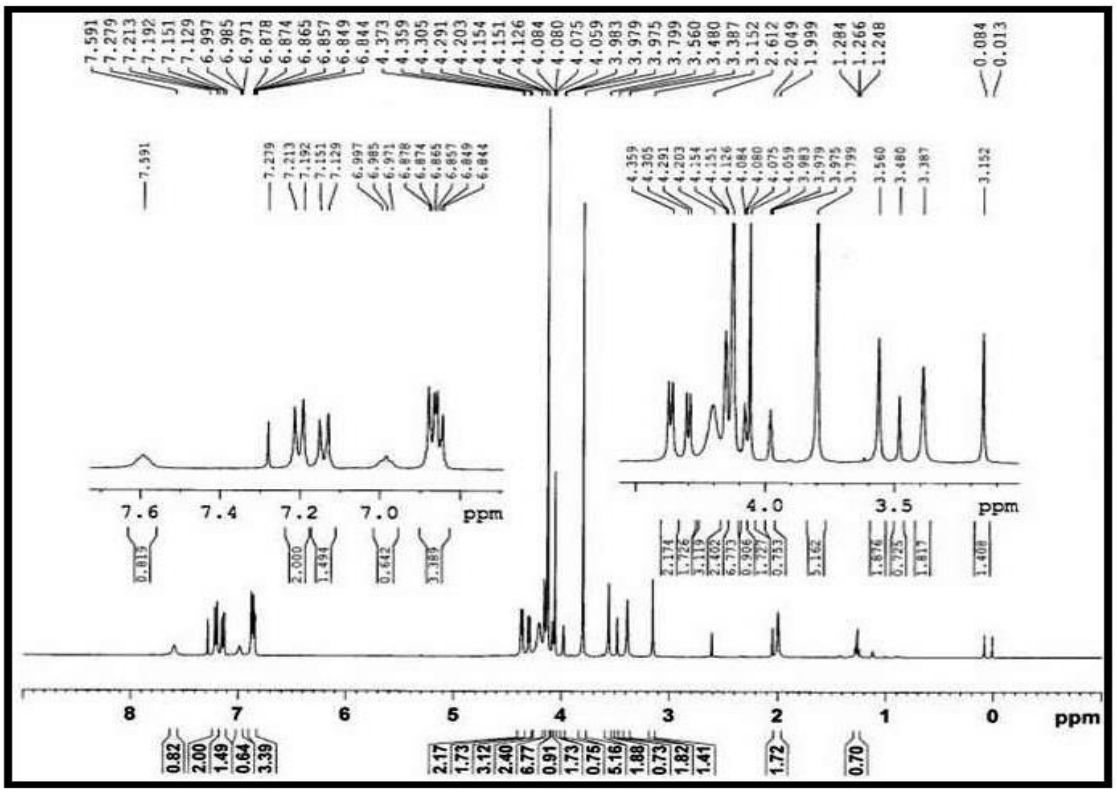

Annexure 19. ^{1}H NMR Spectrum of 5b.

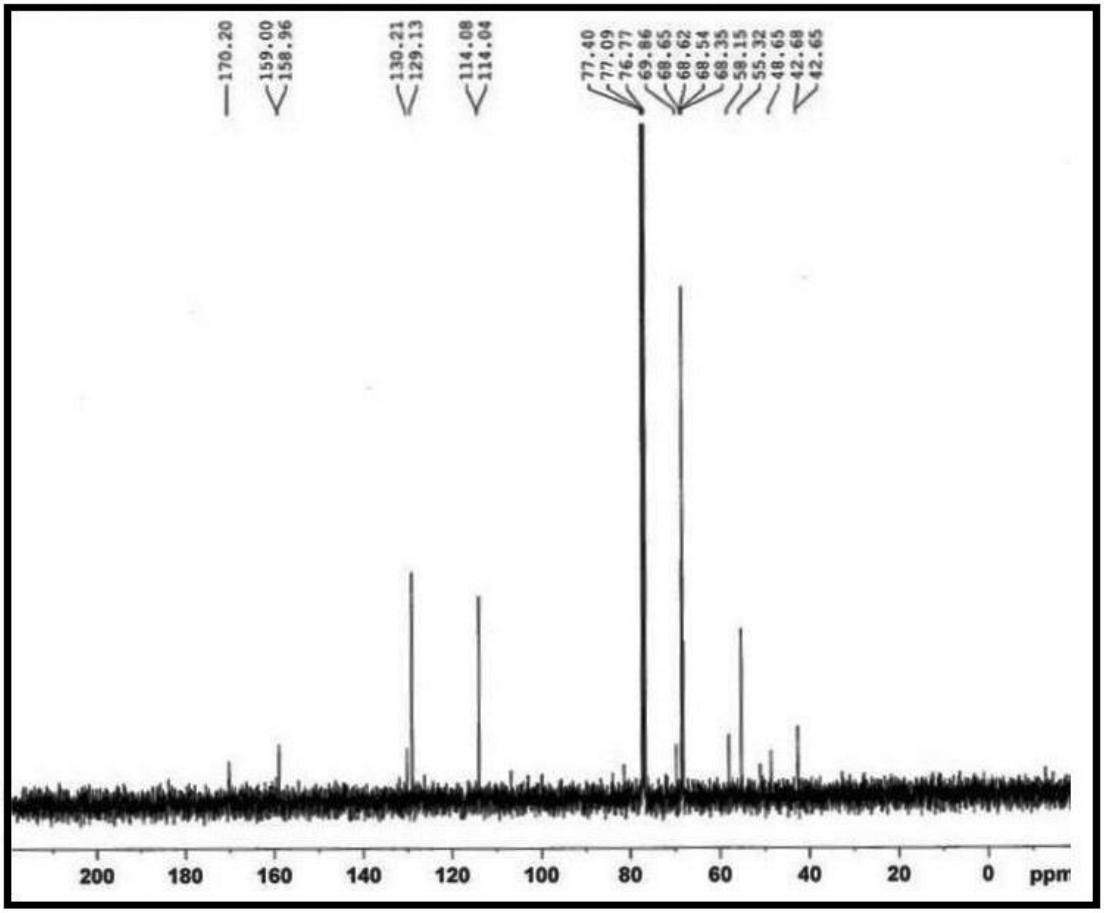

Annexure 20. 13C NMR Spectrum of 5b.

IR Spectra

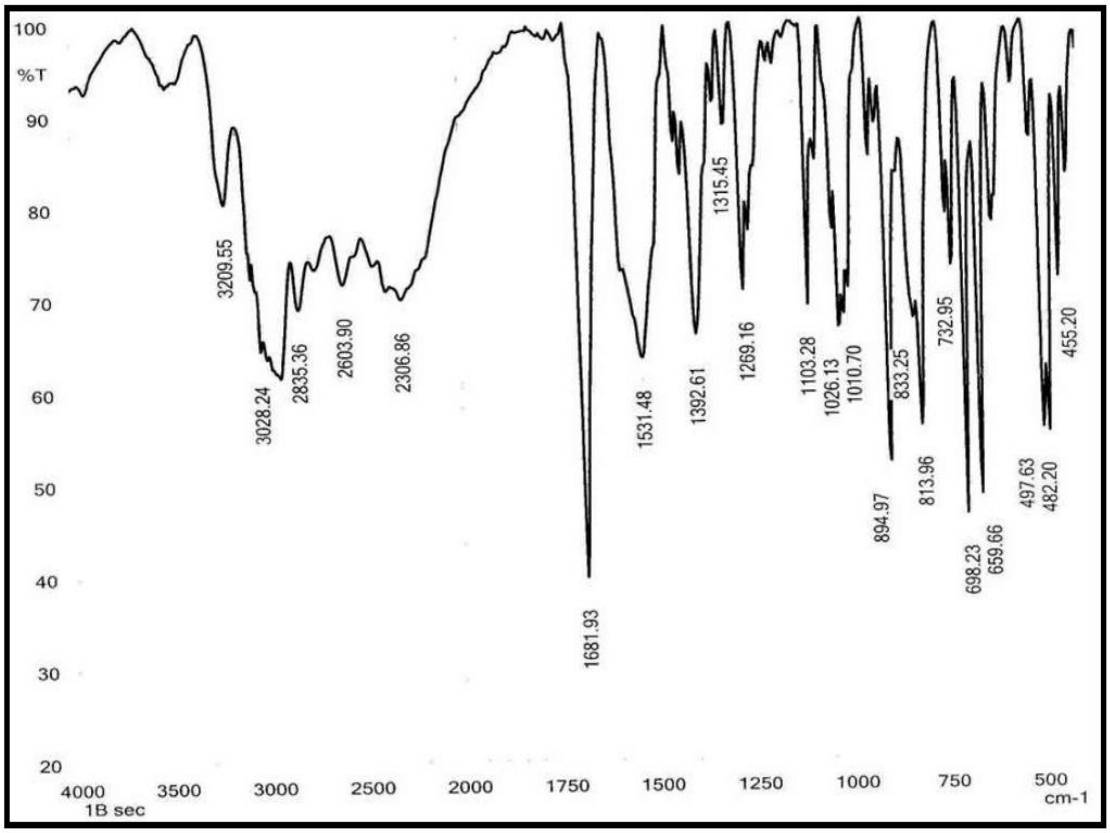

Annexure 21. IR spectrum of 1a.

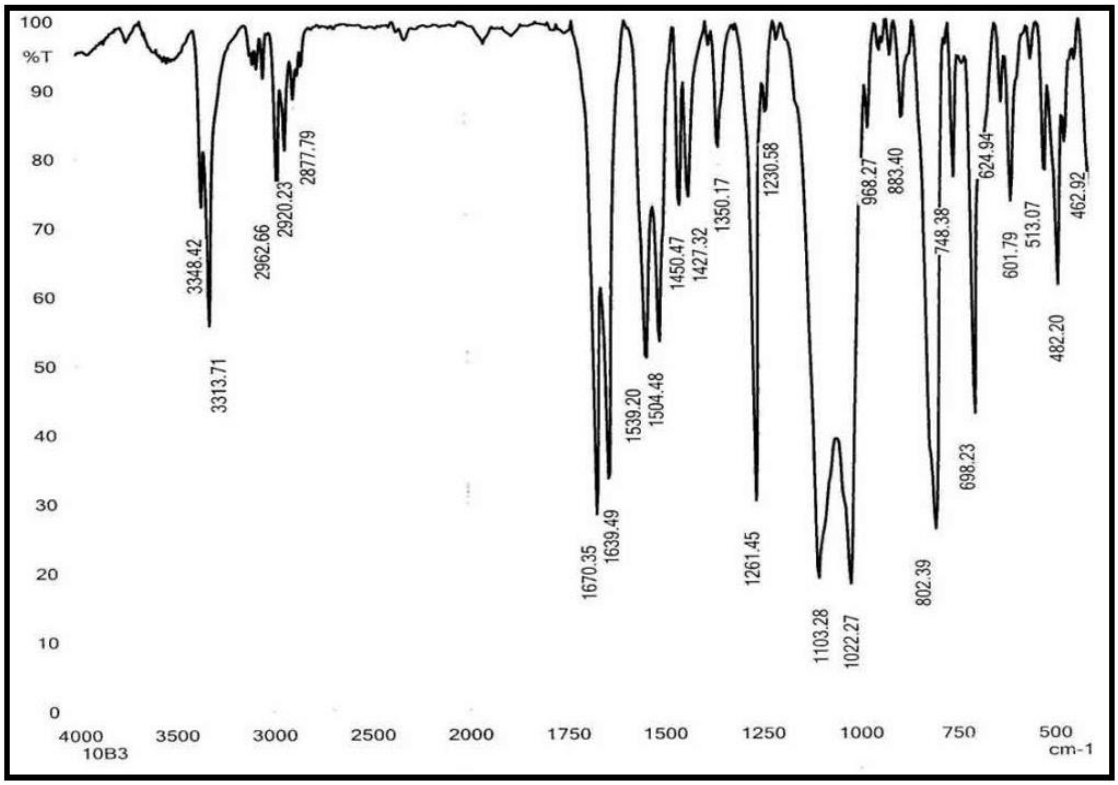

Annexure 22. IR spectrum of 1b.

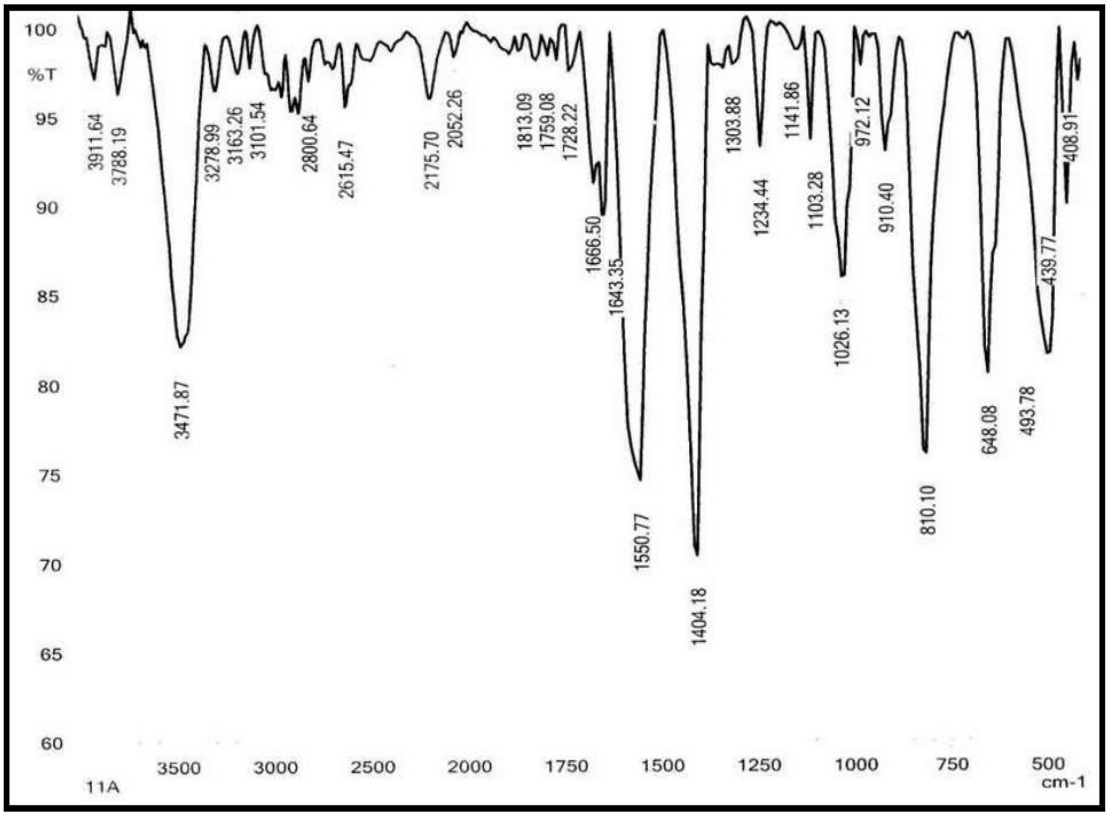

Annexure 23. IR spectrum of 2a.

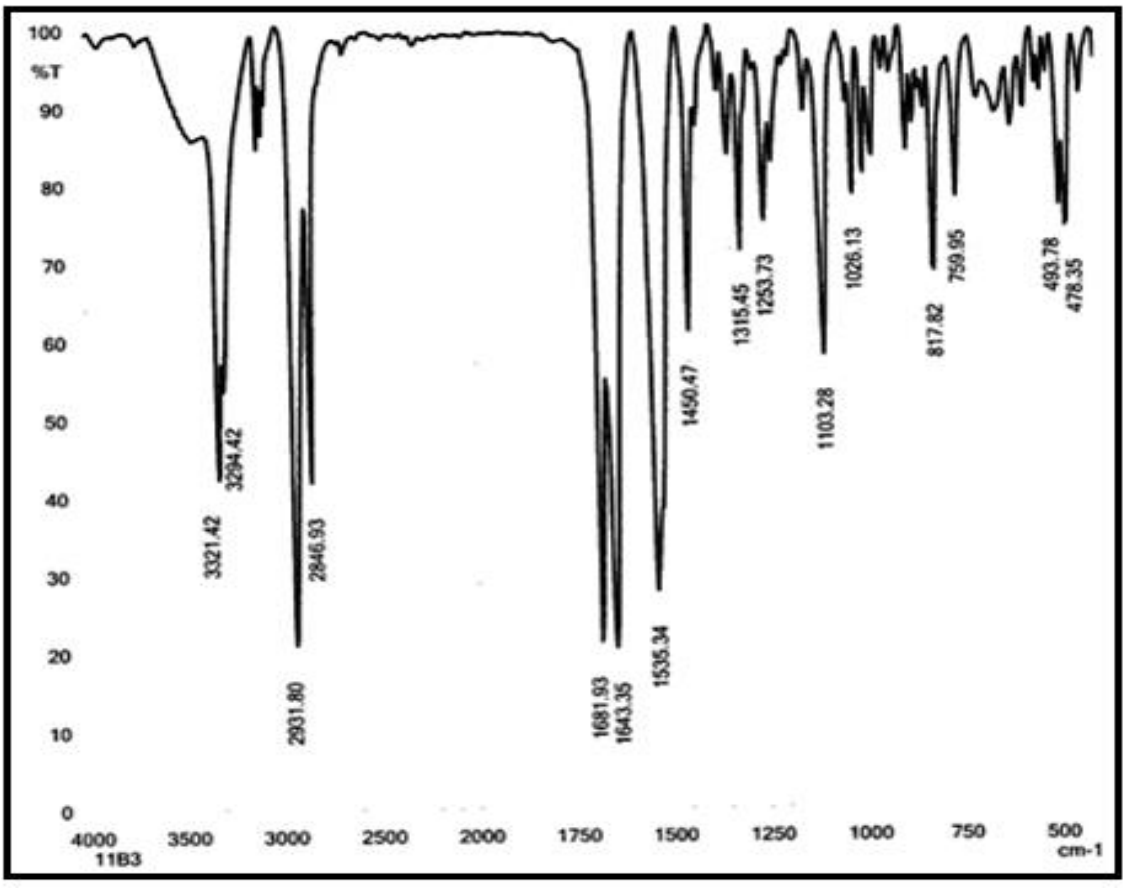

Annexure 24. IR spectrum of 2b.

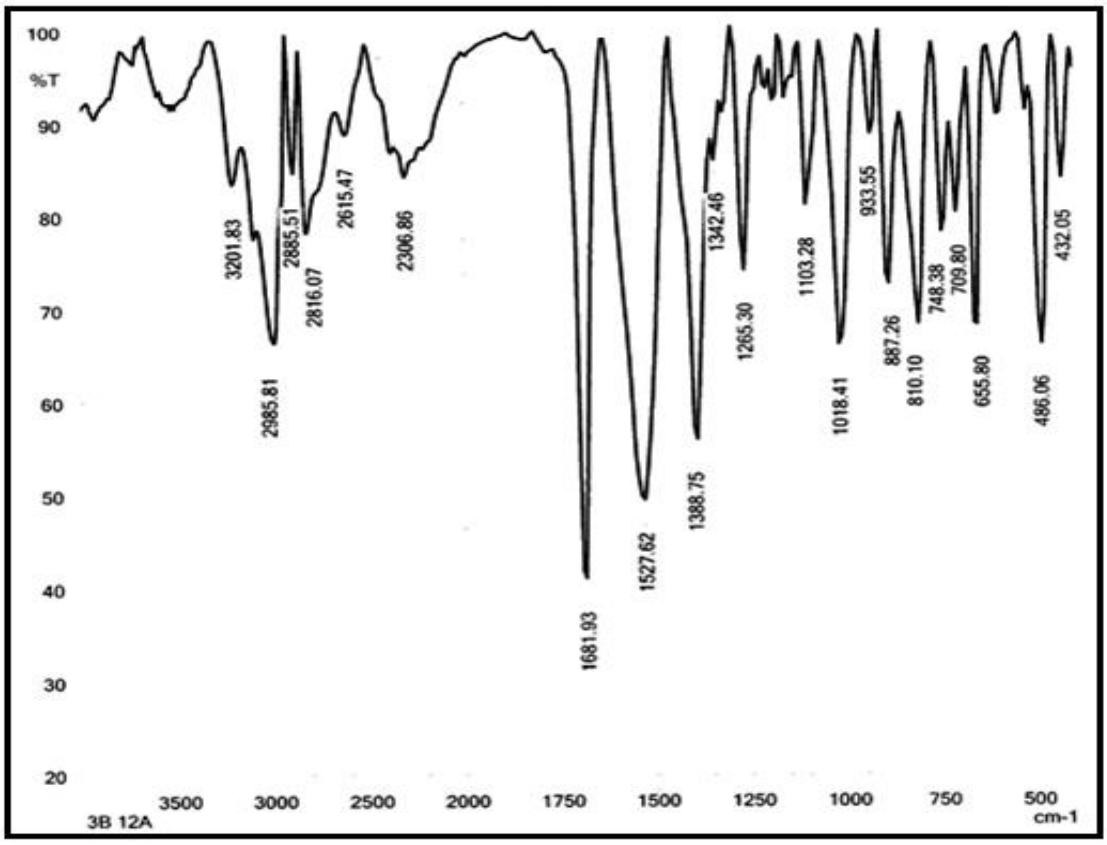

Annexure 25. IR spectrum of 3a.

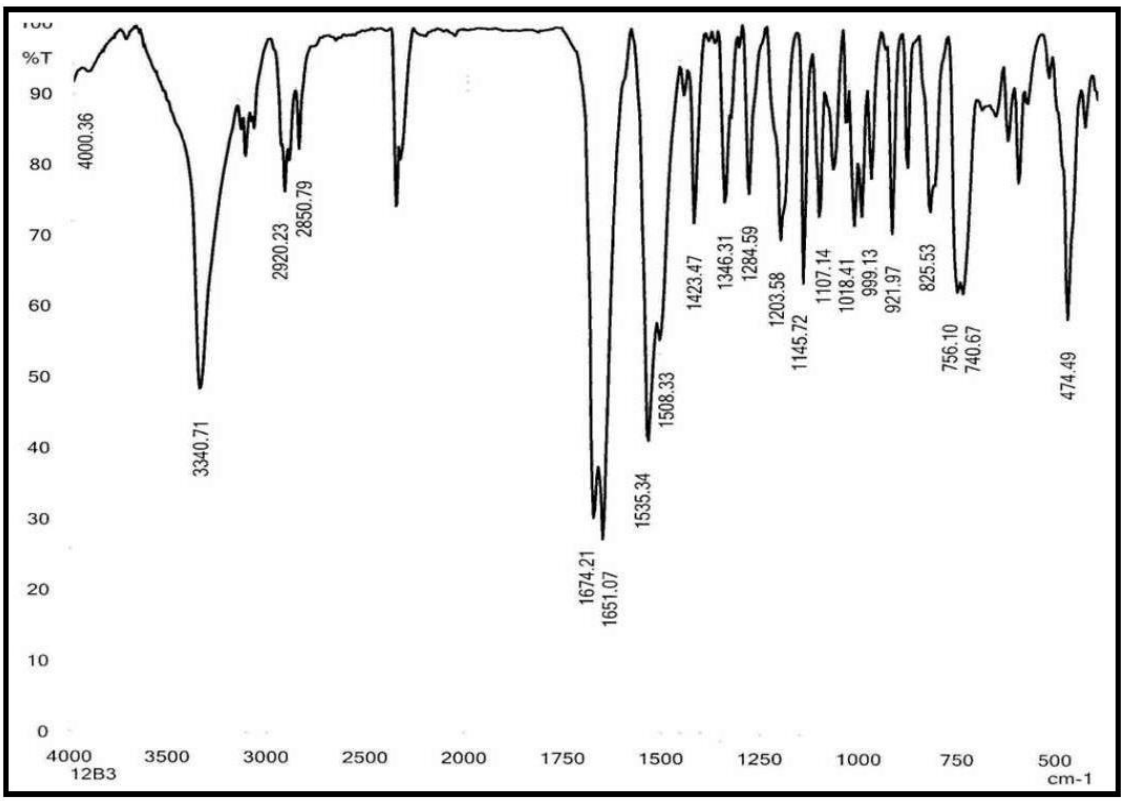

Annexure 26. IR spectrum of 3b.

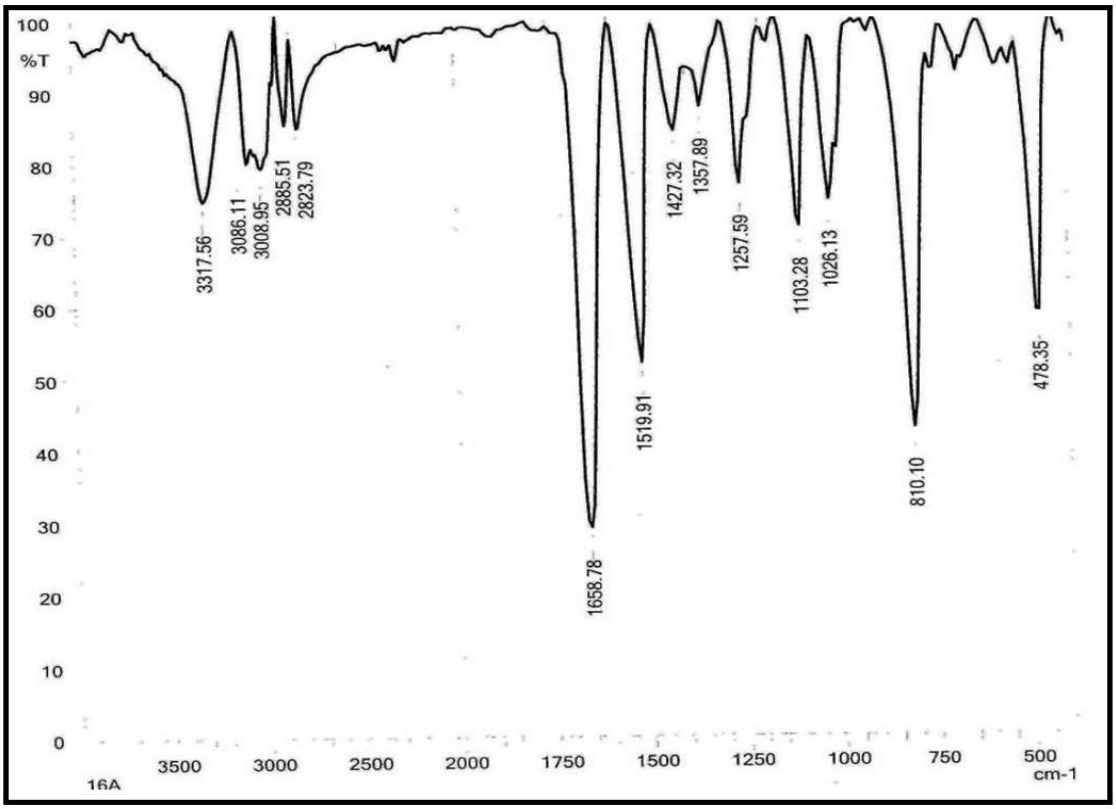

Annexure 27. IR spectrum of 4a.

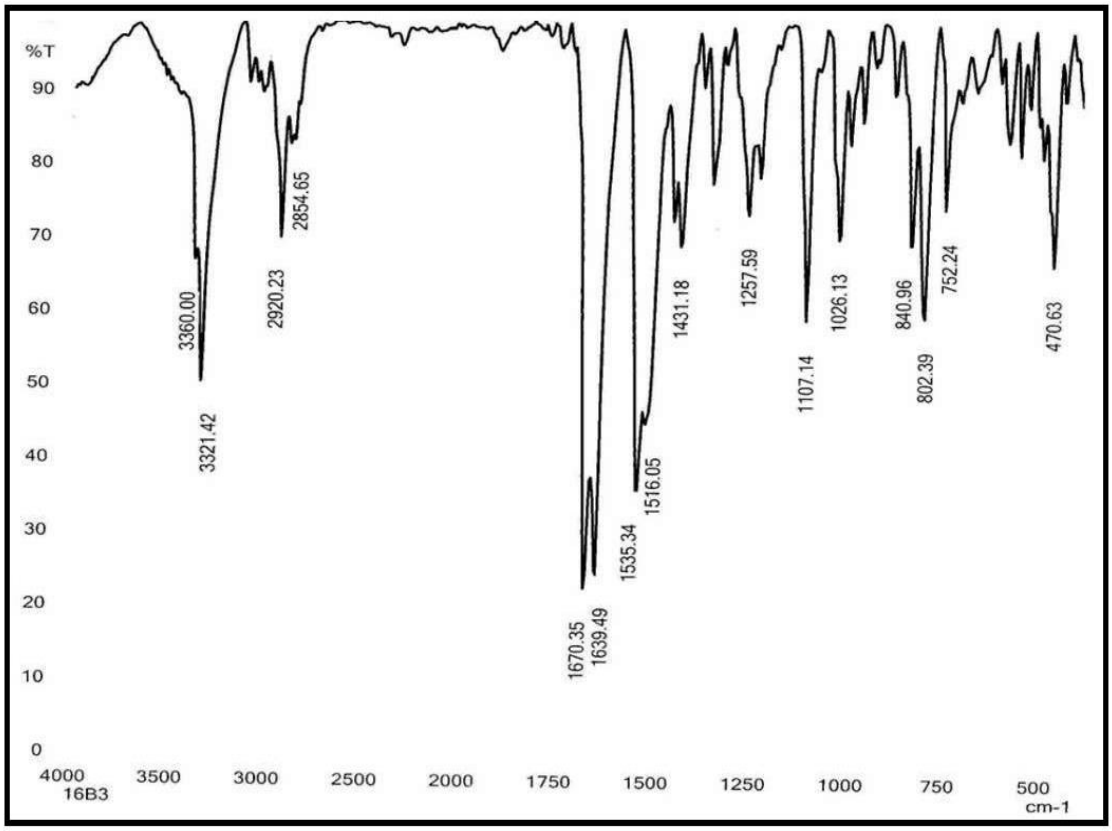

Annexure 28. IR spectrum of 4b.

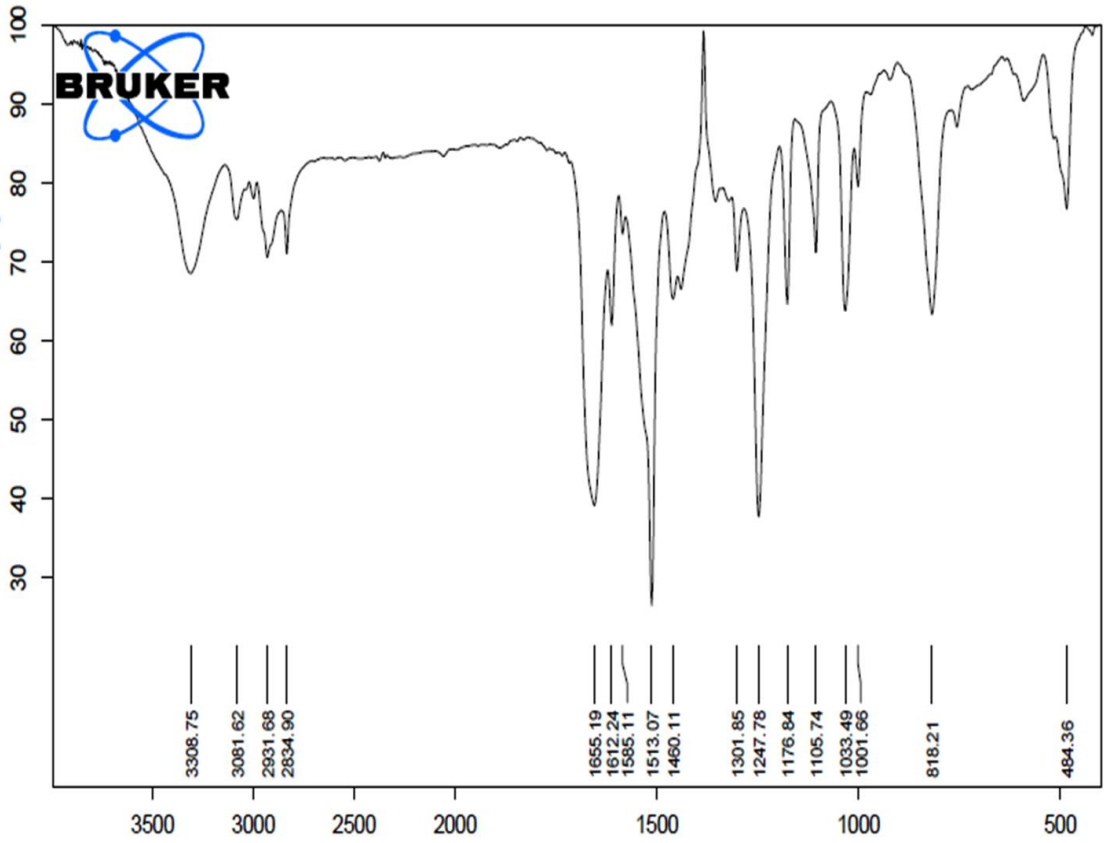

Annexure 29. IR spectrum of 5a.

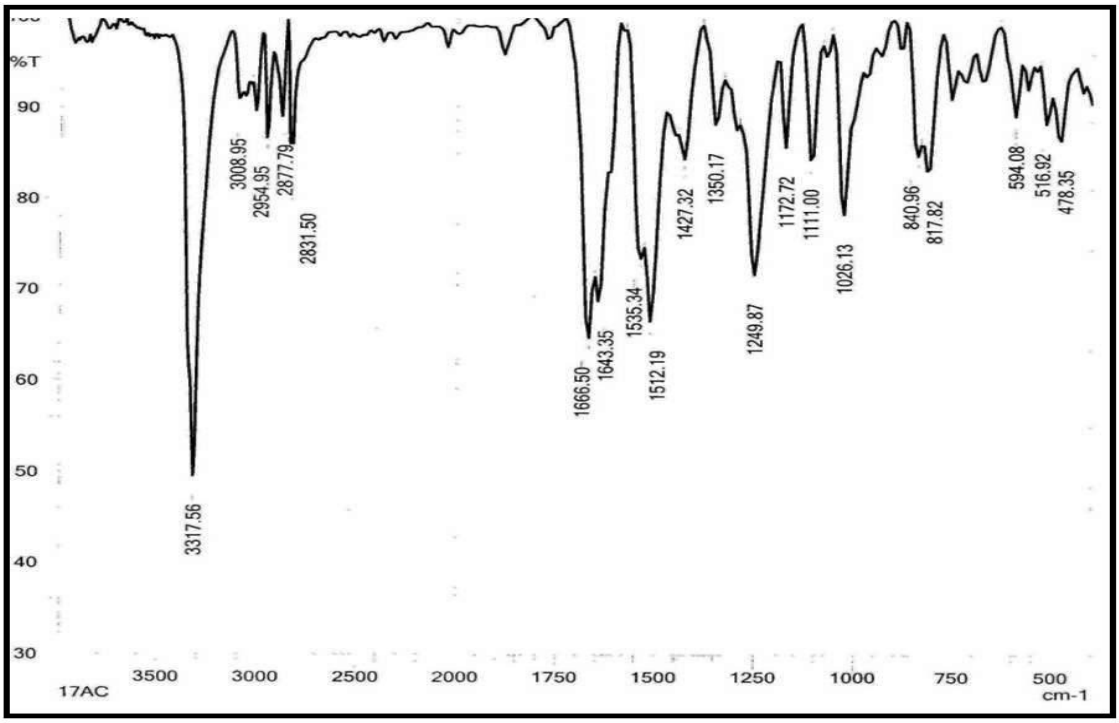

Annexure 30. IR spectrum of 5b.